Lawrence Berkeley National Laboratory
Recent Work

Title
CORRELATION OF H PRODUCTION AND THE WORK FUNCTION OF A SURFACE IN A HYDROGEN PLASMA

Permalink
https://escholarship.org/uc/item/5q43428q

Author
Wada, M.

Publication Date
1983-03-01

eScholarship.org Powered by the California Digital Library
University of California

LBL-15800
c.2

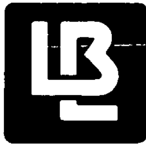

Lawrence Berkeley Laboratory

UNIVERSITY OF CALIFORNIA

RECEIVED
LAWRENCE
BERKELEY LABORATORY
JUN 8 1983
LIBRARY AND
DOCUMENTS SECTION

Accelerator & Fusion Research Division

CORRELATION OF H^- PRODUCTION AND THE WORK FUNCTION OF A SURFACE IN A HYDROGEN PLASMA

Motoi Wada
(Ph.D. Thesis)

March 1983

TWO-WEEK LOAN COPY

This is a Library Circulating Copy which may be borrowed for two weeks. For a personal retention copy, call Tech. Info. Division, Ext. 6782.

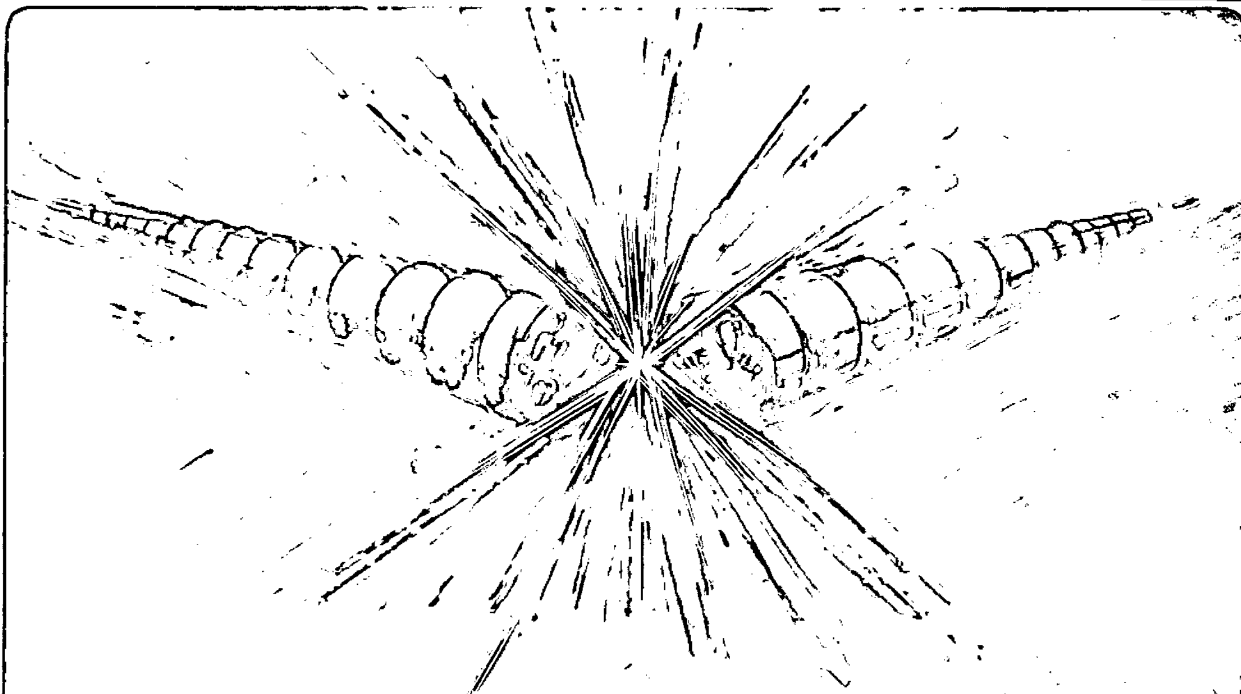

Prepared for the U.S. Department of Energy under Contract DE-AC03-76SF00098

LBL-15800 c.2

DISCLAIMER

This document was prepared as an account of work sponsored by the United States Government. While this document is believed to contain correct information, neither the United States Government nor any agency thereof, nor the Regents of the University of California, nor any of their employees, makes any warranty, express or implied, or assumes any legal responsibility for the accuracy, completeness, or usefulness of any information, apparatus, product, or process disclosed, or represents that its use would not infringe privately owned rights. Reference herein to any specific commercial product, process, or service by its trade name, trademark, manufacturer, or otherwise, does not necessarily constitute or imply its endorsement, recommendation, or favoring by the United States Government or any agency thereof, or the Regents of the University of California. The views and opinions of authors expressed herein do not necessarily state or reflect those of the United States Government or any agency thereof or the Regents of the University of California.

LBL-15800

CORRELATION OF H^- PRODUCTION AND THE WORK FUNCTION OF A SURFACE IN A HYDROGEN PLASMA

Motoi Wada

Ph.D. Thesis

Lawrence Berkeley Laboratory
University of California
Berkeley, CA 94720

March, 1983

---

* This work was supported by the Director, Office of Energy Research, Office of Fusion Energy, Development and Technology Division, of the U. S. Department of Energy under Contract No. DE-AC03-76SF00098.

CORRELATION OF H^- PRODUCTION AND THE WORK FUNCTION OF A SURFACE IN A HYDROGEN PLASMA

Motoi Wada

Ph.D. Thesis

Lawrence Berkeley Laboratory
University of California
Berkeley, CA 94721

March, 1983

ABSTRACT

Surface-plasma negative hydrogen ion sources are being developed as possible parts for future neutral beam systems. In these ion sources, negative hydrogen ions (H^-) are produced at low work function metal surfaces immersed in hydrogen plasmas. To investigate the correlation between the work function and the H^- production at the surface with a condition similar to the one in the actual plasma ion source, these two parameters were simultaneously measured in the hydrogen plasma environment.

The photoelectron emission currents from Mo and Cu surfaces in a cesiated hydrogen discharge were measured in the photon energy range from 1.45 to 4.14 eV, to determine the work function based on Fowler's theory. A small magnetic line cusp plasma container was specially designed to minimize the plasma noise and to realize the efficient collection of incident light onto the target. The photoelectron current was detected phase sensitively and could be measured with reasonable accuracy up to about 5 x 11^{11} cm^{-3} of the plasma electron density.

As Cs density was increased in the hydrogen discharge, the work function decreased until it reached a minimum value. This value of the lowest work function was approximately 1.4 eV for both Mo and Cu surfaces, and the detected total H^- current was a maximum at this condition. Further introduction of Cs into the discharge from this point increased the work function and decreased the total H^-. Thus, at any coverage of Cs on the surface, the total H^- current was monotonically increasing for decreasing work function.

When the negative bias potential to the H^- production surface was increased, the work function changed in a way corresponding to a decrease in Cs coverage. Due to this effect a bias potential for maximum H^- production was observed for steady state operation of the ion source with a fixed density of Cs. When H^- currents from surfaces of similar work functions, but with different bias potentials, were compared, the total H^- current was always larger at the higher bias potential.

Table of Contents

		PAGE
I.	Introduction	1
II.	Physics of a surface plasma H^- ion source	5
	(2-1) Formation of atomic hydrogen at the surface	5
	(2-2) Formation of H^- at the surface	10
	(2-3) Transport of H^- beam in the plasma	16
III.	Experimental approach and apparatus	19
	(3-1) Experimental approach	19
	(3-2) Apparatus	24
	1. Ion source	24
	2. Light source system	31
	3. Momentum analyzer	32
IV.	Experimental procedure and data analysis	37
	(4-1) Experimental procedure	37
	1. Cleaning of the ion source	37
	2. Cs loading of the ion source	39
	3. Start up of the ion source	40
	4. Light source operation	41
	5. Experimental measurements	42
	(4-2) Data analysis	44
V.	Experimental results and discussion	48
	(5-1) Correlation between work function and H^- production	48
	(5-2) Effect of target bias on the H^- production	52
	(5-3) H^- energy spectra at different work functions	57
	(5-4) H^- produced at thick Cs covered surface	59
	(5-5) Upper limit of H^- production probability	65

PAGE

VI. Conclusions 69

Acknowledgements vi

References 71

Figure Captions vii

Appendix 1. Fowler's theory of photoelectron emission. 75

Appendix 2. Measurements of photoelectron emission from alkali-covered metal surfaces in an ultra high vacuum 81

Appendix 3. Langmuir probes 88

Appendix 4. The momentum analyzer 97

Appendix 5. Pyroelectric radiometer 103

Appendix 6. Calibration of the momentum analyzer 108

Appendix 7. Change of the work function by a hydrogen discharge. 116

Appendix 8. The plasma sheath equation for a H^- production surfaces. 121

Appendix 9. Work function measurements in the plasma after glow. 127

ACKNOWLEDGMENTS

I am indebted to Dr. R. V. Pyle for suggesting and supervising this project. I am also indebted to Dr. K. H. Berkner, Dr. J. R. Hiskes, and Dr. W. B. Kunkel for their keen interest and guidance to the project, J. W. Stearns for assistance in all aspects of the experiment, and Dr. W. F. Steele for help with the computer system. I want to thank the other graduate students who spent many hours trying to help me understand experimental results. These include Dr. N. E. Abt, Gary Guethlein, Dr. K. R. Stalder, and John Trow. My thanks also go to the members of the mechanical shops of H. A. Hughes and L. A. Biagi who built the mechanical components of the experiment.

Finally, I would like to thank the secretarial staff led by A. Aitkens for typing this manuscript.

LIST OF FIGURE CAPTIONS

FIGURE	PAGE
1. Conceptual diagram of surface plasma H^- source	6
2. Illustration of the lowering and broadening of the H^- bound level in the vicinity of a surface.	12
3. Illustration of the interaction potential used by Hiskes and Karo to calculate the survival probability for H^- leaving a surface, (a) with thick coverage of alkali metal, and (b) with partial monolayer of Cs on W.	14
4. Comparison of the result of calculations by Kishinevskiy and Hiskes and Karo for H^- survival probability as a function of exit energy.	15
5. Cross sections relevant to H^- destruction in the plasma.	17
6. Block diagram of the major parts of the apparatus.	23
7. Cross sectional view of the target	25
8. Cs oven.	27
9. Perspective illustration of the ion source	28
10. Radial profile of ion saturation current measured by Langmuir probes.	29

FIGURE PAGE

11. Axial profile of ion saturation current measured by Langmuir probes. 30

12. Block diagram of experimental set up to measure the spectral intensity of incident monochromatic beam. 34

13. Mass analyzer and magnetic shielding. 36

14. Typical output of the least square fit program to determine the work function. 45

15. Output of the mass analyzer data. 47

16. The dependence of (H^- current)/(target current) upon the work function for the Cu target biased at -100 V. 49

17. The dependence of (H^- current)/(target current) upon the work function for the Mo target biased at -100, -200 and -300 V. 51

18. Dependence of detected H^- current on target bias for a steady state source operation. 54

19. Dependence of target work function on target bias at the steady state operation of the ion source. 55

20. The three groups of H^- produced by back scattering process. 58

FIGURE PAGE

21. Comparison of energy spectra for H^- produced at the target with work function of, 60
(a) 3.4 eV
(b) 2.85 eV
(c) 2.19 eV
(d) 1.40 eV

22. Comparison of energy spectra for H^- produced at the target with similar work function (~ 1.69 eV) but different bias potential. (a) 100 V, (b) 200 V and (c) 300 V. 61

23. Behavior of H^- current and target work function as more Cs was introduced from the source condition near the maximum H^- production. 62

24. H^- energy spectra for different target work functions for Cs coverage thicker than the work function minimum. The work function of the target was, 63
(a) 1.44 eV
(b) 1.68 eV
(c) 1.90 eV
(d) 1.95 eV

FIGURE PAGE

25. Comparison of the target current and ion saturation current at different work function. Target bias was held at 200 V, and discharge power was 5 W. 66

26. Time history of photoelectron current and H^- current after the target bias was adjusted down to 100 V from 400 V. 68

27. Effect of temperature and finite band width on the theoretical curve of photoelectron emission efficiency. 79

28. Illustration of the deviation of the experimental points to theoretical curve of (quantum efficiency)$^{1/2}$ versus photon energy. 80

29. Experimental setup for the photoelectric work function measurement in the U.H.V. system. 82

30. Experimental comparison of quantum efficiency at different band width of incident light beam. 83

31. Comparison between work functions measured by work function diode and photoelectric emission. 85

32. Typical trace of the I-V characteristics of a work function diode. 87

33. Block diagram of electrical circuit of Langmuir probes. 89

34. A typical probe voltage-current characteristics. 91

FIGURE PAGE

35. Plot of probe current to the probe bias voltage after subtracting the high energy tail of electron distribution. 92

36. Fit of probe current to orbital motion in the electron saturation region. 96

37. Two regions to consider space charge effect. 102

38. Schematic view of the pyroelectric radiometer. 104

39. Spectral dependence of the responsitivity of the pyroelectric detector. 105

40. Spatial dependence of the responsitivity of the pyroelectric detector. 106

41. Energy spectrum of H^- beam produced by a Cs discharge. 110

42. Potential diagram along the path of H^- beam. 111

43. Electrical circuit to measure contact potential difference between the target and the collector. 112

44. Result of the contact potential difference measurement. The indicated number on the trace is the potential difference between the target and the collector. Shape of the H^- momentum spectrum is identical when bias potential of the collector is more than -3 V above the target bias potential. 115

FIGURE PAGE

45. Behavior of photoelectron current after turning on the K getter dispenser. 117

46. Change of the work function of K covered Cu surface by a hydrogen discharge. 119

47. Upper limit of H^- production efficiency due to space charge effect. $T_e = 1$ eV. 126

48. Sequence to measure photoelectron current by turning off the arc power by using a pulsive light source. 128

49. Diagram of the electrical circuit used to measure the work function during the after glow. Abbreviations are as follows: D = delay gate, A = and gate, C = comparator. 129

CHAPTER 1

INTRODUCTION

Because of its higher neutralization efficiency compared to that of positive hydrogen ions,[1] the negative hydrogen ion is proposed for future neutral beam injection systems. To produce H^- ion beams with a reasonable efficiency and quality, surface-plasma, or self extraction H^- ion sources are currently being developed.[2] This type of ion source has either a discharge cathode, or a separately installed metal plate which is biased negative with respect to the plasma potential, and is facing the exit of the source. Sometimes this surface is given a curvature so that the geometrical focal point is at the source exit.[3] A flux of hydrogen particles is created by the hydrogen discharge in front of the metal surface. Some part of this hydrogen flux is converted to H^- at the surface and extracted toward the source exit across the sheath between the plasma and the metal surface.

This surface production of H^- was reported to be enhanced by introducing Cs into the ion source.[4] Cs adsorption on a metal surface is known to reduce the work function and electron emission from a surface is also known to be higher for lower work function surfaces. Therefore, the observed increase of H^- production was attributed to the higher electron transfer from the metal surface to the atomic hydrogen, due to a reduction of the work function. The quantitative dependence of H^- production on the work function has been calculated by Janev,[5] Kishinevskiy,[6] Hiskes and Karo,[7]

and Rasser et al.[8] Their results show that the efficiency of the H^- production at the surface is high when the work function of the metal surface is low. This effect is especially pronounced for H atoms leaving the surface with lower velocities.

To confirm this relation between the work function and the H^- production efficiency, work functions were monitored in several experiments that measured the H^- production from the surface. Schneider[9] has measured the H^- and D^- produced by back scattering of hydrogen and deuterium ions from a substrate with varying coverage of alkai-metal. A similar experiment was conducted by Yu[10] for H^- production by a Ne^+ beam incident on a Cs and H_2 coadsorbed surface. Optimum H^- yields in these experiments were found near the corresponding minima of the work functions. Thus, the relation between the work function of the surface and the H^- production efficiency has been experimentally verified.

Unlike experiments of basic processes such as back scattering and sputtering, H^- production at the surface in an actual surface plasma ion source is not well understood, because of the complex characteristics of the plasmas. Since so many kinds of particles strike it, (e.g., hydrogen ions, atomic hydrogen, Cs ions) it is difficult to predict the condition of the H^- production surface. For example, energetic particles may decrease the Cs coverage by the sputtering processes below the work function minimun. Besides, hydrogen and impurities in the discharge will be adsorbed with Cs on the metal surface, and the value of the work function minimum of

this kind of surface is not necessarily the same as that without a discharge.

Until now, the target surface has been assumed to be at the work function minimum when the maximum H^- ion current is observed.[11] Also, the value of the work function minimum was considered to be that of a pure Cs-substrate system. Due to experimental difficulties, surface conditions had never yet been monitored in the presence of a discharge. Thus, to understand the basic physics of the actual surface-plasma H^- ion source, the following points are needed to be investigated:

(1) What is the lowest value of work function for a metal surface immersed in the cesiated hydrogen discharge

(2) Does the work function minimum give the maximum H^- yield

In this experiment the work function of the H^- production surface was measured by monitoring the photoelectron emission current. Measured values of the work function were compared with the total current and energy spectrum of H^- from the surface, and following results were observed:

(a) H^- surface production is monotonically increasing for a decreasing work function.

(b) The work function of a metal in cesiated hydrogen discharge can be lower than 1.5 eV.

(c) Enhancement of H^- surface production by the reduction of work function is especially pronounced at low energies of H^- ions.

(d) H^- surface production in the surface plasma source is monotonically increasing for increasing bias voltage to the metal plate.

These findings together with other experimental results are described and discussed in Chapter 5, following explanations of the experimental system in Chapter 3 and the experimental procedure in Chapter 4. Basic physics related to the experimental device is briefly introduced in Chapted 2, and conclusions are summarized in Chapter 6.

CHAPTER 2

PHYSICS OF A SURFACE PLASMA H^- ION SOURCE

Contrary to its relatively complicated physics, the basic structure of a surface plasma H^- ion source is simple. The main parts of the source are schematically drawn in Fig. 1. The negatively biased metal plate, often called the converter, is immersed in the cesiated hydrogen plasma facing the exit of the ion source. In several source geometries, this metal plate also serves as the discharge cathode. Formation of a negative hydrogen ion beam is a three stage process; first, particle radiation from the plasma creates a flux of atomic hydrogen leaving the surface; second, part of this atomic hydrogen flux is converted to H^- flux by electron transfer from the metal substrate, it is this process where the work function of the surface plays an important role; and third, H^- ion current is accelerated back to the plasma across the sheath, and transported to the source exit. In this chapter, this three stage process will be explained.

(2-1) Formation of Atomic Hydrogen leaving the Surface

The metal surface immersed in the plasma is irradiated by the plasma particles. In a steady state, the incoming hydrogen flux is equal to the hydrogen flux leaving the surface. Some part of this flux leaving the surface is atomic hydrogen which can be converted to H^-. Two processes are most probably responsible for the production of the atomic hydrogen flux from the surface; back

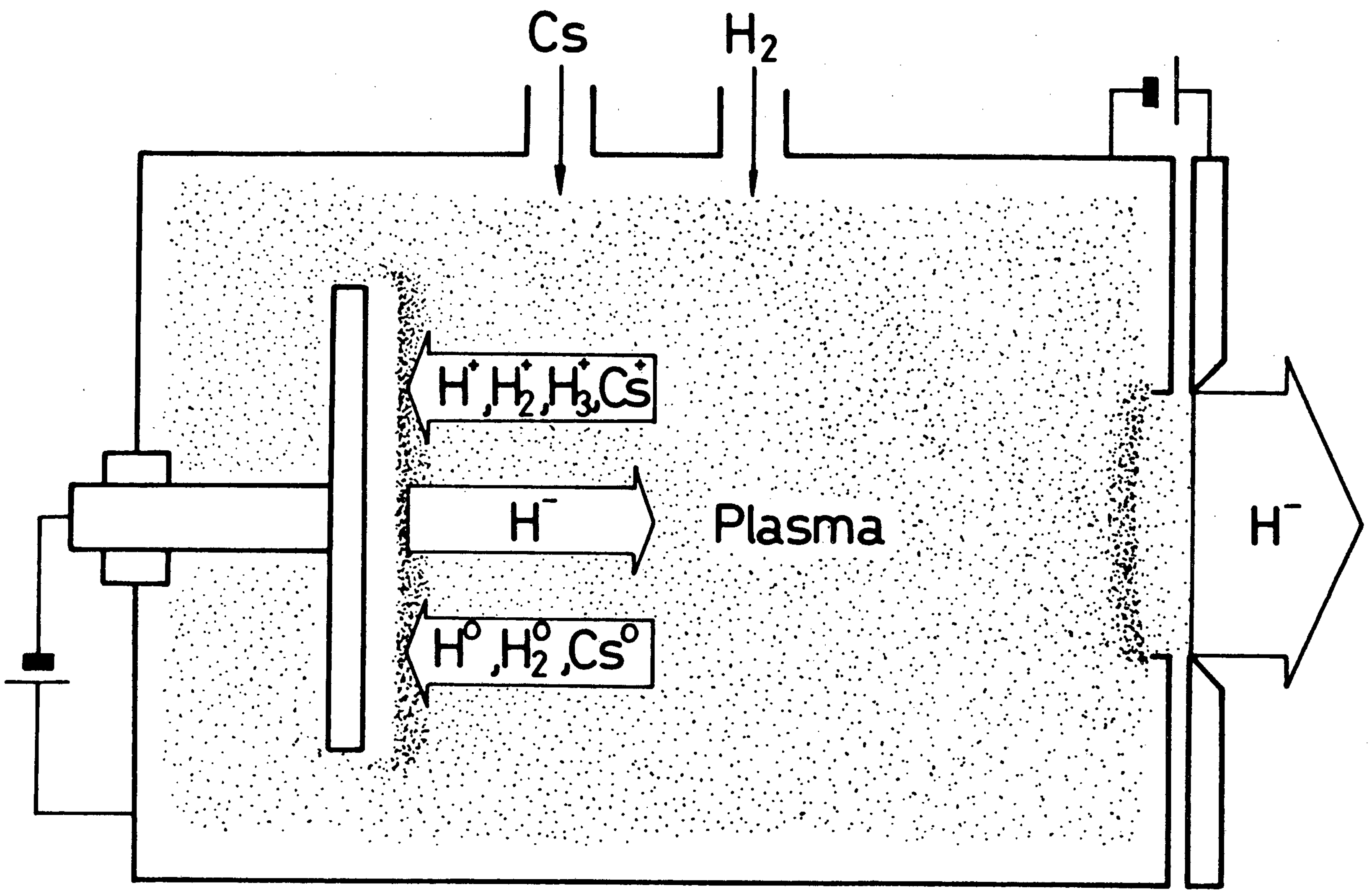

Fig. 1

XBL 832-8200

scattering of hydrogen ions and neutrals and surface desorption of adsorbed hydrogen atoms by energetic particles from the plasma.

The formation of atomic hydrogen by the back scattering of hydrogen ions is the most distinct process. Protons and molecular hydrogen ions incident on the surface are neutralized or dissociated at the surface, and after one or several collisions, they are scattered back to free space. Because the energy of the incident particle is equal to the difference between the plasma potential and the surface, the energy distribution as well as the total particle reflection co-efficient of the incident hydrogen ions can be computed by setting up the proper model for the process. For example, Oen and Robinson[12] have developed a code to calculate the velocity and angular distribution of hydrogen isotopes back scattered from polycrystaline metals. This code was actually used by Hiskes and Schneider[13] to interpret the experimental data of H^- production by back scattering.

Back scattering of neutral hydrogen atoms can be a very efficient process to produce H^- ions. The following collisions in the plasma are responsible for the production of atomic hydrogen with energies below several eV.

$$H_2 + e \rightarrow 2H + e$$

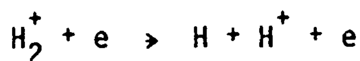

$$H_2^+ + e \rightarrow H + H^+ + e$$

$$H_3^+ + e \rightarrow H_2^+ + H + e$$

$$H_2^+ + e \rightarrow H + H$$

$$H_3^+ + e \rightarrow H_2 + H$$

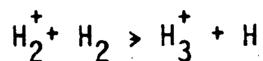

$$H_2^+ + H_2 \rightarrow H_3^+ + H$$

An experimental study of the H^- production by back scattering of low energy atomic hydrogen was done by Graham[14]. The reported efficiency for the process was not very high.

The particle reflection co-efficient and energy distribution of the back scattered hydrogen particles are dependent on the material of the substrate. For the surfaces in the cesiated hydrogen plasma, existance of adsorbed layer affects the back scattering parameters. We define the following parameters:

$f_0(v)$; Velocity distribution of atomic hydrogen.

$f_1(v)$; Velocity distribution of protons.

$f_2(v)$; Velocity distribution of H_2^+ ions.

$f_3(v)$; Velocity distribution of H_3^+ ions.

$G_0(v_0,v)$; Probability that an incoming atomic hydrogen with velocity v_0 will be back scattered from the surface with exit velocity v.

$G_1(v_1,v)$; Probability that an incident proton with velocity v_1 will be back scattered from the surface with exit velocity v.

$G_2(v_2,v)$; Probability that an incident H_2^+ ion with velocity v_2 will be back scattered from the surface with exit velocity v.

$G_3(v_3,v)$; Probability that an incident H_3^+ ion with velocity v will be back scattered from the surface with exit velocity v.

Here the G_i are functions of the hydrogen and cesium coverage. Denoting the hydrogen coverage and the cesium coverage on the substrate by θ_H, and θ_{Cs}, respectively, the velocity distribution of the outgoing atomic hydrogen flux from the surface can be written for the back scattering process as:

$$F_b\ (v) = \sum_{i=0}^{3} \int_0^\infty f_i(v_i)\ G_i\ (v_i, v, \theta_H, \theta_{Cs})\ dv_i \qquad (2\text{-}1)$$

Desorption of atomic hydrogen from the surface is more directly connected to the amount of hydrogen adsorbed on the surface.
When energetic particles impinge on the surface, an adsorbed hydrogen is likely to be desorbed from the surface in the form of atomic neutrals.[15] Similar to the case of back scattering, we define the following cross sections:

$\sigma_1(v',v)$; Probability that an incident proton with velocity v' ejects the atomic hydrogen with velocity v from the surface.

$\sigma_2(v',v)$; Probablity that an incident H_2^+ ion with velocity v' ejects the atomic hydrogen with velocity v from the surface.

$\sigma_3(v',v)$; Probability that an incident H_3^+ ion with velocity v' ejects the atomic hydrogen with velocity v from the surface.

The final velocity distribution of atomic hydrogen due to desorption can be written:

$$Fd(v) = \sum_{i=1}^{4} \int_{0}^{\infty} \theta_H fi(v_i) \sigma_i(v_i, v) dv_i \tag{2-2}$$

Neglecting the contribution from other processes, we may write the final velocity distribution function by simply adding (2-2) to (2-1).

(2-2) Formation of H^- at the surface.

For an atomic hydrogen to be an H^-, it must capture an electron from the surface. After the electron capture, the H^- must leave the surface without transferring the electron back to the metal surface. To describe this process, we define the formation probability P_f, which is the probability for an atom to capture an electron from the metal substrate, and the survival probability P_s, which is the probability for an H^- to leave the metal substrate without losing the captured electron. These probabilities are dependent upon work function, and the hydrogen atoms velocity component normal to the metal surface. Using these probabilities, the distribution function of the H^- ion can be expressed as:

$$f(v) = P_f(v_n)\, P_s(v_n)(Fb(v) + Fd(v)) \tag{2-3}$$

where v_n is the velocity of the H atom perpendicular to the surface.

When the electron affinity of the atom is lower than the work function of the metal, an electron in the conduction band can be transferred to the atom in the vicinity of the metal surface. For the case of hydrogen, the electron affinity is 0.75 eV but work

functions of ordinary metals, including alkali-metal covered surfaces are not as low as this value. However, when an atom approaches a surface, it weakly interacts with the metal, and electrons can tunnel between the atom and the solid. This process will shift and broaden the electron affinity states to be a narrow band as it is illustrated in Fig. 2. The tail of this state may overlap the Fermi level of the metal, and the tunneling of an electron from the metal to the atom becomes possible. If the alkali metal is adsorbed on the surface, then effective electron affinity of the hydrogen atom can be that of alkali halides, which is larger than .75 eV.[17]

We define X_o as the distance at which the electron affinity of the hydrogen becomes equal to the work function. for example, if only the shift of electron affinity by the image potential is considered, X_o can be written :

$$X_o = \frac{e^2}{4(\phi_w - E_a)}$$

where E_a is the electron affinity of the free atomic hydrogen, e is the unit charge of the electron and ϕ_w is the surface work function. In the region of $X < X_o$, electron transfer from the Fermi level to the electron affinity of the H atom is energetically possible. When $X < X_o$, some of the produced H^- are neutralized by electron transfer back to a surface, and using this separation X_o, we can write the formation and survival probability as:

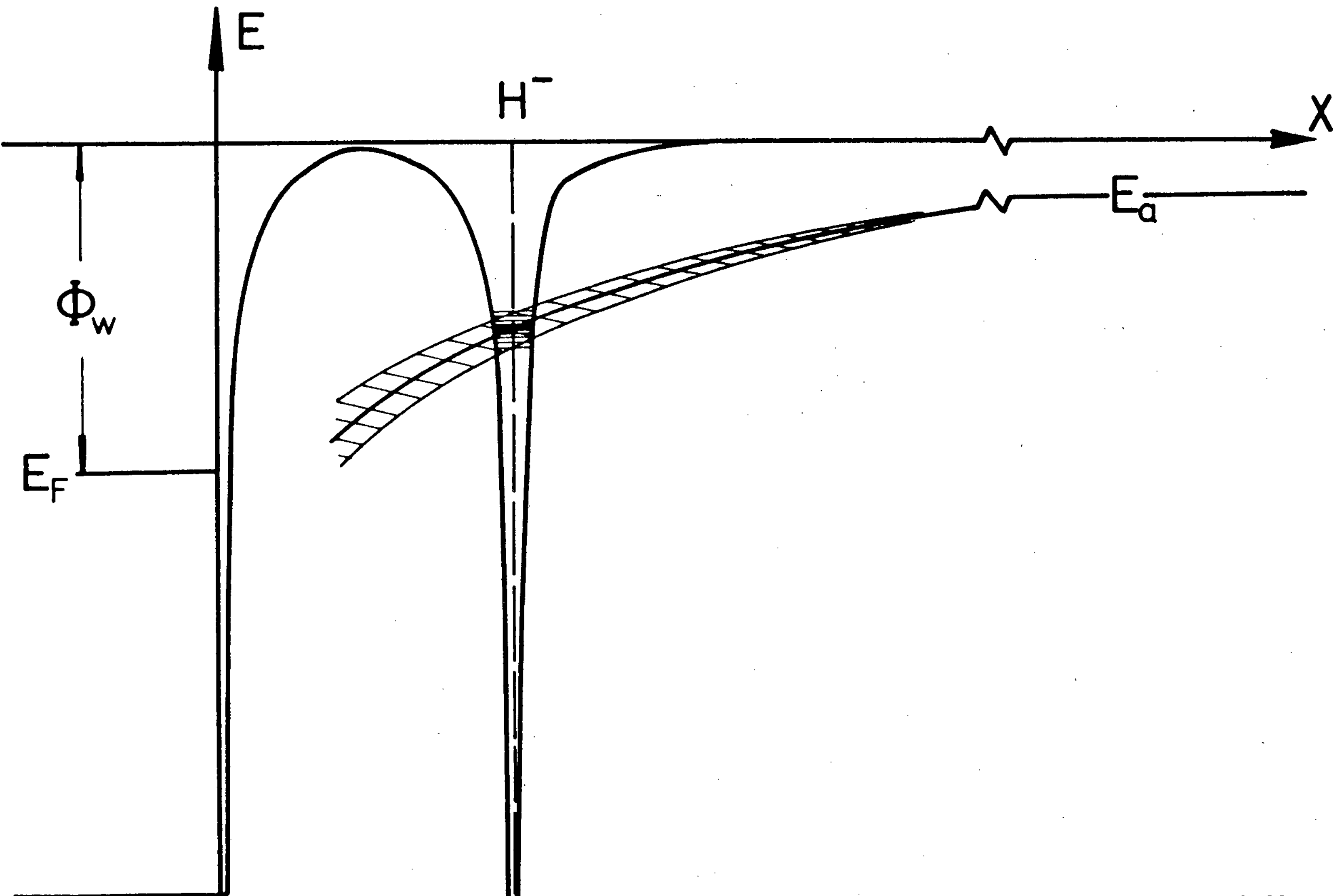

XBL 832-8199

Fig. 2

$$P_f(v) = 1 - \exp(-\frac{1}{V_n}\int_0^{X_0} P(x)\, dx)$$

$$P_s(v) = \exp(-\frac{1}{V_n}\int_0^{X_0} Q(X)\, dx) \qquad (2\text{-}4)$$

where P(X) is the rate at which an H atom is converted to an H^- at the distance X, and Q(X) is the rate at which an electron is transferred back from H^- to the metal. Rasser et.al.[8] included the probability of tunneling from the metal to the atom at larger distance than X_0. In this case, the range of integrations for both formation and survival probabilities is from 0 to infinity.

Probabilities P(X) and Q(X) can be derived as the solution to the steady state problem. The destruction probability Q(X) was approximately calculted by Janev[5,18] and by Kishinevskiy.[6] The geometry is schematically shown in Fig. 3-a. Hiskes and Karo calculated the survival probability by numerically solving for Q(X). They showed that when the Cs adlayer forms a surface dipole as it is shown in Fig. 3-b, the survival probability can be pratically unity for a tungsten surface covered with a partial monolayer of Cs. Figure 4 shows this comparison between geometries A and B shown in Fig. 3 together with the result by Kishinevskiy.

Because the formation probability is sensitive to the potential profile near the surface, which is not well known in many cases, the theoretical estimation of the formation probability is more difficult than the survival probability. Rough estimation of the formation probability was given by Hiskes and Karo as nearly 100% at

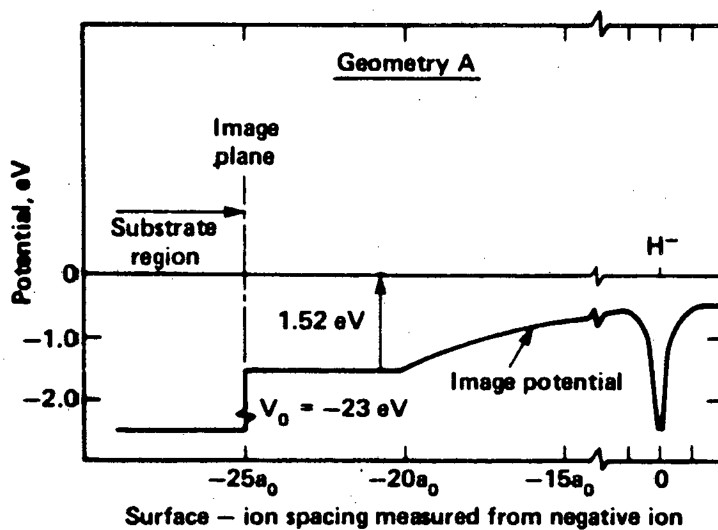

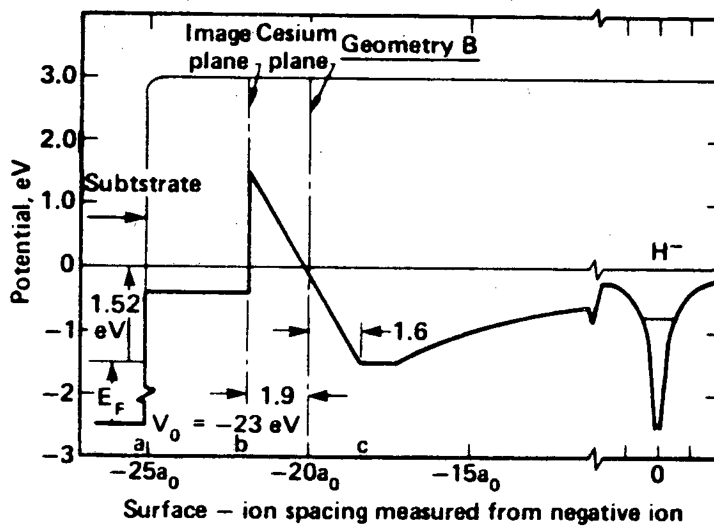

XBL 803-8748

Fig. 3

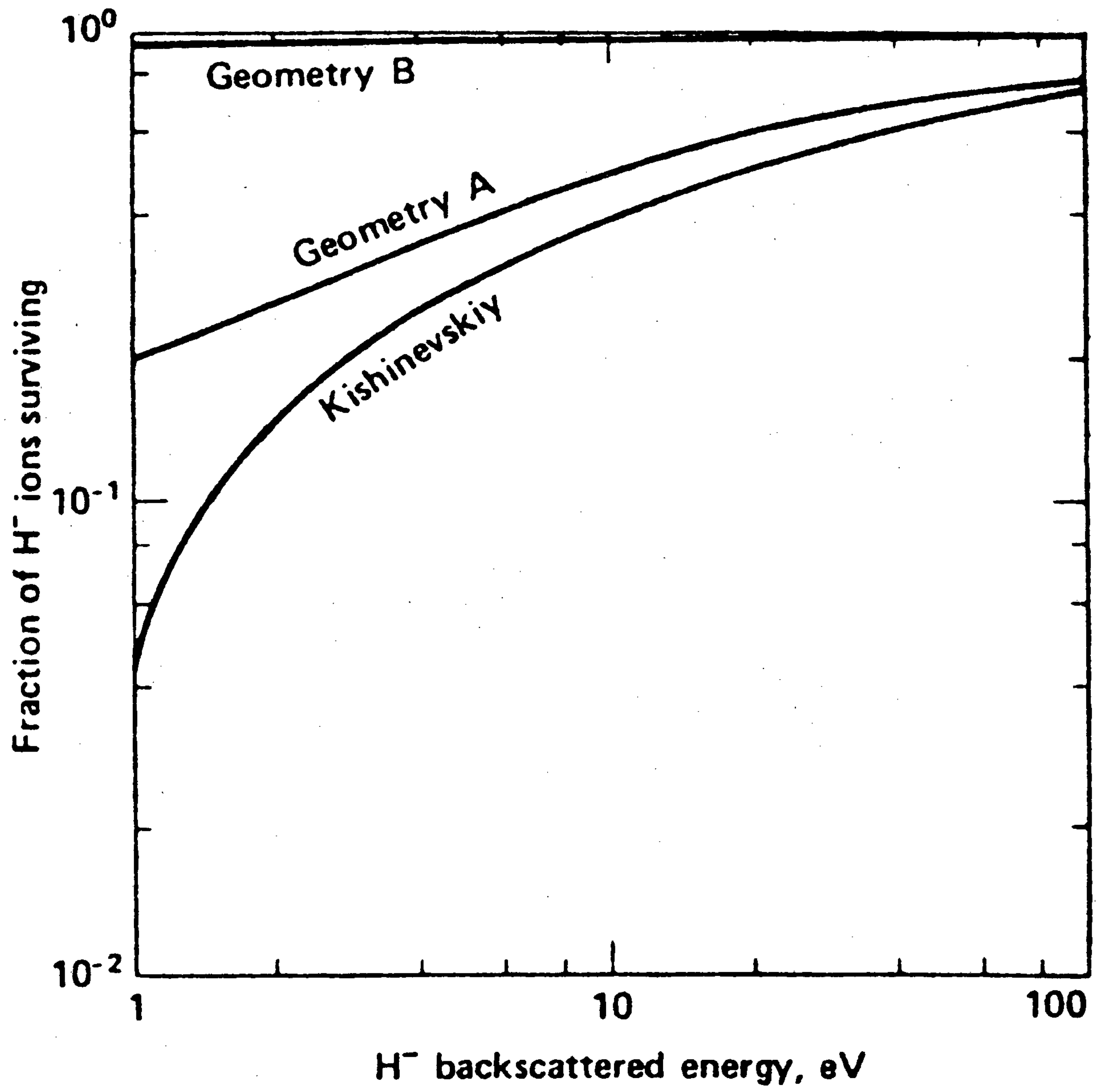

XBL 803-8645

Fig. 4

1 eV to 50 % at 100 eV, for tungsten covered with a partial monolayer of Cs. In order to simplify the calculation of the low energy H^- production at low work function surface, the formation probability is sometimes assumed to be unity. This assumption should be valid if the escape velocity of H^- is only a few eV and the surface work function is close to 1 eV. Also, for the case of desorption of H^- by energetic particles, only the survival probability will be necessary since the H^- is already formed while on the surface.[10]

(2-3) Transport of H^- Ion Beam in the Plasma

After acceleration across the sheath, some H^- are lost by collisions with plasma particles before the beam goes out of the ion source. The following collisions are responsible for the destruction of H^-:

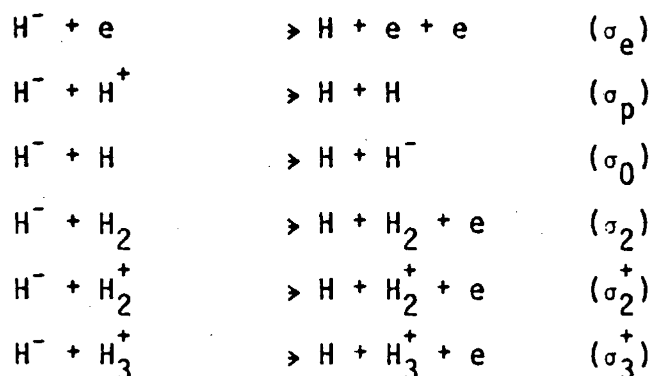

$$H^- + e \rightarrow H + e + e \qquad (\sigma_e)$$
$$H^- + H^+ \rightarrow H + H \qquad (\sigma_p)$$
$$H^- + H \rightarrow H + H^- \qquad (\sigma_0)$$
$$H^- + H_2 \rightarrow H + H_2 + e \qquad (\sigma_2)$$
$$H^- + H_2^+ \rightarrow H + H_2^+ + e \qquad (\sigma_2^+)$$
$$H^- + H_3^+ \rightarrow H + H_3^+ + e \qquad (\sigma_3^+)$$

some of the above listed cross sections are shown in Fig. 5. As a result of the loss in the plasma, the velocity distribution of the H^- current can be written as:

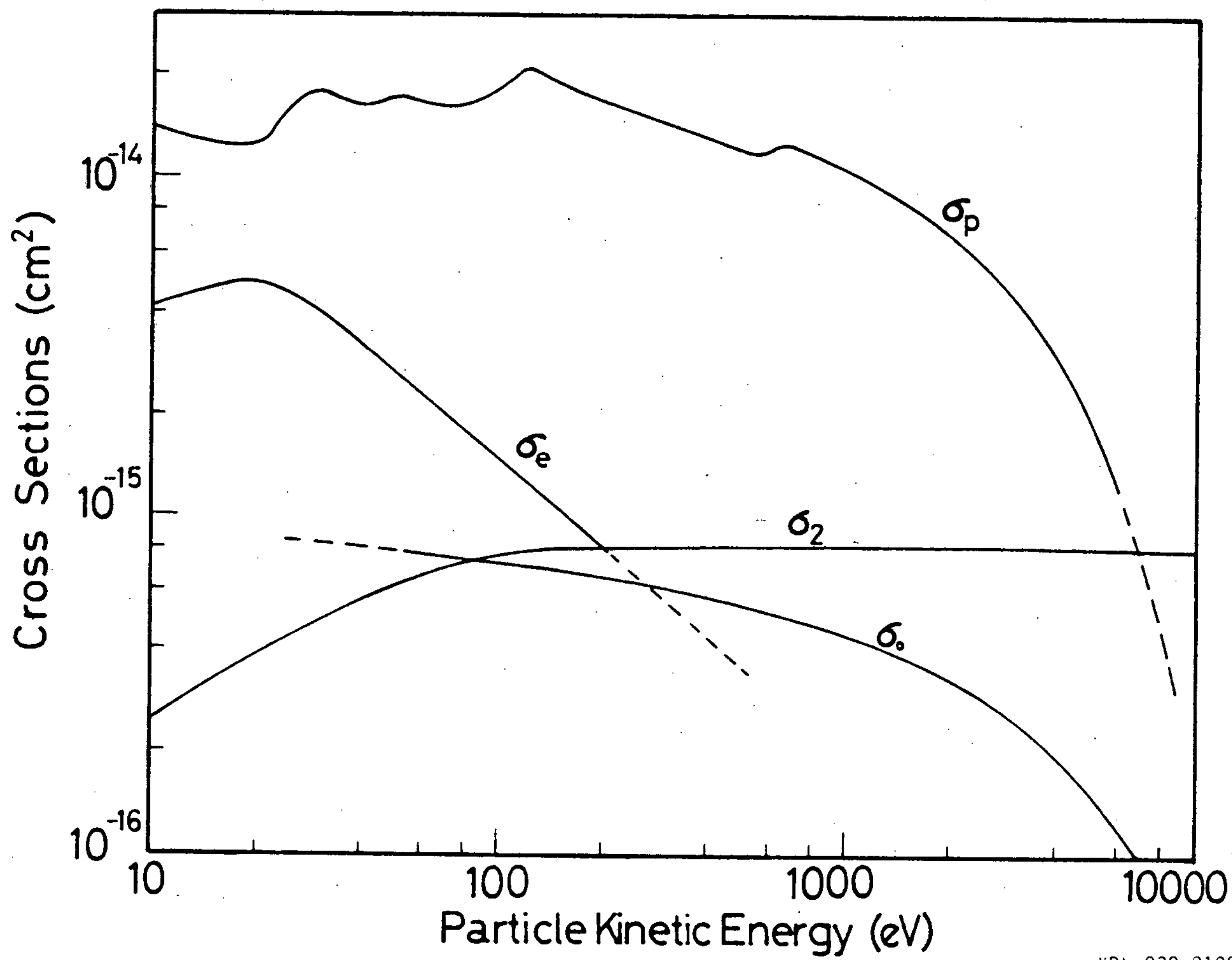

Fig. 5

$$f'(v,x) = f(v)\exp\left[-\int_0^X dx\left(\frac{n_e\langle\sigma_e V_e\rangle}{V} + n_o\sigma_o + n_2\sigma_2 + n_p\sigma_p + n_2^+\sigma_2^+ + n_3^+\sigma_3^+\right)\right] \quad (2\text{-}5)$$

The above equation is good for one dimensional geometries. If the effect of size and shape of the metal surface is to be taken into consideration, the distribution function should be written:

$$f'(\vec{v},\vec{x}) = f(\vec{v},\vec{x} - L\frac{\vec{v}}{v})\exp\left[-\int_0^X dx\left(\frac{n_e\langle\sigma_e V_e\rangle}{V} + n_e\sigma_o + n_2\sigma_2 + n_p\sigma_p + n_2^+\sigma_2^+ + n_3^+\sigma_3^+\right)\right] \quad (2\text{-}6)$$

The total H^- current is now given by the integration of above distribution function, and is:

$$I_H^- = \int dS\, dV\cdot V\, f_{(x,v)}$$

CHAPTER 3

EXPERIMENTAL APPROACH AND APPARATUS

(3-1) Experimental Approach

Because the surface production of H^- is determined by the discharge and the surface conditions, the method of measuring the work function must not affect these conditions. Since the moderate intensity photon beam in the visible range does not affect the plasma nor the surface, photoelectron emision is suitable for determining the work function of the H^- production surface. As it is shown in Appendix 1, the work function can be determined by measuring the photoelectron current and the incident photon flux at the given photon energy. The form of the equation is:

$$Y = (\text{phoeoelectron current})/(\text{incident photon flux})$$

$$\propto \quad (h\nu - \phi_w)^2 \;/\; (E_F + \phi_w - h\nu)^{1/2}$$

where,
- Y; photoelectron quanmtum yield.
- $h\nu$; incident photon energy
- ϕ_w; the surface work function
- E_F; Fermi level of the surface.

By assuming the absorptivity of the surface to be nearly constant, the plot of the square root of the quantum efficiency against the

photon energy gives a straight line which intersects at the work function.

Before applying this method to the surface in the plasma, several basic characteristics of the photoelectron emission were studied for the alkali-metal covered surfaces in an ultra high vacuum system (Appendix 2). Because the measured quantum efficiency was less than 10^{-4}, photoelectron current for a monochromatic light from the ordinary light source was not expected to be much larger than 10^{-6}A. When the surface is immersed in the plasma, the plasma noise will be imposed on this relatively small photoelectron current. To do the measurement with a reasonable accuracy, three major requirements were imposed in designing the experimental system: First, suppression of the plasma noise; second, maximization of the incident light intensity on the surface; and third, the signal detection system that can discriminate photoelectron current from the plasma noise.

Since the H^- production surface is biased negative with respect to the plasma, the total current that flows the surface is composed of the plasma ion current, photoelectron current and the current from secondary emission of negative charged particles. Provided the bias voltage to the surface and the surface condition are stable, the noise on the current is most likely caused by the density fluctuation of the plasma ions. Because this noise can be assumed to be proportional to the surface area, noise to the surface can be reduced by minimizing the surface area. As the magnetic line cusp geometry is reported to confine a plasma quietly[20], a small

metal surface in the multiline cusp device was chosen as the target. At the same time, the ion source was designed with a large diameter of the vacuum window and a short distance from the window to the target to collect the incident light efficiently on the target.

To obtain the reasonable intensity of the incident light beam, we need a light source with a high brightness. Because a grating monochromator gives an elongated beam shape with a spatially dependent spectral intensity, an interference filter monochromator was considered to be more appropriate. The design of the monochromatic light source should take the method for signal detection into consideration. For example, because the phase sensitive signal detection by modulting the light beam is necessary, the effect of the position and the size of the light beam modulator on the divergence, polarization and intensity of the beam had to be investigated. We chose the light modulation by a mechanical chopper to produce a 50% duty cycle light pulse to detect the signal using a simple lock-in amplifier.

The momentum analyzer was considered to be more appropriate to detect the H^- current than an electrostatic energy analyzer, because impurity negative ions are also produced with a similar energy to H^- at the surface. Because we were interested in the velocity distribution as well as the total current of H^-, the differential momentum spectrum was measured during the experiment and the total current was computed following the simple formula explained in Appendix 4. It should be noticed that the distribution

measured by the momentum analyzer is f'(v,x) in equation (2-6) instead of the original distribution function of the H^- produced at the surface. The beam attenuation by the transport in the plasma, and the geometrical sensitivity of the momentum analyzer should be considered if one wants to know the original distribution function $f_{(v)}$ in Eq. (2-3). The attenuation of the beam by the charged particles cannot be a serious problem provided the electron and atomic hydrogen densities are below 10^{12} cm^{-3}, as it is seen from the cross section data in Fig. 5. When the H_2 neutral density is 3×10^{13} cm^{-3}, mean free path of H^- is about 40 cm for H^- attenuation by H_2 molecules. But as it appears in Fig. 5, σ_2 is almost constant from 100 eV to 1 keV, and attenuation by H_2 will be nearly the same for all energies causing negligible effect on the energy spectrum measurements.

In addition to the work function and H^- current, other plasma parameters should be measured during the experiment. An ion gauge and a Langmuir probe were used to monitor the neutral pressure and the electron density, and the momentum analyzer was occasionally used as the mass analyzer to investigate the species composition of positive ions. Simplified diagram of the experiment is illustrated in Fig. 6, and each component is described in detail in the next section.

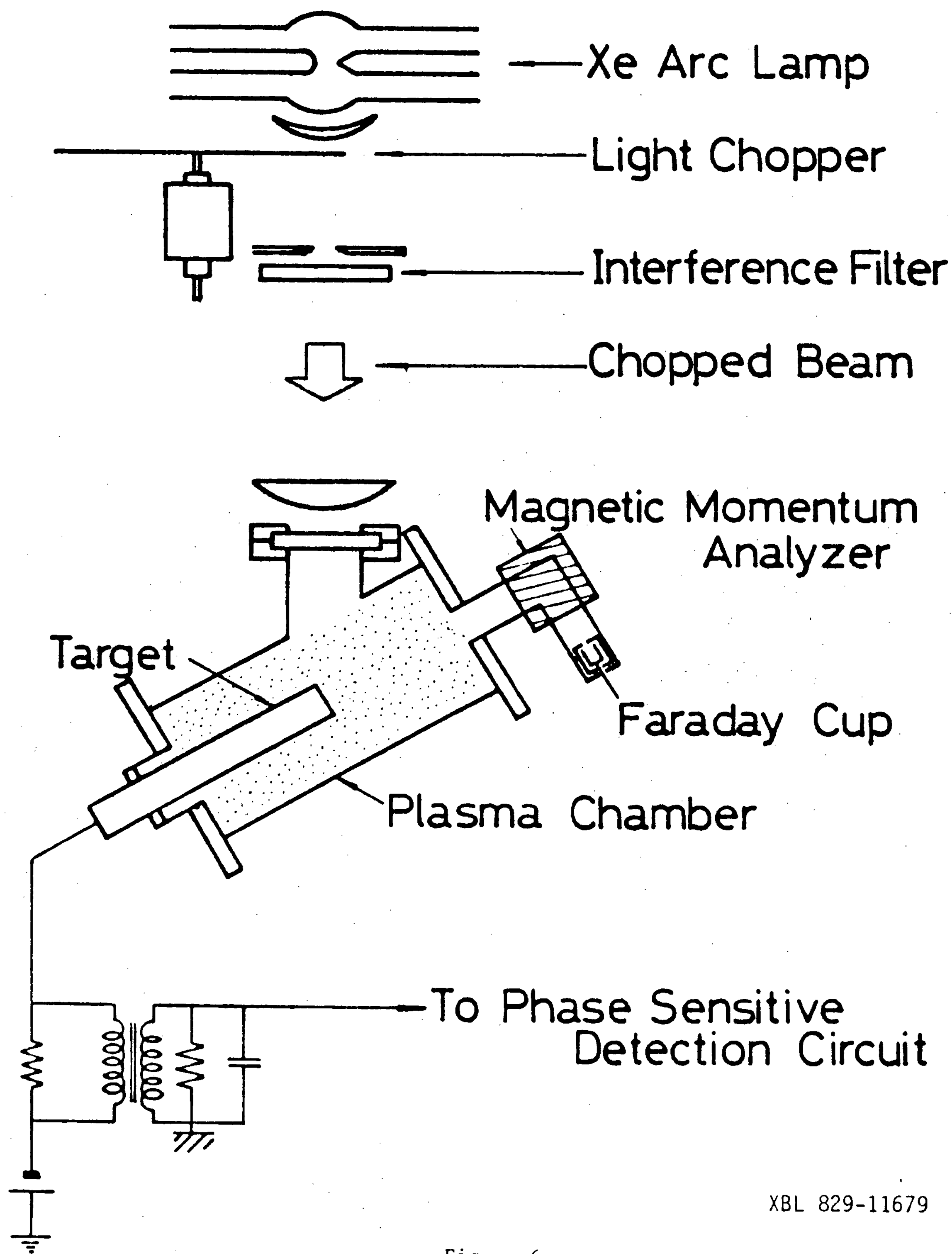

Fig. 6

(3-2) Apparatus

(1) Ion Source

A 15 cm diameter 18 cm long stainless steel chamber was used as the plasma container. This vessel was surrounded by 6 columns of samarium cobalt magnets to form full line cusp geometry. These magnets were placed in a water cooled manifold that touched the source chamber wall with a small contact area. Because the cooling of the source chamber wall was indirect, the wall temperature was kept higher than 80°C by the filaments and the discharge radiation heating, and this high wall temperature made the efficient Cs recycling in the ion source possible. One through four of .05 cm diameter tungsten wire was used as the hot cathode, and the entire chamber wall was grounded to serve as the anode of the dicharge. The ion source chamber was pumped by 250 l/s turbo molecular pump through a 25 l/s pumping impedance.

The copper target was the front face of a water cooled copper rod with a surface area of 1 cm^2 which was used as the surface to produce H^-. At the back of this rod, a chromel-alumel thermocouple was attached to monitor the temperature through a high voltage isolation amplifier. The Mo target was made of a 1 mm thick Mo disk which was brazed on the front end of another Cu rod of identical design. A schematic drawing of these targets are shown in Fig. 7. These targets were mounted inside of the chamber with a quartz glass shield to reduce the surface area exposed to the plasma.

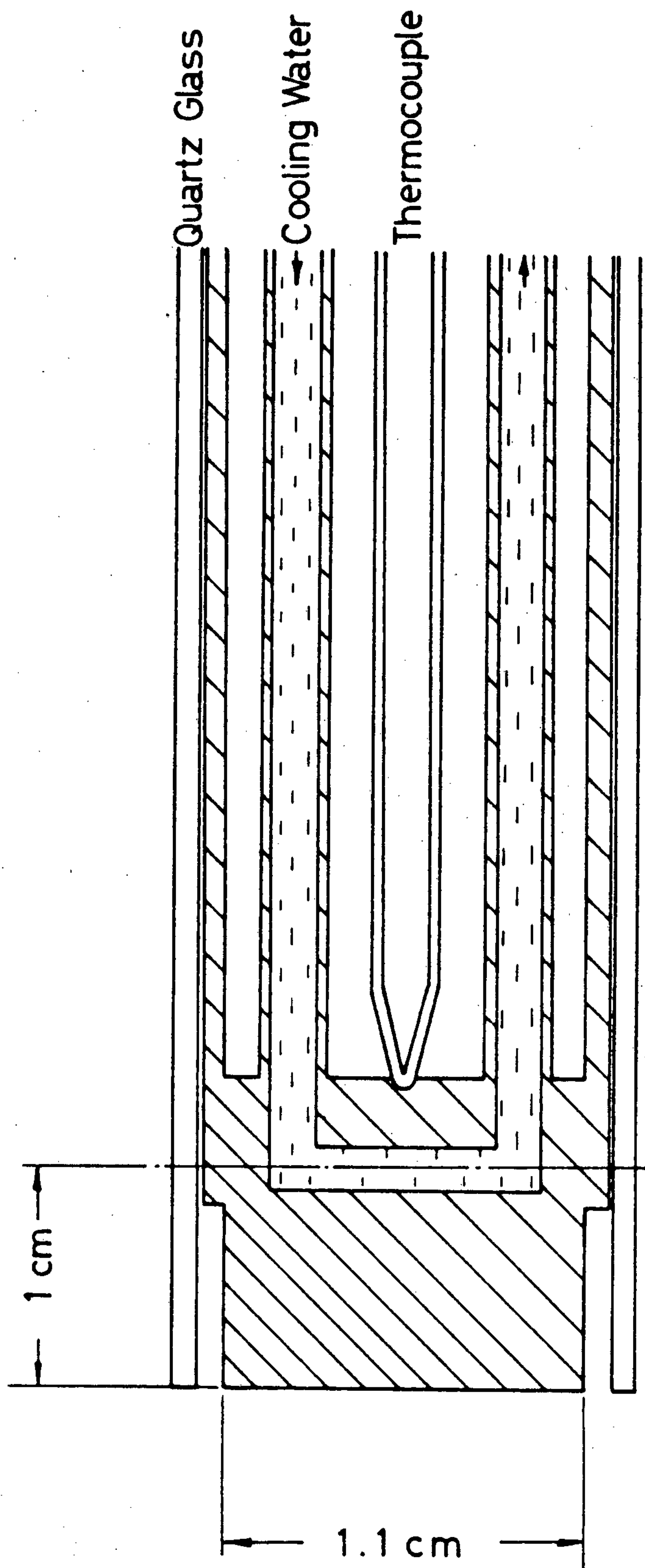

XBL 832-8230

Fig. 7

Hydrogen gas was introduced into the system by a slow leak needle valve. Usually, Cs was introduced by a compact Cs oven, the structure of which was drawn in Fig. 8. The Cs level of the discharge was adjusted by controlling the current of the heater wire of the oven. Quasi-steady state operaton of a cesiated hydrogen discharge up to the order of 10 minutes was possible with this oven. In some experiments, S.A.E.S. alkali metal getter dispensers were used. They were small slitted capsules which contained alkali metal compounds. Alkali metal vapor is released when the capsule which is made of nichrome is heated resistively, by an electrical current. Hydrogen pressure was monitored by an ion gauge, and Cs level was monitored through the measurement of surface produced H^- current or photoelectron current from the target.

In Fig. 9, an illustration of the entire chamber is shown. A typical plasma density of 3×10^{10} cm^{-3} was obtained for 1 A of discharge current with 80 V of discharge potential at 1 mTorr of hydrogen pressure. Quiescence of the discharge was investigated by measuring the ion saturation current of the target. The fluctuation of the ion saturation current was typically 0.4% of the D.C. ion saturation current for a pure hydrogen discharge. The plasma was quieter at higher pressures, and lower discharge current. The frequency spectrum of the noise was broad and flat up to 500 kHz. Homogenuity of the plasma was examined by measuring the ion saturation current to the Langmuir probes. Figures 10 and 11 are the results of this measurement. Probe bias was kept at -150 V. Because of the similarity of the atomic mass to Cs, Xe was used to

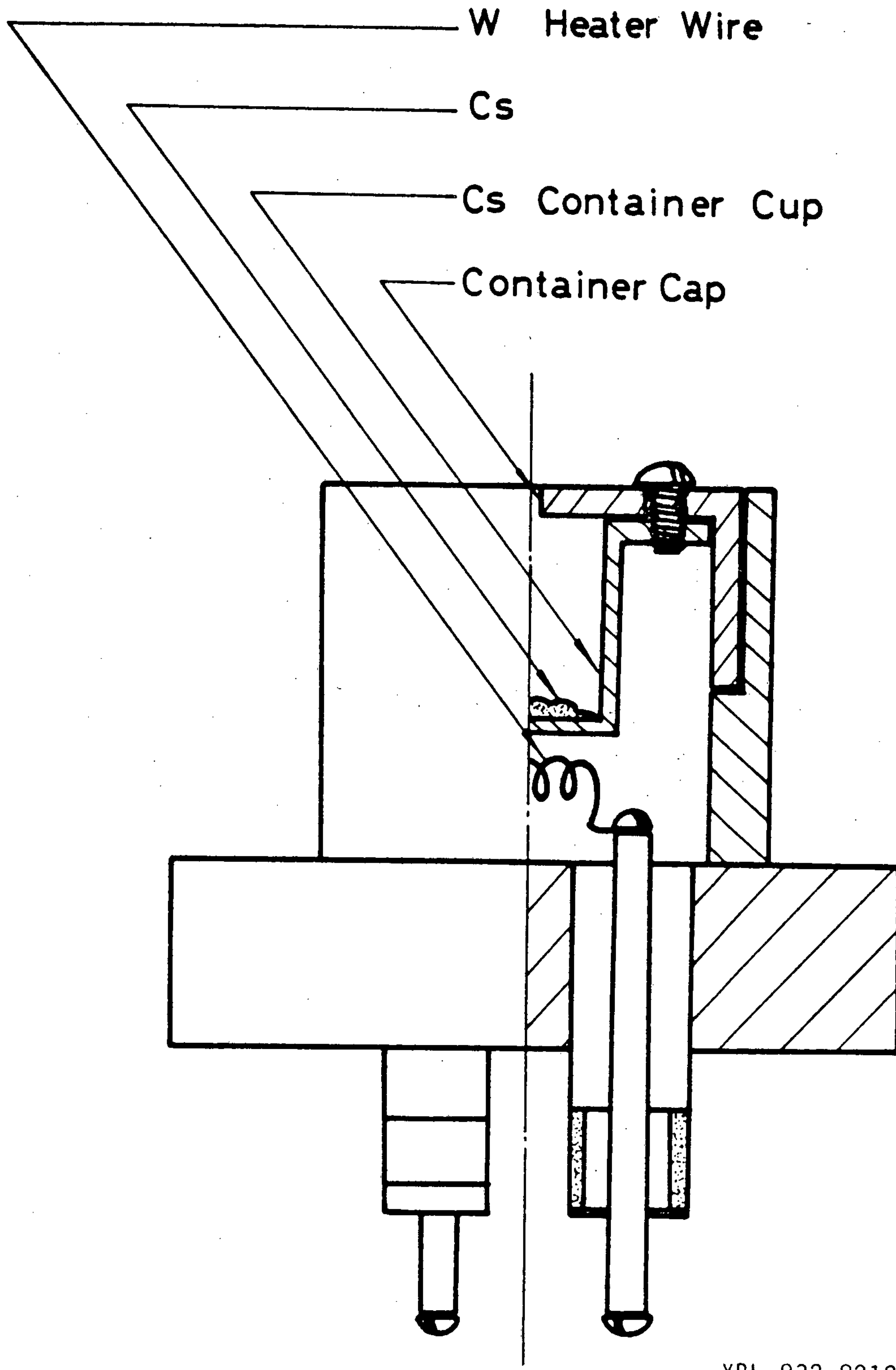

XBL 832-8212

Fig. 8

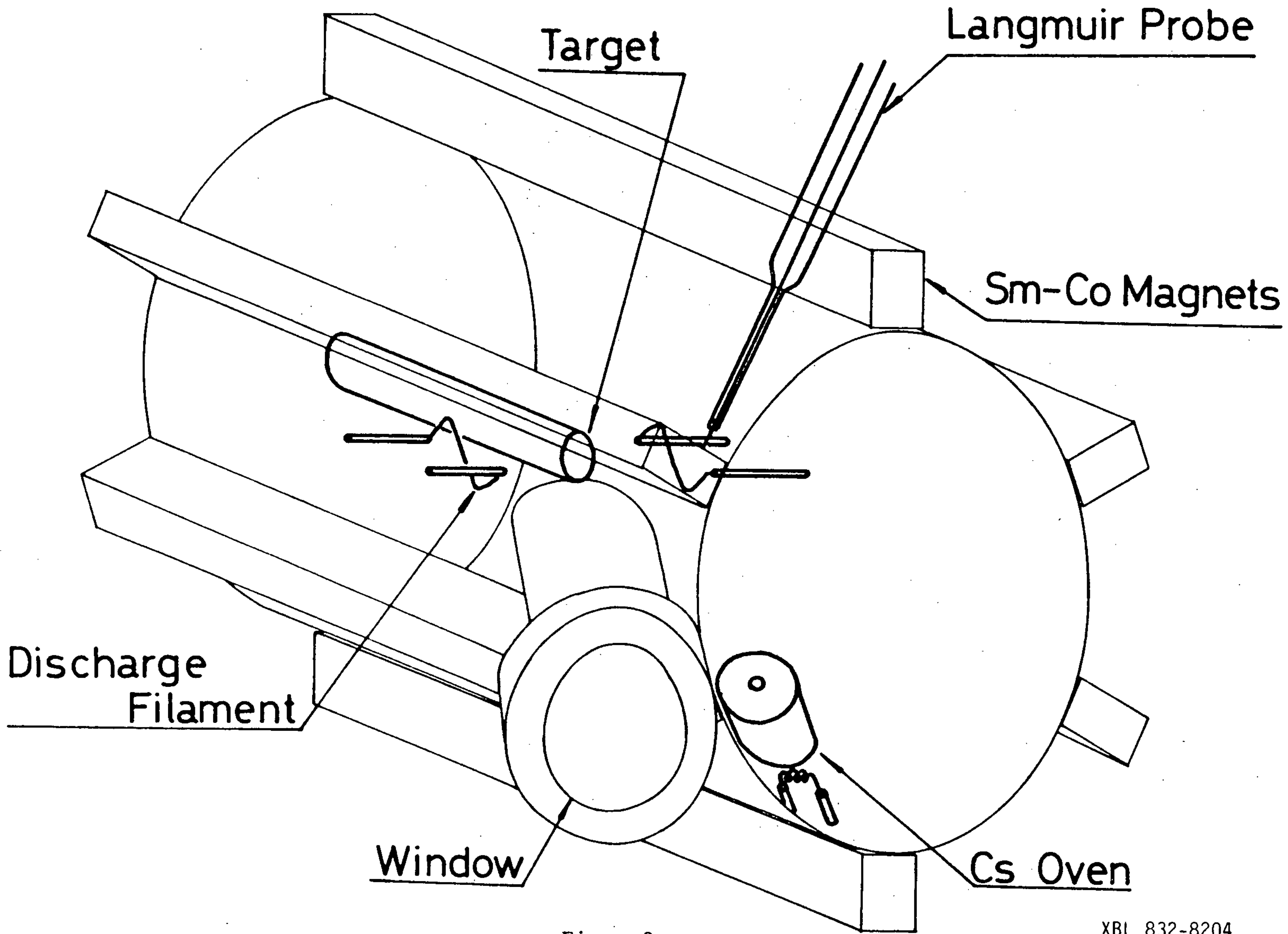

XBL 832-8204

Fig. 9

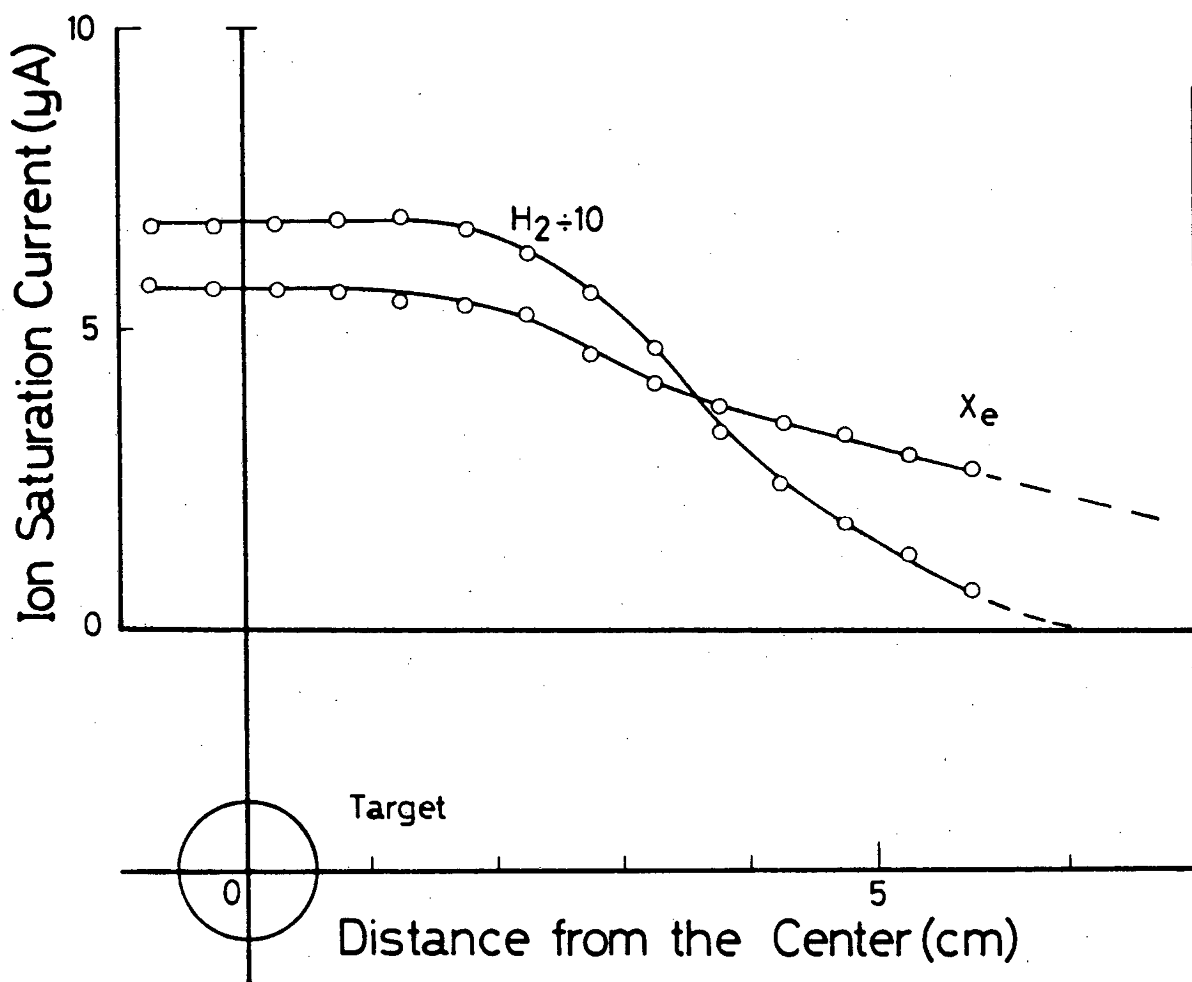

XBL 832-8196

Fig. 10

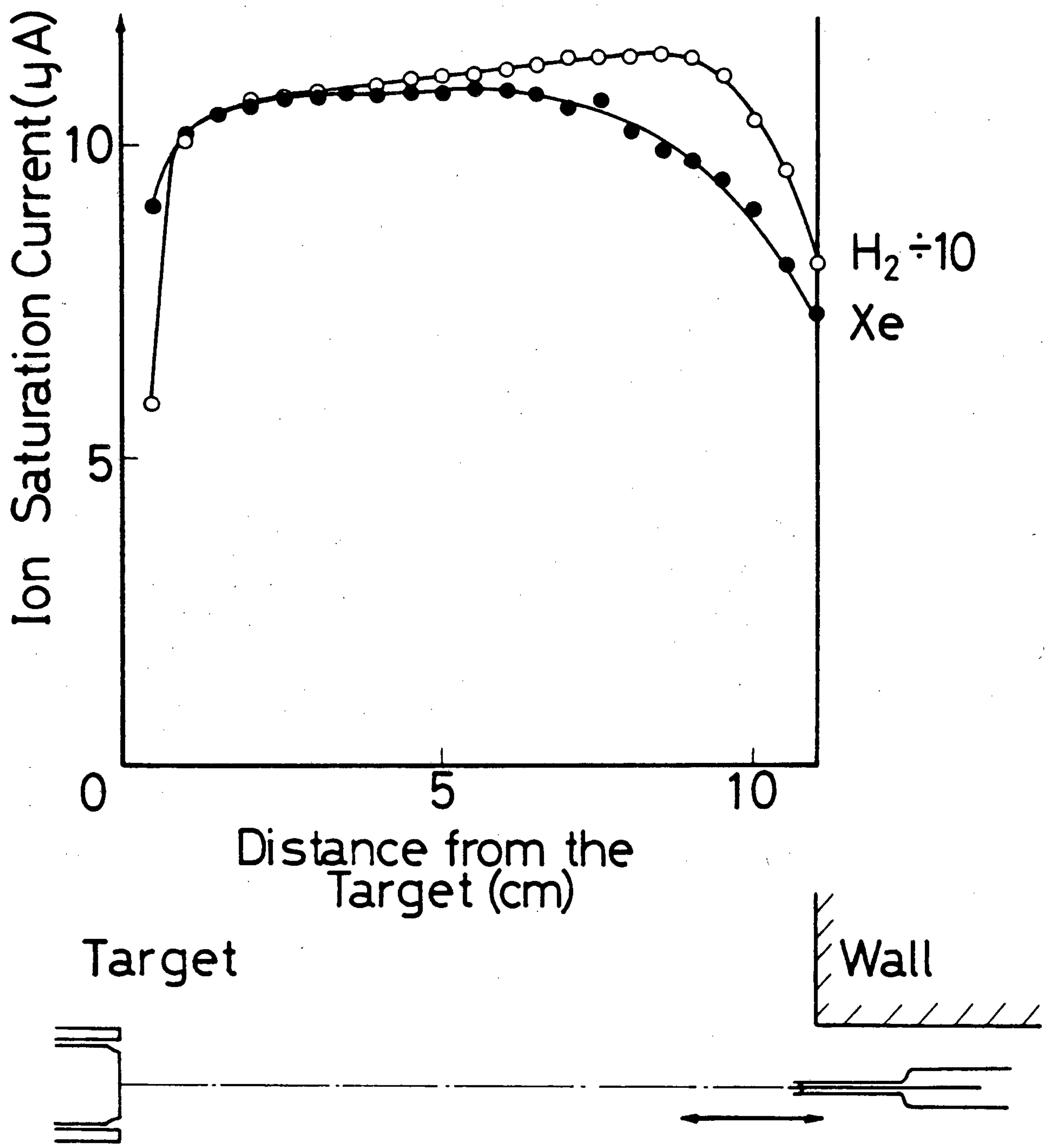

XBL 832-8197

Fig. 11

simulate the profile of a plasma with a high concentration of Cs. Homogenuity of the plasma was usually better for the case of a H_2 discharge than for a Xe discharge, which possibly suggested the less homogenuity of Cs plasma. Still, the target appeared to be illuminated homogeneously by the plasma even for the case of a Xe discharge.

(2) Light Source System

A 1 kW Xe arc lamp which has an image size as large as 3 mm high and 1.5 mm wide was used as the light source. The image was focussed on a 6 mm diameter circular beam limiter after removing the light with a wave length longer than 950 nm by means of a water filter. After this beam limiter, the power of the light beam was typically 1 W, which was a design limit of the interference filters. 10 nm band pass interference filters were mounted on a rotatable disk that can hold up to 24 filters, spanning the range of wave length from 300 nm to 900 nm. By plano convex fused silica lenses, this monochromatic light was focussed onto the target with an image size of approximately 6 mm high and 10 mm wide. For the ultraviolet range, the image size was confirmed to be within the target surface by observing the photoelectron current. In the infrared region, there was no way to confirm the image size, but up to 700 nm, the image was observed to be well within the target surface area. The incident light was chopped at the frequency from 550 Hz to 1.2 kHz by a rotating blade light chopper. This chopper also produced 0 to 10 mV electrical pulses by a light emitting and

light detecting diode pair. The signal was sent to the reference input of the lock-in amplifier through amplifier and comparator cirtuits. There was also a light chopper with fixed frequency of 18.9 Hz with identical structure as the high frequency chopper. This slow light chopper was used to measure the beam power by a large aperture pyroelectric detector. This detector with a 2.5 cm effective diameter was specially designed and made to detect the power of a light beam of large cross section. For details of this detector, see Appendix 5. Spectral intensity of the output light from the filter monochromator system was checked using a grating monochormator (Fig. 12). Typical output power and the peak wave length for each of the individual filters are listed in Table 1.

It was confirmed that 30 to 60 hours of plasma operation with a discharge power more than 300 W, caused appreciable change in transmissivity of the fused silica vacuum window. To avoid the accumulation of tungsten and cesium vapor on the surface, a stainless steel disk was used as the shutter; also, the window was replaced by a new one and the old window was checked to determine if its transmissivity had changed, after every 50 hours of source operation. No appreciable change in transmissivity was observed when the shutter was used.

(3) Momentum Analyzer

The H^- beam traveled through 11 cm of plasma before it hit the collimator of the compact momentum analyzer. After passing through the collimator, the beam trajectory was defined by two slits

which were coated with carbon paint to avoid charging by low energy beams. Because there was a substantial amount of residual magnetic field from the plasma confinement permanent magnets, the Larmour radius to analyze the ion beam was set as small as 3.2 cm. In addition, a 0.6 cm wall-thickness soft iron tube was used for the entire beam extraction section to minimize unwanted beam steering by the residual magnetic field. The schematic drawing of the momentum analyzer is given in Fig. 13. The analyzer was pumped by a 30 l/s compact low magnetic field ion pump. The geometrical resolution of the analyzer can be adjusted by the slits down to 1.5%. However, the analyzer was usually set to 2 % resolution because the uncertainty caused by space charge effects was more than 2%, as discussed in Appendix 4. The entire mass analyzer can be floated up to ±100 V for the beam extraction when necessary. For analysis of the ion species composition of the plasma, approximately 40 V was applied to achieve the right dispersion of the analyzer.

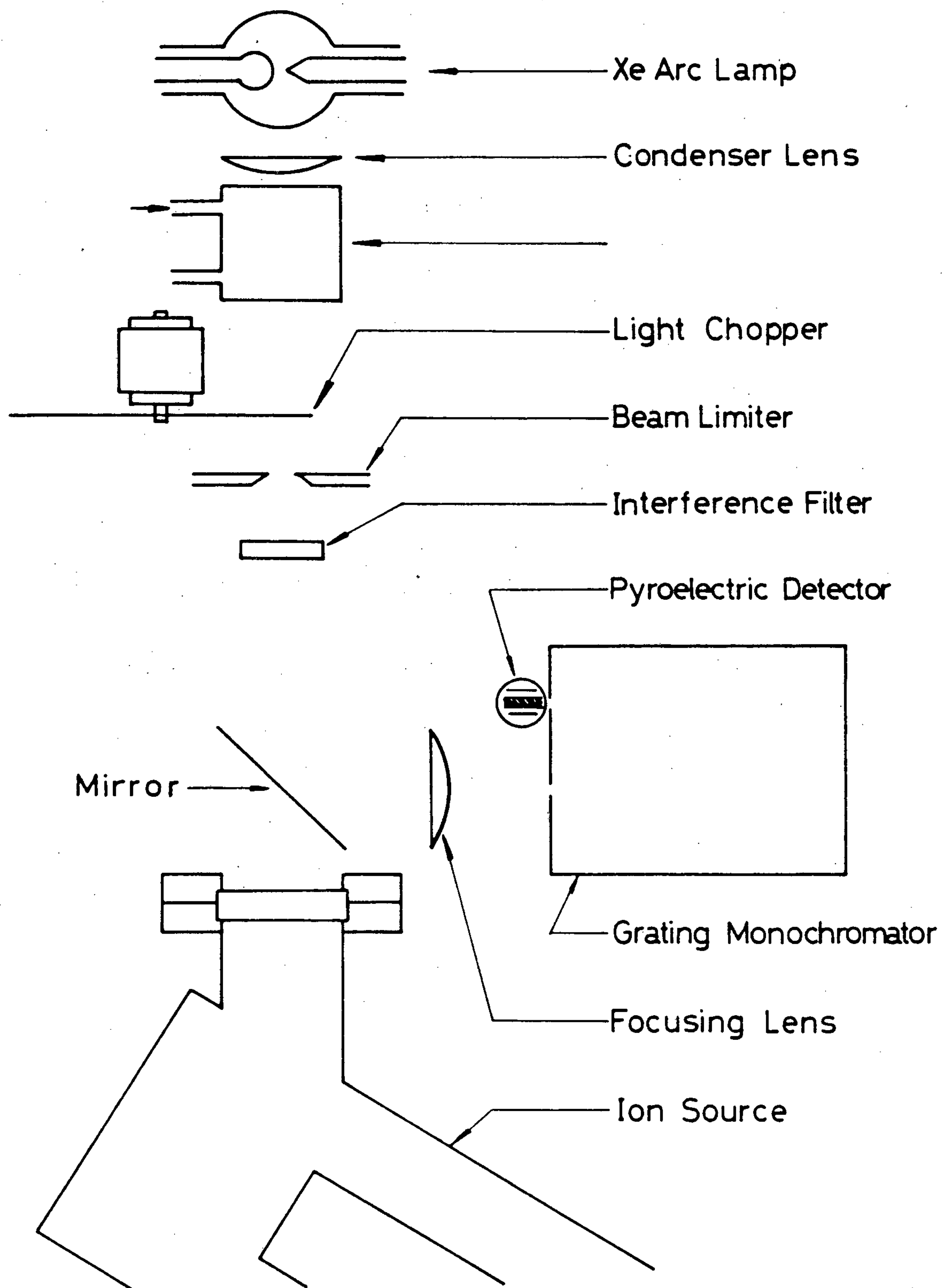

Fig. 12

TABLE 1. PEAK WAVE LENGTH AND TOTAL POWER FROM INDIVIDUAL INTERFERENCE FILTER

Filter Number	Peak Wave Length In nm	Total Beam Power in mW
1	Open	1000
2	304	2.1
3	321	2.2
4	341	3.2
5	366	4.0
6	380	4.3
7	400	5.7
8	418	7.8
9	438	9.3
10	460	10.0
11	477	6.4
12	499	7.2
13	519	7.7
14	538	7.1
15	558	7.6
16	578	7.0
17	599	7.6
18	618	8.3
19	635	6.7
20	659	7.1
21	678	4.6
22	698	4.9
23	748	3.2
24	798	3.5

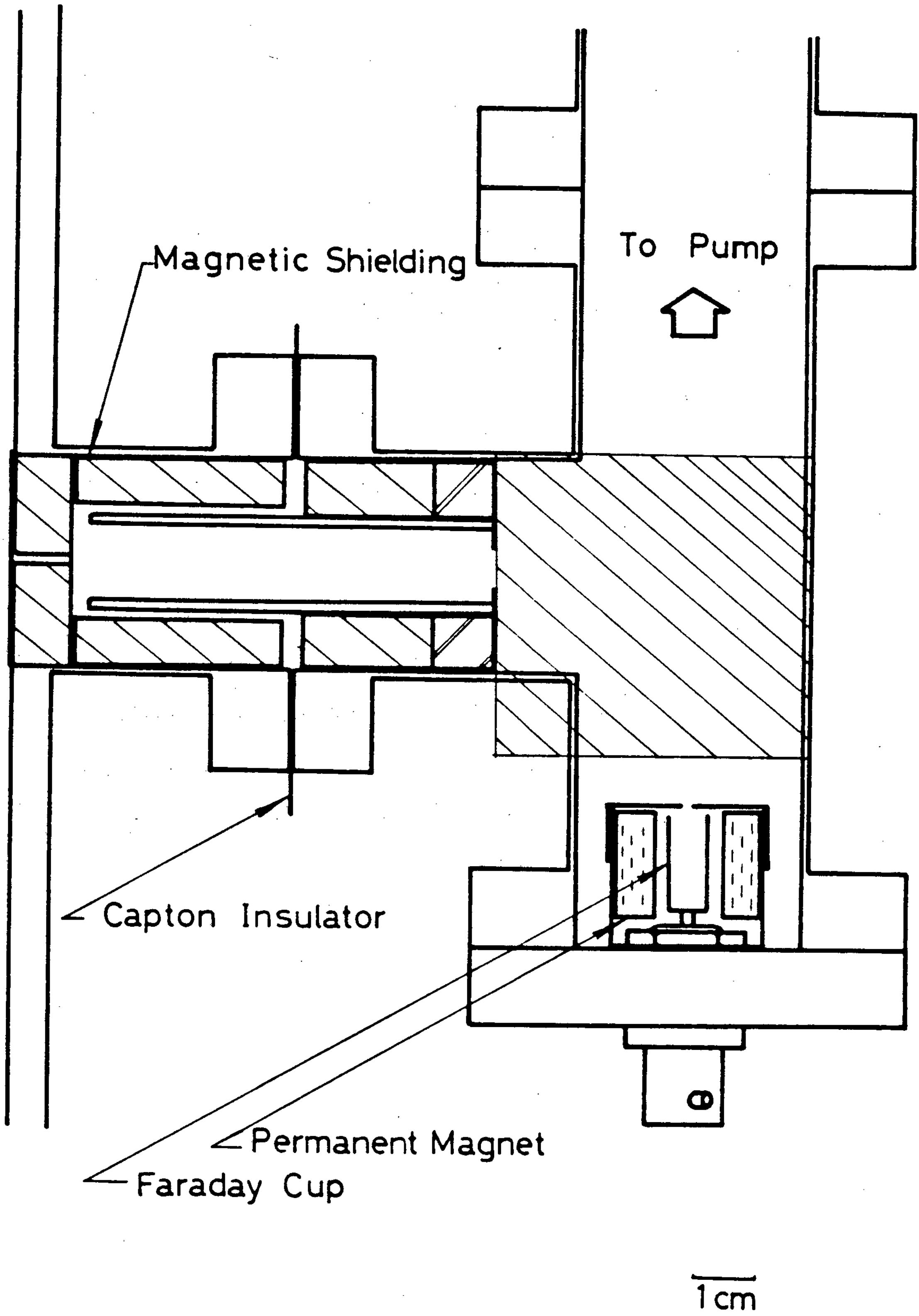

Fig. 13 XBL 832-8227

CHAPTER 4

EXPERIMENTAL PROCEDURE AND DATA ANALYSIS

(4-1) Experimental Procedure

To insure a consistent operation of the ion source, the following procedures were taken before each experimental measurement.

(1) Cleaning the ion source

(2) Cs loading.

(3) Start-up of the ion source

(4) Warm-up of the light source.

In many cases, only steps 3 and 4 were taken, because the ion source was originally clean and loaded with enough Cs.

(1) Cleaning the Ion Source

Cs inside of the ion source chamber absorbed residual impurity gases and accumulated them in the source, especially when the source chamber was opened up to atmosphere. As a large amount of impurity was accumulated in the chamber, a high concentration of impurity ions in the source plasma was detected on the mass analyzer. When either this was observed or too much Cs was accumulated in it, the chamber had to be cleaned.

To clean the source: Every flange was removed from the source chamber; the inner walls of the source chamber and the flanges were cleaned by distilled water, and then by ethyl alcohol; the surface of the target was mechanically polished and then cleaned with nitric

acid, acetic acid and ethyl alcohol; the discharge filaments were replaced by new ones; and the carbon coatings of collimators of the momentum analyzer were repainted. Cs oven was detached from the ion source and the residual Cs was cleaned out of the oven. Then the Cs container was chemically cleaned with nitric acid and acetic acid, and the entire oven was put in place of the ion source. After re-assembling, the ion source was pumped down to 10^{-6} Torr.

To further clean the ion source, the source was baked by the following procedure. The chamber wall and ports were heated by heat tapes and radiation from discharge filaments. The filament of the Cs oven was also turned on at this time to bake out Cs container. Baking power was slowly increased so that the source pressure did not exceed 1.5×10^{-5} Torr. This care was necessary because baking of the system at higher pressure sometimes caused carbon contamination of the system. The baking procedure required nearly 20 hours to bring the source pressure below 5×10^{-6} Torr at full baking power.

The chamber wall was further baked out by running a hydrogen discharge. After 30 minutes of hydrogen discharge with arc power maintained at 320 W, arc power and hydrogen gas flow were tuned off to pump down the system. Thirty minutes of continuous pumping brought the source pressure down to less than 5×10^{-6} Torr, then hydrogen flow and discharge power were turned on again. This procedure was continued until the sum of the impurity ion content monitored by the

mass analyzer fell below 5 % of the total ion current. The mass analyzer output during the baking discharge showed that the dominant impurity ions were O^+, OH^+, H_2O^+, H_3O^+ and CO^+. Usually, it took two days with 10 hours of a baking discharge to obtain a discharge with less than 5 % of impurity current. Base pressure after the baking was typically 1.2×10^{-6} Torr.

(2) Cs Loading of the Ion Source

Dry nitrogen gas was used to bring the chamber pressure up to atmosphere. The Cs oven was taken out of the chamber and put into a glove box which had been purged with Ar for more than 30 minutes to drive off air. From 0.2 to 2 grams of Cs (99.99% pure) was put into the Cs container cup of the oven (Fig. 8), and the container cup was covered with the cap. The whole Cs container cup was then dipped into liquid nitrogen for several seconds to minimize contamination from the atmosphere while in transit to the ion source. The container cup was then placed in the oven and the oven was taken out of the glove box. The Cs oven was carried in the atmosphere and was put in its position on the ion source, which had been continuously purged with dry nitrogen. Immediately after the oven was attached, the system was pumped down.

Two to three hours of pumping brought the ion source pressure down to about 10^{-6} Torr. To clean the impurities that might have possibly been adsorbed during the time of the Cs loading, the source chamber was baked with the same procedure as before, but with less

baking power. Baking with too much heat to the Cs oven caused the evaporation of Cs into the ion source before the clean up of the source chamber wall. The discharge power was kept below 50 W for the first 20 minutes of baking, and raised to 200 to 300 W in the final five minutes of baking. Then the discharge power and the filament power were turned off to remove heat, and the source chamber was pumped down for about an hour. Repeating this operation five to ten times brought the discharge plasma to less than 5% impurity ion current. As a final measure of the source cleanliness, impurity negative ions were monitored. During the initial stage of the baking discharge, the total impurity negative ion current was from 6 to 9 times larger than the H^- current. When the source was well baked, the H^- current was more than 40% of the total negative ion current.

(3) Starting up the Ion Source

Depending on the operation conditions, the ion source had to be baked for three to four minutes before the introduction of Cs into the discharge. If Cs had already been introduced into the ion source in a previous experiment, the impurity level was almost negligible even without a long baking discharge. After checking that the impurity level was small enough, (less than 5% without Cs, less than 1% with Cs), the discharge voltage, the discharge current, and the neutral pressure were set to desired values. The temperature of the source chamber wall was monitored by a thermo-couple, and after the wall temperature became constant, Cs was slowly introduced into the discharge.

With the indroducton of Cs, the species mix of the plasma changed. Impurity ions became almost negligible, and the H_2^+ decreased as H_3^+ increased. In accordance with the decrease of impurity positive ions, impurity negative ion current decreased to less than 1 to 10% of the total negative ion current. H^- current increased approximately two orders of magnitude with introduction of Cs at fixed arc power.

The H^- beam optics of the momentum analyzer were examined at this time. When it was the first run of the current Cs loading, alignment of the analyzer was tested. In case the axis of the anlayzer did not correspond to that of the beam, low energy H^- ion beams were steered very sensitively by applying a small extraction potential to the analyzer. This misalignment was adjusted by putting a flux return across the proper pair of rows of confinement magnets at the side wall of the ion source. Once this was done, misalignment of the beam was never again experienced. Charge up of low energy beams was also tested prior to every experiment. Beam energy was decreased down to less than 30 eV, and the small current was extracted from the souce to check if the current fluctuated due to the beam charge up. It took 150 hours of operaion time of the ion source until we found appreciable charge up of the beam.

(4) Light Source Operation

Collimation of the light source system was usually done when the ion source was reassembled after its cleaning procedure. A

light collimator was placed in front of the lamp and another was placed in front of the window of the ion source to determine the light axis. A beam limiter was then placed between these two collimators and the lamp was turned on. To determine if the light beam was focussed there, a screen was inserted at the beam limiter. Beam power was monitored by the large aperture pyroelectric detector and light power was adjusted to be less than 1 W on the interference filter. The filter monochromator was then placed in its position, and the light beam was focussed at the center of the target.

The Xe arc lamp was turned on at least 30 minutes before the experiment to avoid the slow drift of the light power which was associated with the change of the spectral intensity of the lamp. A slow light chopper was put into the light path and the large aperture pyroelectric detector monitored the total light power at the beam limiter and after the filter monochromator. Following the recheck of the alignment of optics by the pyroelectric detector, the light beam was focussed on the target. Then, the fast light chopper was tuned on and the constants of phase sensitive detection circuits were properly adjusted.

(5) Experimental Measurements

Several parameters had to be adjusted to realize the quasi-steady state operation of the ion source. The Cs oven power was adjusted until the H^- current, detected at the momentum analyzer, was constant. Then the hydrogen neutral pressure and the

arc current were readjusted to the pre-determined values. Confirming that H^- current was still nearly constant, the filter monochromator was scanned and the photoelectron current was recorded. The H^- current, the discharge current and the hydrogen neutral pressure were continually monitored to see if they were constant within the experimental error of 2%, during the measurement of the photoelectron current. Then signals from the momentun analyzer and the Langmuir probe were measured and recorded.

When the Cs oven power was increased to change the H^- current, the target ion saturation current sometimes became noisy and it was virtually impossible to measure the photoelectron current. This noise was usually irrelevant to the discharge current or the electron density of the plasma. When the source was operated at the constant H^- output current, or when the H^- current was decreased by reducing the oven power, the target ion saturation current was quieter and the noise at this time was proportional to the discharge current. The reason for the noise that we see when the Cs level was increased is suspected to be due to the inhomogeneous surface coverage of Cs that leads to the formation of arc spots at the surface of the target. To avoid this noise, the H^- current was kept higher for a while, and then slowly decreased to the desired value. When several different values of H^- current and the corresponding work functions had to be measured successively, the measurement was started from the condition for the higher H^- current production.

The time constant of the discharge condition could not be made much longer than 10 minutes, when Cs oven was turned on. Due to this time limit, the signal integration time for the photoelectron current was set a few seconds. The accuracy of the measurement was determined by this signal integration time, and by the plasma noise to the target that was proportional to the electron density. The work function could be determined in the 5×10^{10} cm^{-3} plasma, but the corresponding experimental error was more than ± 0.2 V.

(4-2) Data Analysis

All of the data were analyzed after each consecutive series of experiments. The photoelectron current output was recorded on the chart recorder. The ripple and the average of the phtotelectron current were determined from this trace. These two parameters for each photon energy were stored in the computer together with the monotired power of the incident monochromatic light. A minicomputer calculated the quantum efficiencies and plotted their square roots on CRT display. The work function was determined from this plot. Several points that were probably out of the range of Fowler's theory were discarded by the operator, controlling the cursor of the terminal. The value of the work function with the error range was displayed on the screen. When the range to determine the work function was not obvious on the screen, several combinations of the data points were used to determine the work function and its maximum error range. Typical output of the least square fit program that followed the treatment stated above is shown in Fig. 14.

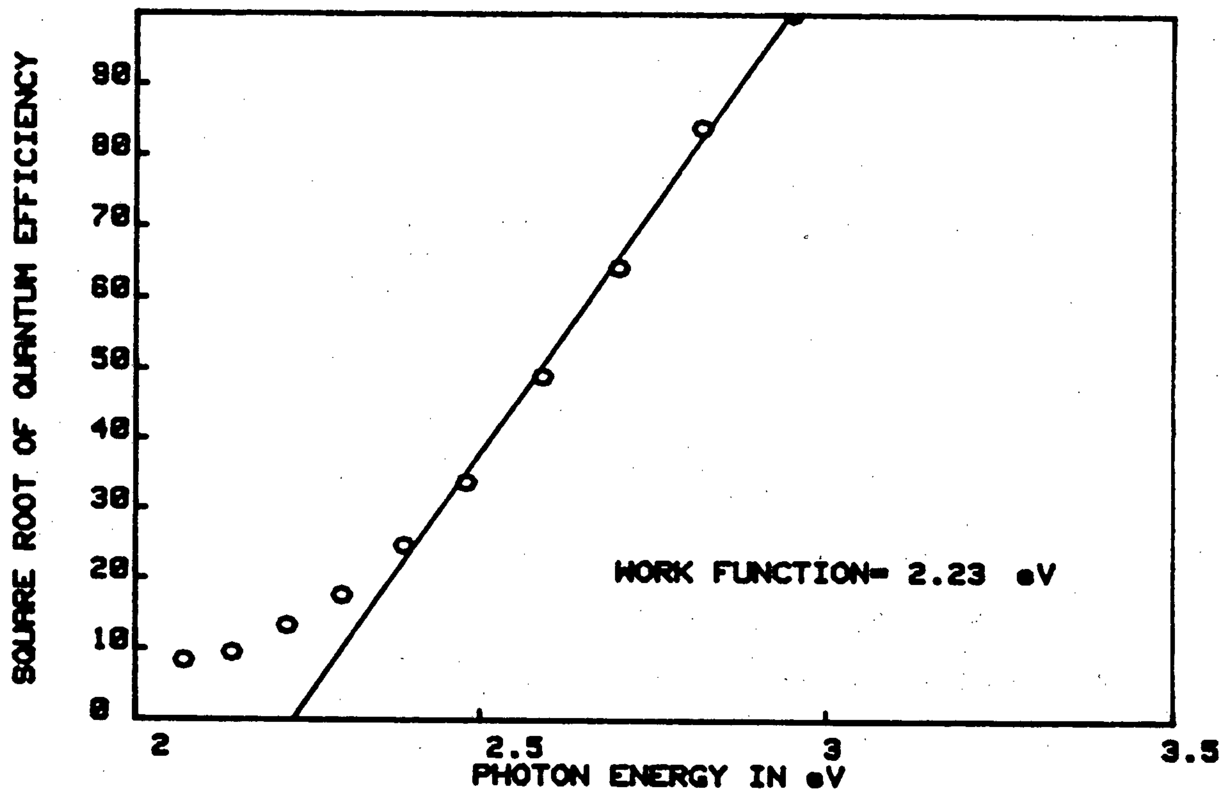

XBL 829-11508

Fig. 14

The differential momentum spectrum of the H^- beam was displayed soon after the sweep of the magnetic field of the analyzer. The energy spectrum and the total H^- current were calculated along the theory explained in Appendix 4, and displayed on the terminal. The hard copy of the spectrum as shown in Fig. 15, was recorded for each set of data. In Fig. 15, the energy distribution of H^- beam is plotted with respect to the reduced target energy. The 100% of the target potential corresponds to the actual target bias voltage, that is calculated along with the dispersion of the analyzer explained in Appendix 6. The neutral hydrogen pressure, the discharge current, the filament current, the wall temperature, the target current and other parameters were recorded along with the H^- current. Among these parameters, the neutral pressure and the discharge voltage and current were readjusted during the experiment, and only the target current changed appreciably. The total H^- current was usually divided by the target current to express the H^- production efficiency.

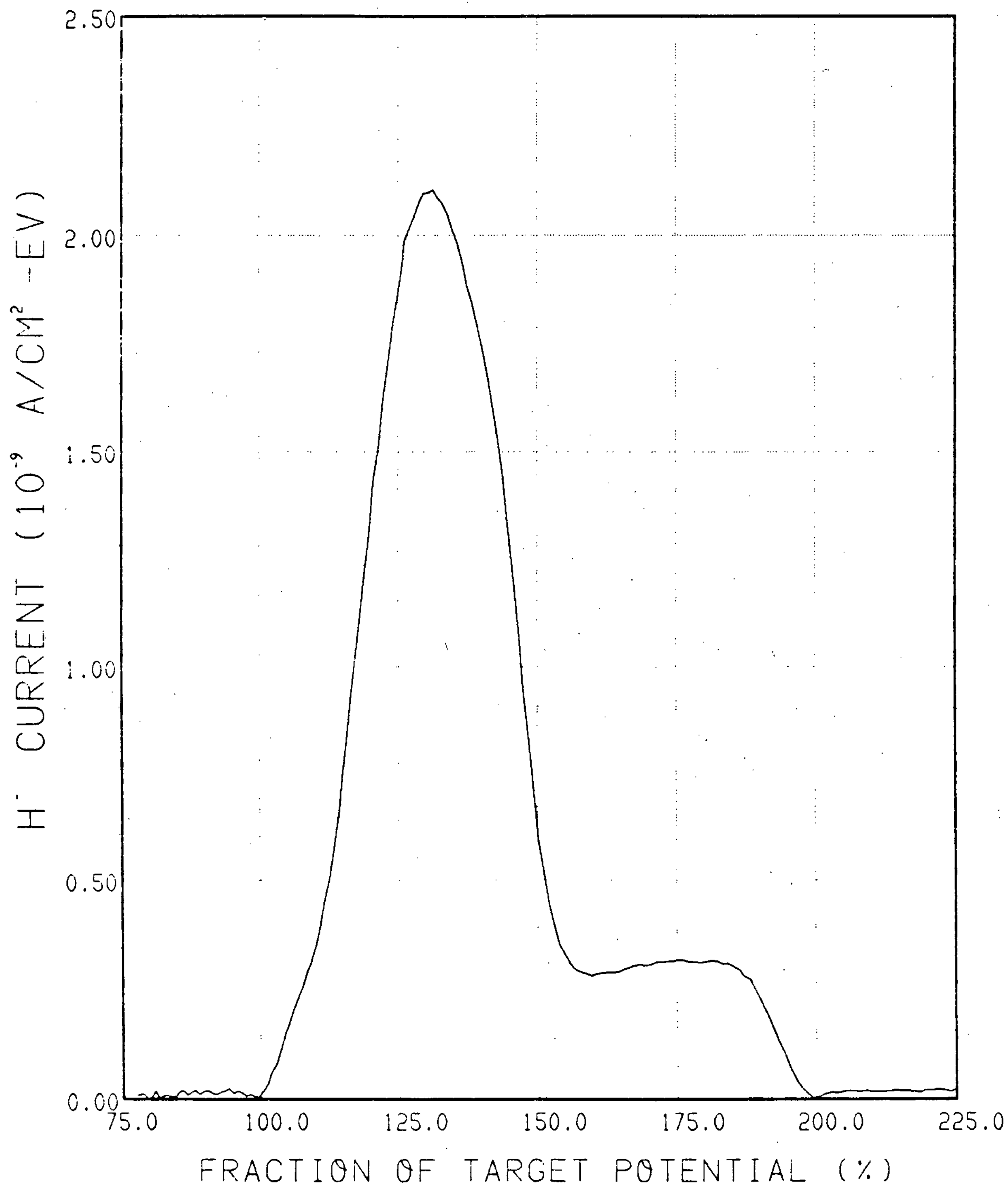

Fig. 15

CHAPTER 5

EXPERIMENTAL RESULTS AND DISCUSSION

(5-1) Correlation between Work Function and H^- Production

The correlation between the target work function and the surface produced H^- current was studied for both Mo and Cu targets. To maintain better signal-to-noise ratio, arc power was kept as low as 5 W, with an average electron density of 2×10^9 cm^{-3}. Figure 16 shows the result for Cu target. On the graph, the H^- ion current divided by the target ion saturation current was plotted against the measured value of work function. The hydrogen neutral pressure was kept at 1 mTorr and the target potential was 100 V.

Experimental error of the H^- current and the target current were within 5% and 3%, respectively. The statistical error of the work function was usually smaller than ± 0.03 eV. When the target work function was lower than 1.5 eV, the photoelectron emission was small in the energy range used to determine the work function, and the error was sometimes larger than ± 0.05 eV. The estimated systematic error due to the simplification of Fowler's analysis is -0.03 to -0.01, and total error of work function measurement was usually -0.06 to +0.02 eV.

After the experiment, the surface of the Cu target was found to be sputtered due to plasma particles bombardments. The inner surface of the quartz glass shield of the target was also found to be covered by a layer of the sputtered Cu. Though an obvious change

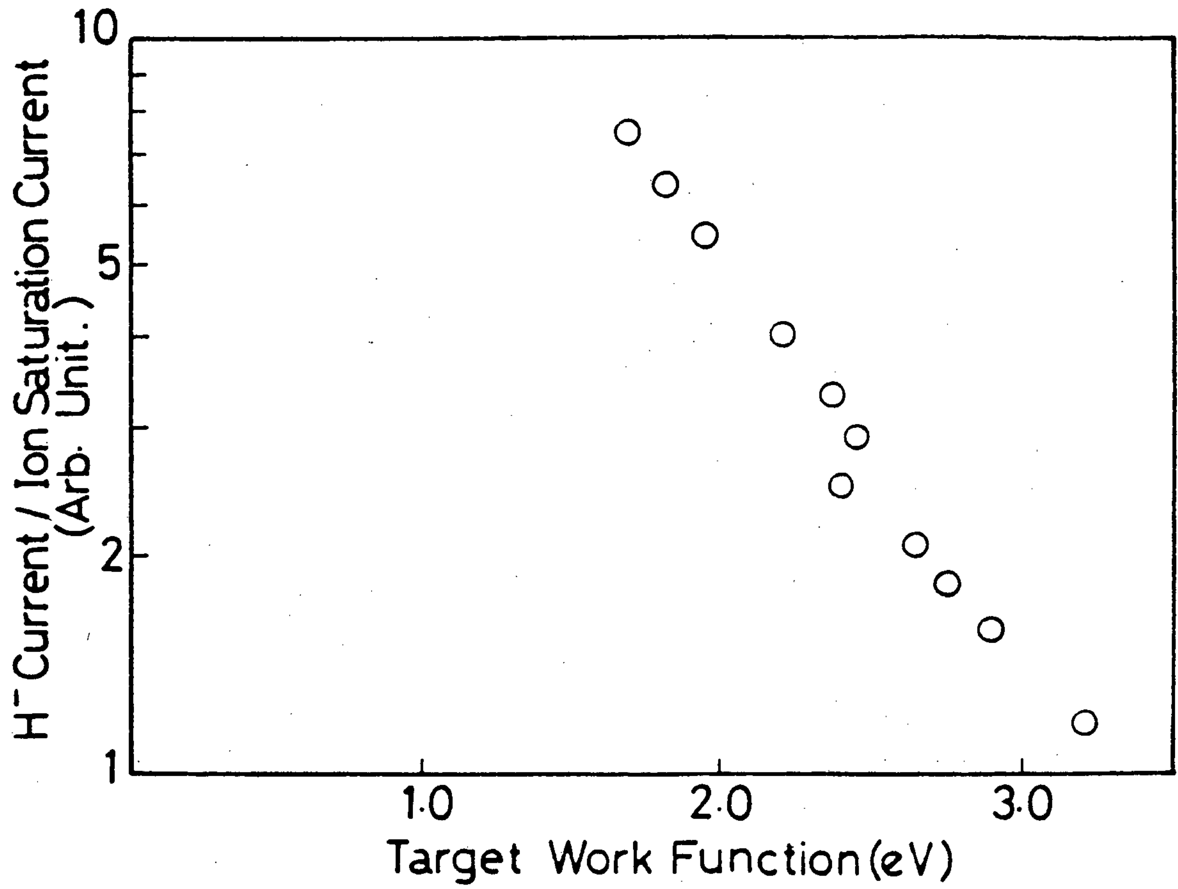

Fig. 16

of the surface area of the target was never observed, the target was changed to Mo, to avoid a possible change of experimental condition of the target by sputtering. In case of the Mo target, build up of the metal layer on the surface of the quartz glass sheath was small, and this enabled us to study the correlation between work function and H^- yield at the higher target bias voltage. Results of the Mo target are plotted in Fig. 17. As with the Cu target result, the H^- current monotonically increases for decreasing work function.

For all three biases of 100, 200, and 300 V, the Cs density was increased up to the optimum condition to give the largest H^- currents. Therefore, the lowest work functions appearing on the graph are the observed lowest work functions at the corresponding target bias. In the cesiated hydrogen discharge the work function minimum was usually less than 1.4 eV which was less than minimum work functions of Cs covered Mo,[21] or Cs covered Cu.[22] There are several possible explanations for this low value of work function. The first possibility is the additional co-adsorption of hydrogen on the Cs covered surface. Papageogopolous and Chen[23] have reported that co-adsorption of hydrogen onto a Cs covered tungsten surface decrease the work function minimum. In the present system, hydrogen coverage of the target in the discharge may be thicker than that for neutral hydrogen. This thicker layer of adsorbed hydrogen may reduce the minimum work function. Further discussion on this point is given in Appendix 7. The second possibility is the

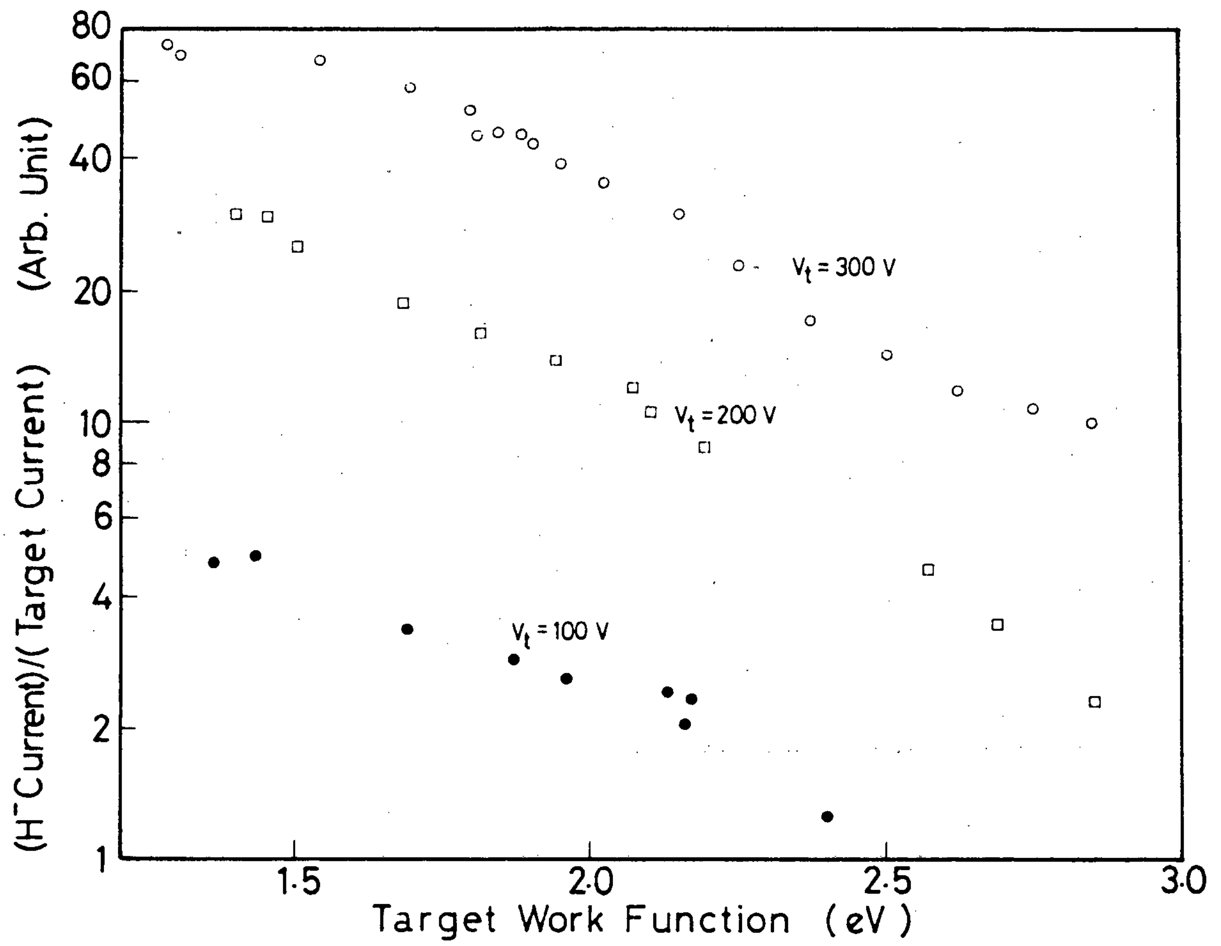

Fig. 17

contamination of the surface by impurities. For example, the small oxygen concentration below the Cs layer is known to reduce the work function minimum.[24]

At the same work function and target bias, the reproducibility of the absolute value of the H^- current was poor, and became even poorer as the target bias was increased. When work functions of two successive experiments were compared, H^- was always larger for the smaller work function. But when the two H^- currents at similar work functions, measured at different times, were compared, the H^- current was sometimes larger at the slightly higher target work function. Thus, H^- current appeared to be affected by the history of the ion source operation, and usually, H^- current at the same target work function was recorded to be higher after the operation of the source with higher Cs concentration. When the discharge condition was kept constant and Cs density was increased and then decreased to recover the same H^- current, a slight decrease of electron temperature and a small increase of electron density were observed on the Langmuir probe signal. The observed change of H^- current may be caused by this change of the discharge condition, but the reason for this change of the discharge is not known at this time.

(5-2) Effect of Target Bias on the H^- Production

According to the results in Fig. 17, the H^- yield monotnically increases with the target bias potential for fixed target work function. In their 1977 Brookhaven paper[11], the Novosibirsk group

reported the ratio of the H^- current to the positive ion current detected through a small aperture in the cathode of a cesium loaded Penning source. They found that the H^- production efficiency strongly decreased with increasing discharge potential. More recently, Ehlers and Leung[25] measured the H^- produced from a metal surface in a cesiated hydrogen discharge, and reported that they observed the existence of optimum bias voltage for H^- production of around -200 V. A very similar result was found for our source.

After an introduction of enough Cs to the ion source to sustain the Cs recycling from the source chamber wall, a cesiated hydrogen discharge with a time contant of several hours was established. Soon after the increase of the target potential, H^- first increased, and then decayed to a steady state value which was a function of the target bias. Figure 18 shows one example of this source characteristic. However, the optimum target bias was found to be different when Cs concentration in the source was changed. It was suspected that the Cs coverage on the surface became smaller as the target bias potential was raised, because of the possible sputtering of adsorbed Cs by the plasma ions.

The effect of bias voltage on work function was studied by utilizing a very stable cesiated hydrogen discharge. For various bias potentials, the target work function was measured. Figure 19 shows the result of this measurement. It is clearly seen that the work function of the target was changed by the target bias. The

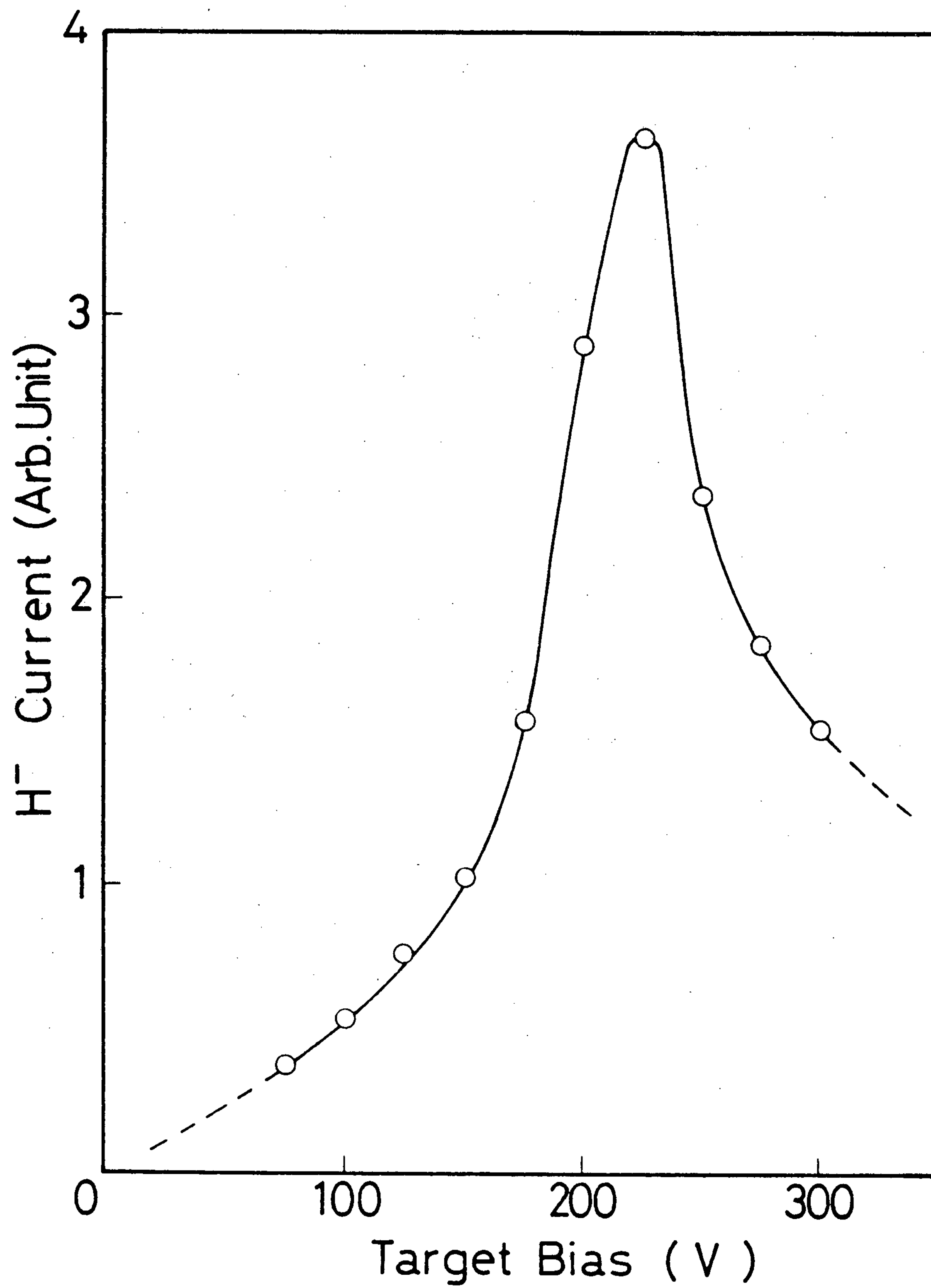

XBL 832-8208

Fig. 18

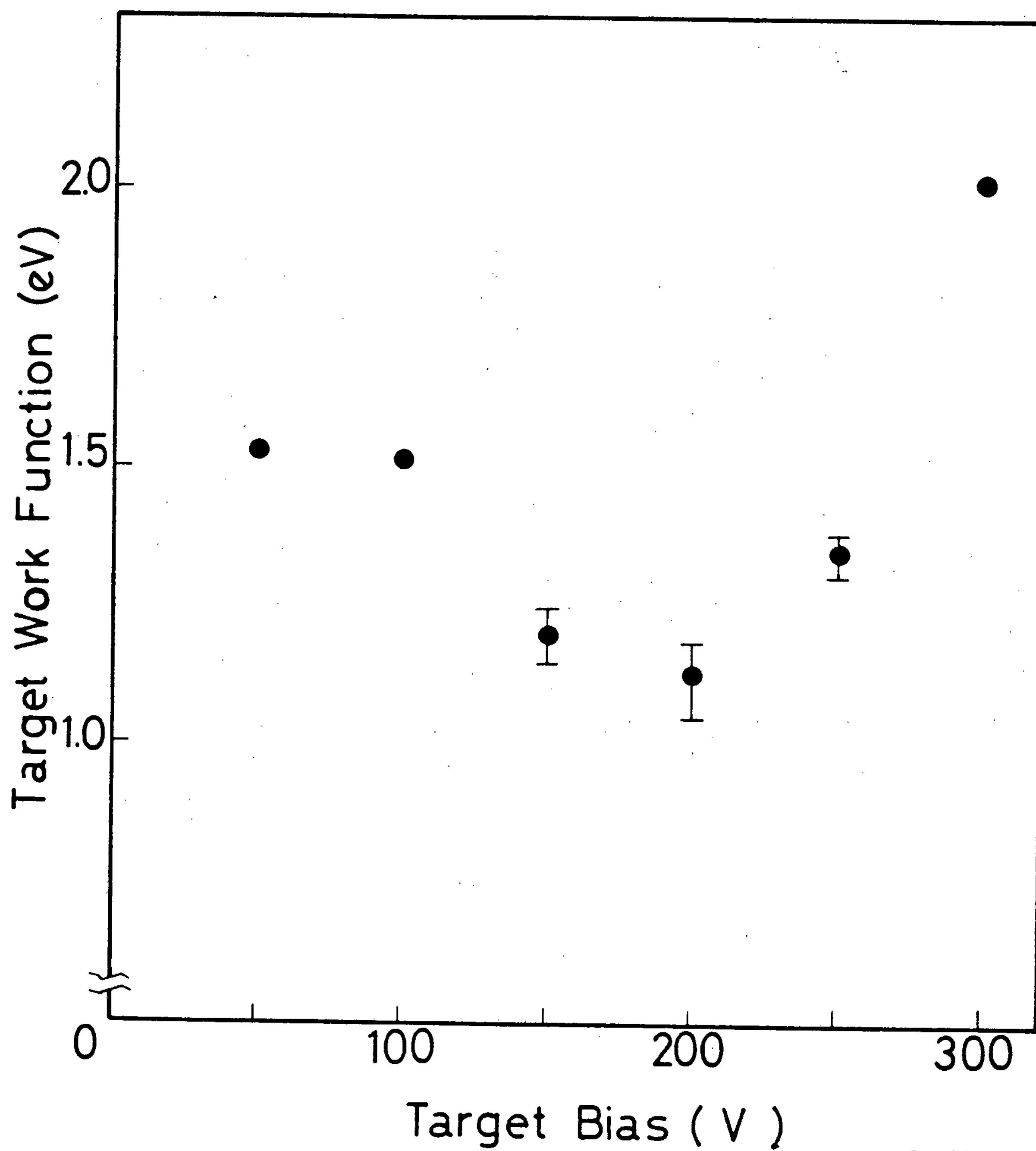

Fig. 19

work function of the target was higher at both higher and lower target bias, and was the lowest at the bias potential of 200 V. The Cs coverage on the target decreased with increasing bias. Starting at a thick coverage for low bias, the Cs coverage decreased through that corresponding to the work function minimum at 200 V and then continued to decrease yielding a higher work function. Incidentally, the maximum value of H^- current was recorded at the target potential of 200 V. This result clearly demonstrates that the optimum condition for the H^- production should not be determined solely by the bias potential, but by the combination of the surface condition and the bias potential.

Since the experimental geometry of Ehlers and Leung was almost the same as ours, their result, the H^- dependence on the bias to the H^- production surface, can be attributed to the change of work function due to the sputtering effect as we observed in our experiment. The geometry of the experiment by the Novosibirsk group was very different from ours, but considering their higher power loading to the production surface, their result is explainable with the higher target work function leading to lower H^- production at a higher bias voltage.

The removal of Cs by a discharge was also confirmed to be enhanced by the increase of the electron density. In our source, work function minimum was obtained until the density of 6×10^9 cm^{-3} at 300 V, but due to plasma noise, a work function measurement was not accurate enough. To confirm the attainment of the work function minimum at the H^- production surface in a denser

plasma, another modification should be made to the experimental method. One possible way to measure the work function for high density discharge was tested and explained in Appendix 9.

(5-3) H^- Spectra at different Work Functions

Before the introduction of Cs into the discharge, the work functions of the targets were at least 4.14 eV, since no photoelectron current was observed at this photon energy. Under this condition, the energy spectrum of H^- was relatively broad. An example of this kind of spectrum can be seen in Fig, 20. This trace was taken from the Cu target biased at 350 V in a pure hydrogen discharge with 300 W of an arc power. The spectrum appears to be composed of three groups of particles, as is shown on the figure with dashed lines. One group has the high energy cut off at twice the target bias potential. The second and third groups have their high energy cutoffs at 1.5 and 1.33 times the target potential, respectively. These are consdiered to be the H^- current created by the back scattering of H^+, H_2^+, and H_3^+ accelerated across the sheath. The reduction of discharge power did not change this picture except in the contribution from protons, whose current density decreased with the reduction of an arc power.

When Cs was introduced into the discharge, several distinct changes of the spectrum were observed. The amount of H^- ion current increased rapidly, and the peak of the energy spectrum shifted toward the low energy side. Then, as work function became

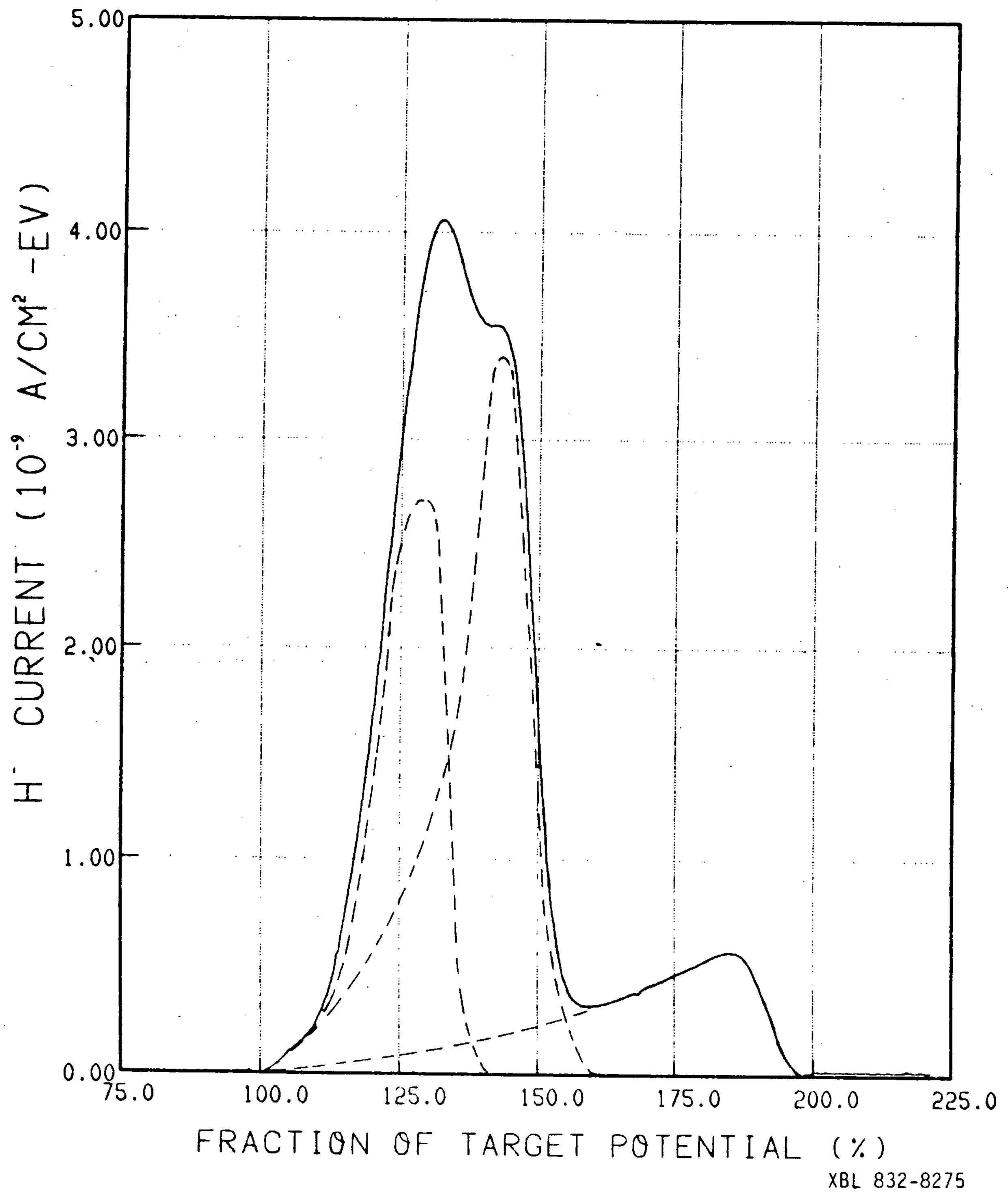

Fig. 20

lower than about 3 eV, another H^- component appeared on the energy spectrum near the target potential. As the work function decreased, this low energy component of H^- increased much more rapidly than the H^- of the back scattering component. These changes of the H^- energy spectrum by the reduction of the work functions are shown in Fig. 21 for the case of 200 V target bias. Similar results were observed for 100 and 300 V target bias. The target work function was close to its minimum, and most of the H^- current belonged to a low energy component whose height increases with the target bias potential. Figure 22 compares the H^- spectra at three different bias potentials at nearly the same work function of the target. From the fact that the peak height of this low energy H^- current was increased by the target bias, most of the H^- in this group seemed to be produced by kinetic desorption by charged particles, rather than by back scatterings of atomic hydrogen.

(5-4) H^- Produced at the Thick Cs Sufrace

Several interesting phenomena were observed when the ion source was operated with a large amount of Cs. To make a thick Cs coverage without putting too much Cs into the discharge, target bias was maintained at 100 V. As work function increased together with Cs concentration, H^- current decreased rapidly. This is shown in Fig. 23, and the corresponding H^- spectra are compared in Fig. 24. The most obvious effects was that the H^- current in the

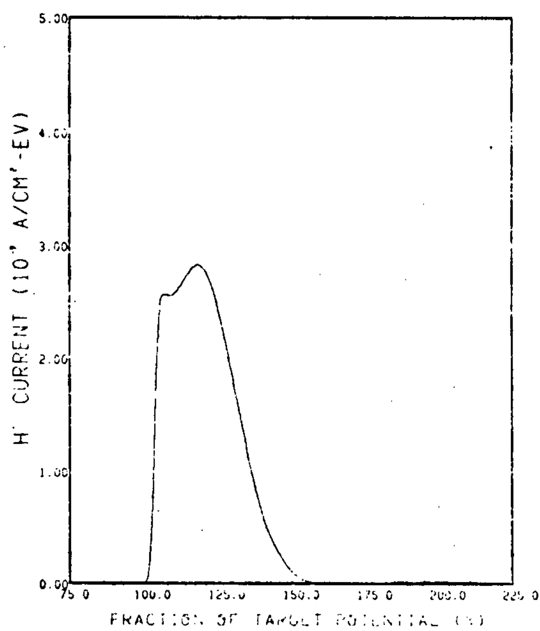

(a)

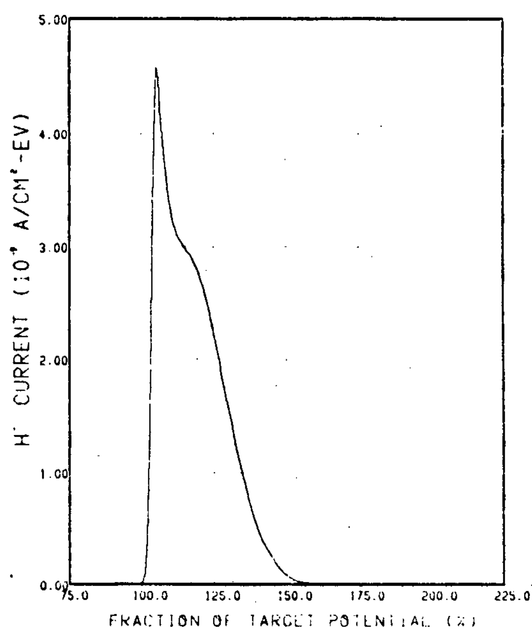

(b)

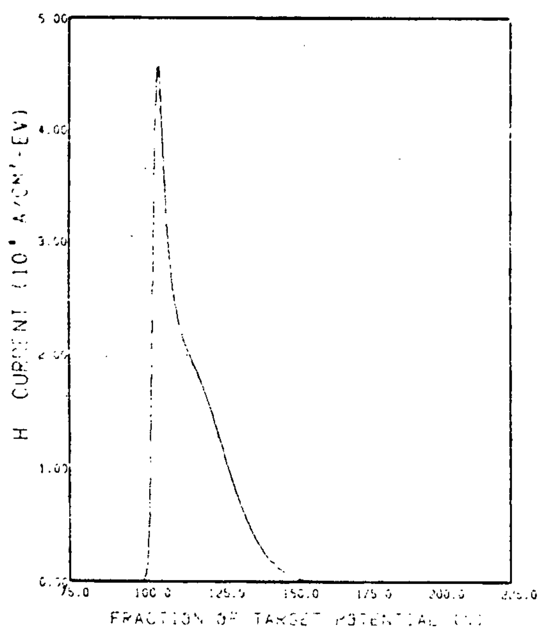

(c)

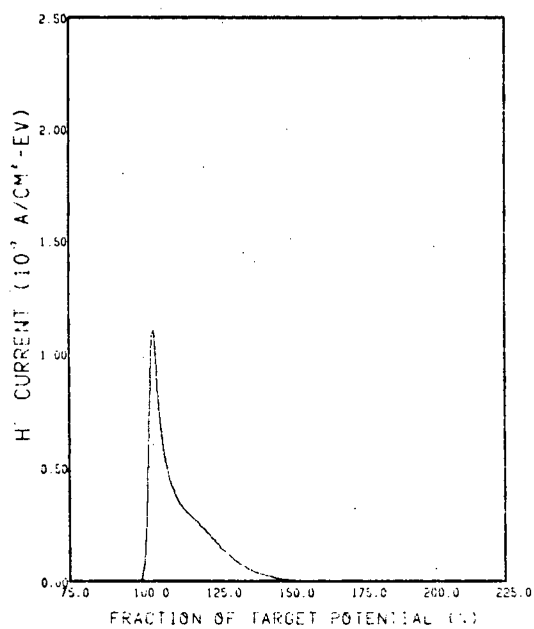

(d)

XBL 832-8270

Fig. 21

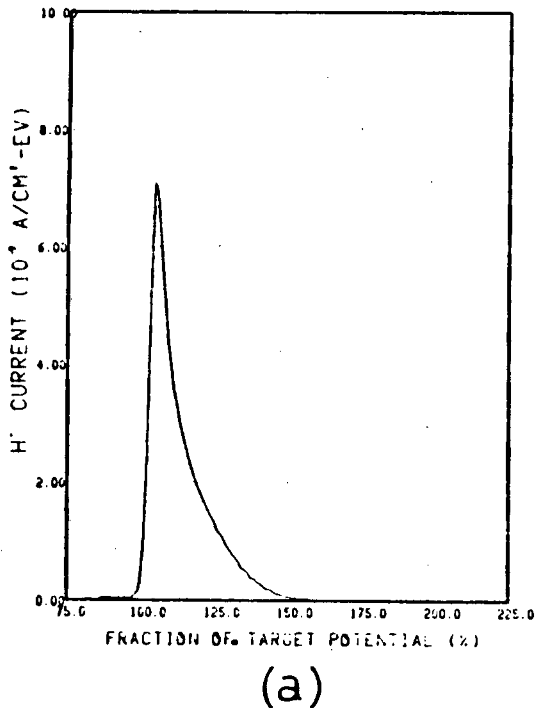

(a)

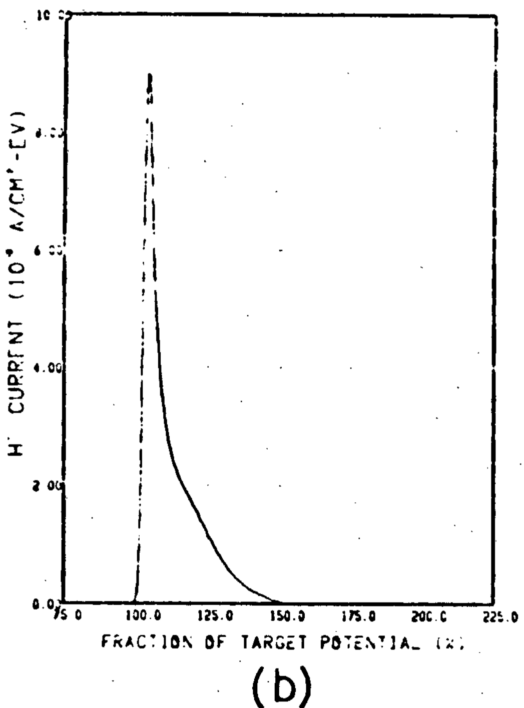

(b)

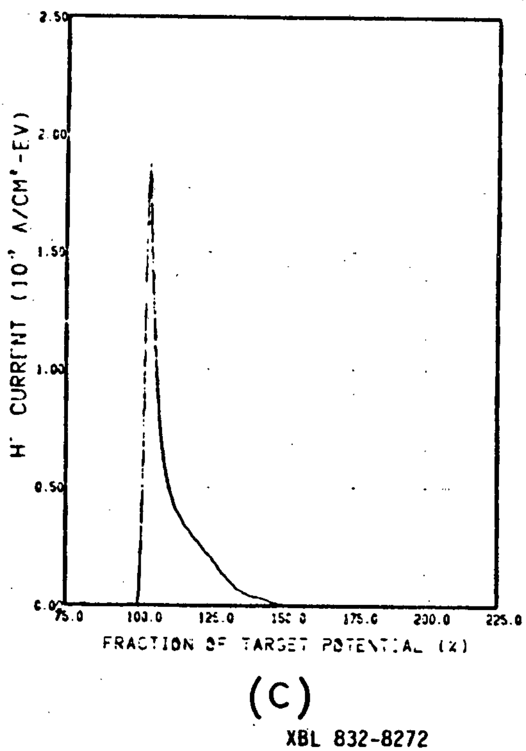

(c)

XBL 832-8272

Fig. 22

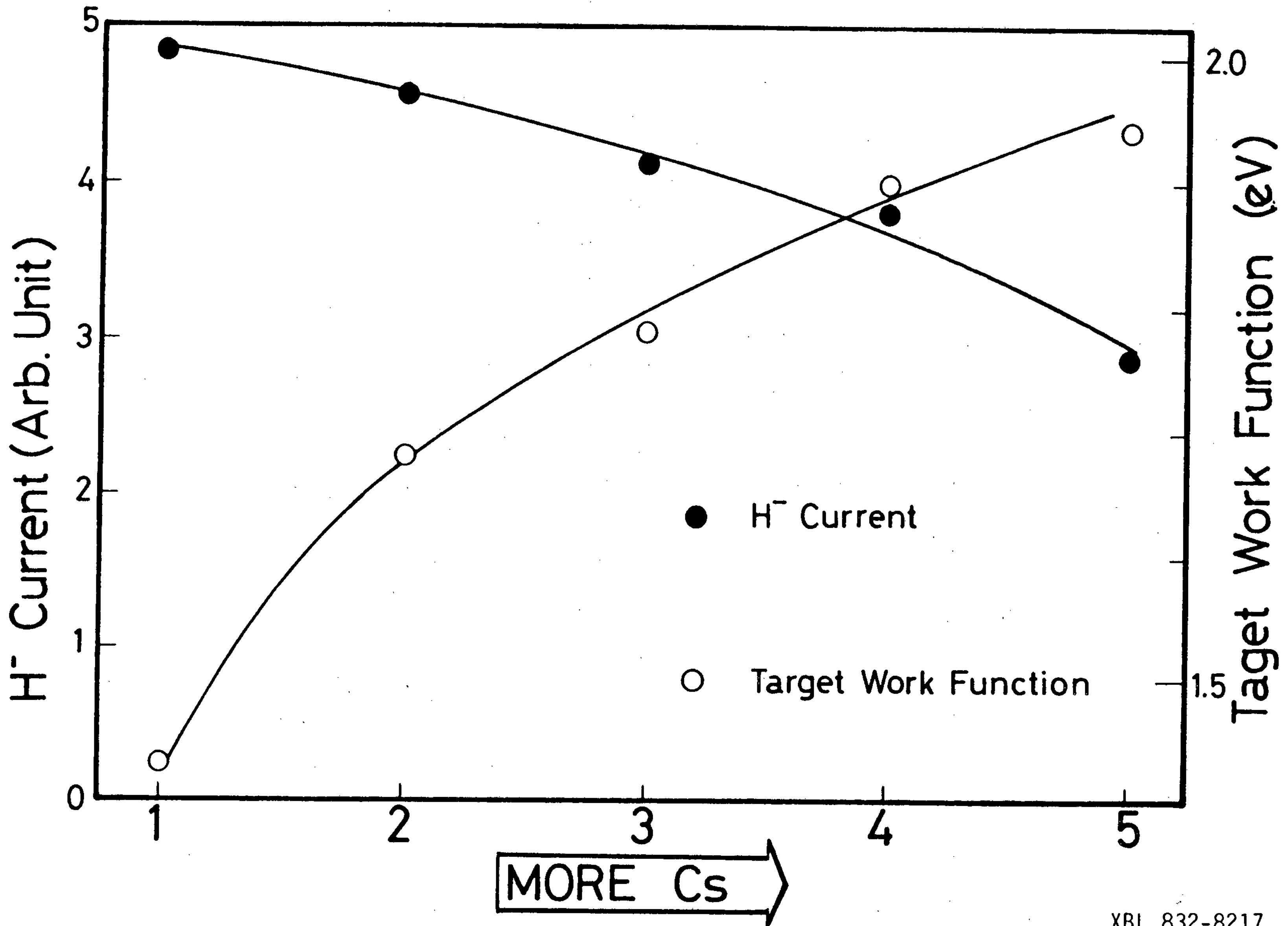

XBL 832-8217

Fig. 23

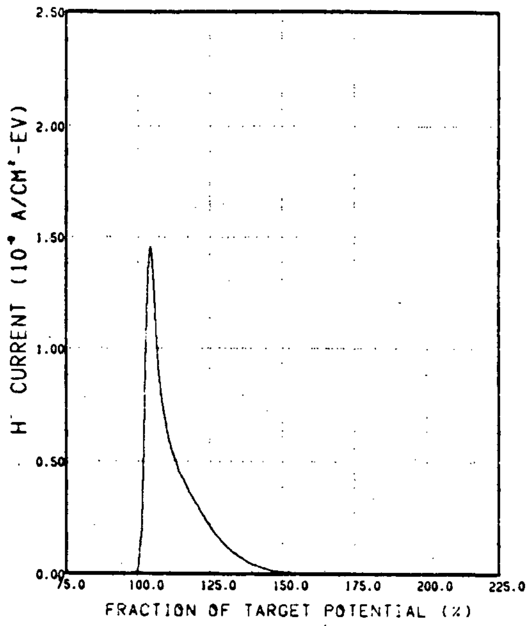

(a)

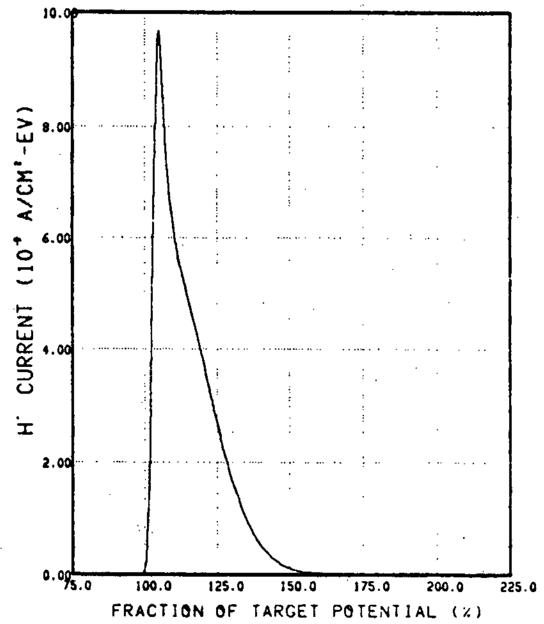

(b)

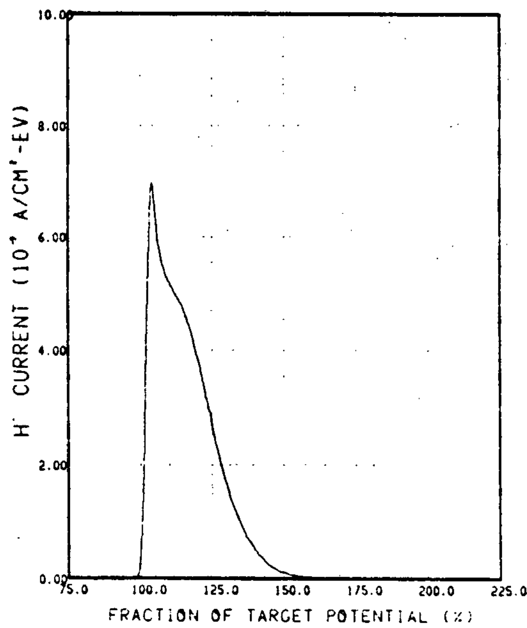

(c)

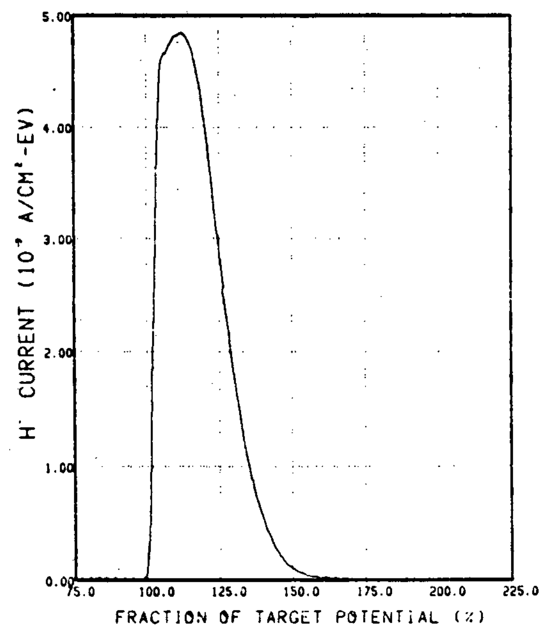

(d)

XBL 832-8271

Fig. 24

energy range where the back scattering was supposedly dominant, increased as the work function increased. On the other hand, H^- current in the low energy range decreased for increased work function of the target. In the experiment by Schneider[9], H^- production efficiency by back scattering process was reported to be the maximum at the Cs coverage slightly thicker than that of the work function minimum. He explained that this was because of the increase of the particle reflection coefficient due to thicker Cs coverage, which compensated the decrease of production probably due to the increase of the work function. Our result looks consistent with this explanation.

Another noticeable feature of the H^- at thicker coverages of Cs was the low height of the low energy H^- peak. When the H^- energy spectra were compared at two different Cs coverages with the identical discharge condition, target bias and work function, the peak height was always larger for the thinner coverage of Cs. The adsorption of hydrogen on the Cs covered surface in the cesiated hydrogen discharge is not well known at this point, but the sticking coefficient of H on Cs covered W surface has been reported to decrease exponentially with increasing Cs coverage.[23] If the number of H atoms adsorbed on the surface is smaller at the thicker Cs coverage, even with the presence of the hydrogen discharge, the decrease of the H^- peak at the thicker coverage of Cs can be ascribed to the reduction of target H atom adsorbed on the surface.

(5-5) Upper Limit of the H^- Production Probability

A rough estimation of the upper limit of the H^- production efficiency can be obtained by measuring the apparent target ion saturation current. The measured value of the target current is the true ion saturation current plus the secondary emission currents of negative charged particles. When Cs was introduced into the discharge, the sum of the impurity negative ion currents produced at the surface was usually less than 10% of the total negative ion current. If we neglect the effect of ion secondary electrons, and impurity negative ions, the target current becomes ion saturation current plus surface produced H^- current. Then, the target current should increase with the H^- current as the work function decreases. Figure 25 compares the theoretical value of the ion saturation current to the measured value of the target current. As the work function decreased, the target current increased while the ion saturation current derived from the electron density and electron temperature obtained from the probe was relatively constant. It can be seen from Fig. 25 that target current approaches a constant value at high target work function. If we assume that this value of target current is close to the ion saturation current, we can compare this current with the maximum target current to estimate the maximum H^- yield at the target.

When the ion source is operated by Cs recycling from the wall, Cs coverage on the target can be changed by controlling the bias potential. By raising the target potential from the one which gives the thick Cs coverage, the H^- current increases as the coverage

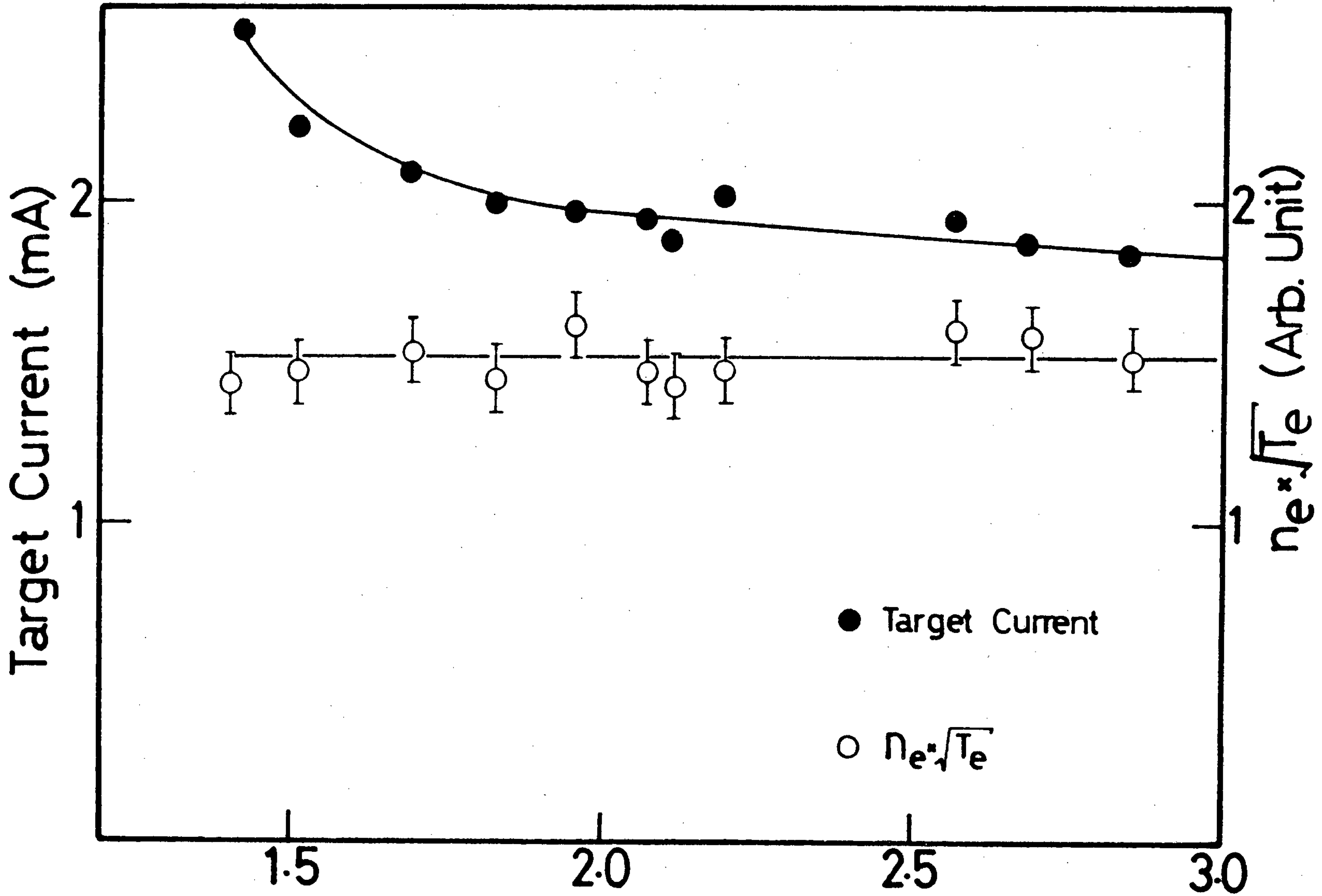

XBL 832-8215

Fig. 25

approaches to the work function minimum, and then decreases in accordance as the Cs is removed from the surface. If the bias potential is high enough, the Cs coverage will be sufficiently removed to give the target current with little contribution from H^-. When the target potential is decreased from this condition, Cs will be accumulated on the surface and the H^- reaches its maximum sometime after the reduction of the target bias. This method of changing Cs coverage was ideal for measuring the target current at the work function minimum and at the high work function, because the Cs density in the plasma should be nearly constant for two conditions. The typical time history of the photoelectron emission current from the unfiltered light and the H^- yield after the removal of Cs from the target, is shown in Fig. 26.

The ratio of the maximum target current to the minimum target current was approximately 1.8 at 400 V decreasing to about 1.6 at 100 V of the target bias. As shown on Appendix 8, there exists an upper limit for H^- production probability which is caused by the space charge effect. The above values for maximum H^- production probability of 80% and 60% correspond to approximately 30% and 20% for H_3^+ dominant plasma, which are obviously small for the space charge limit condition to exist.

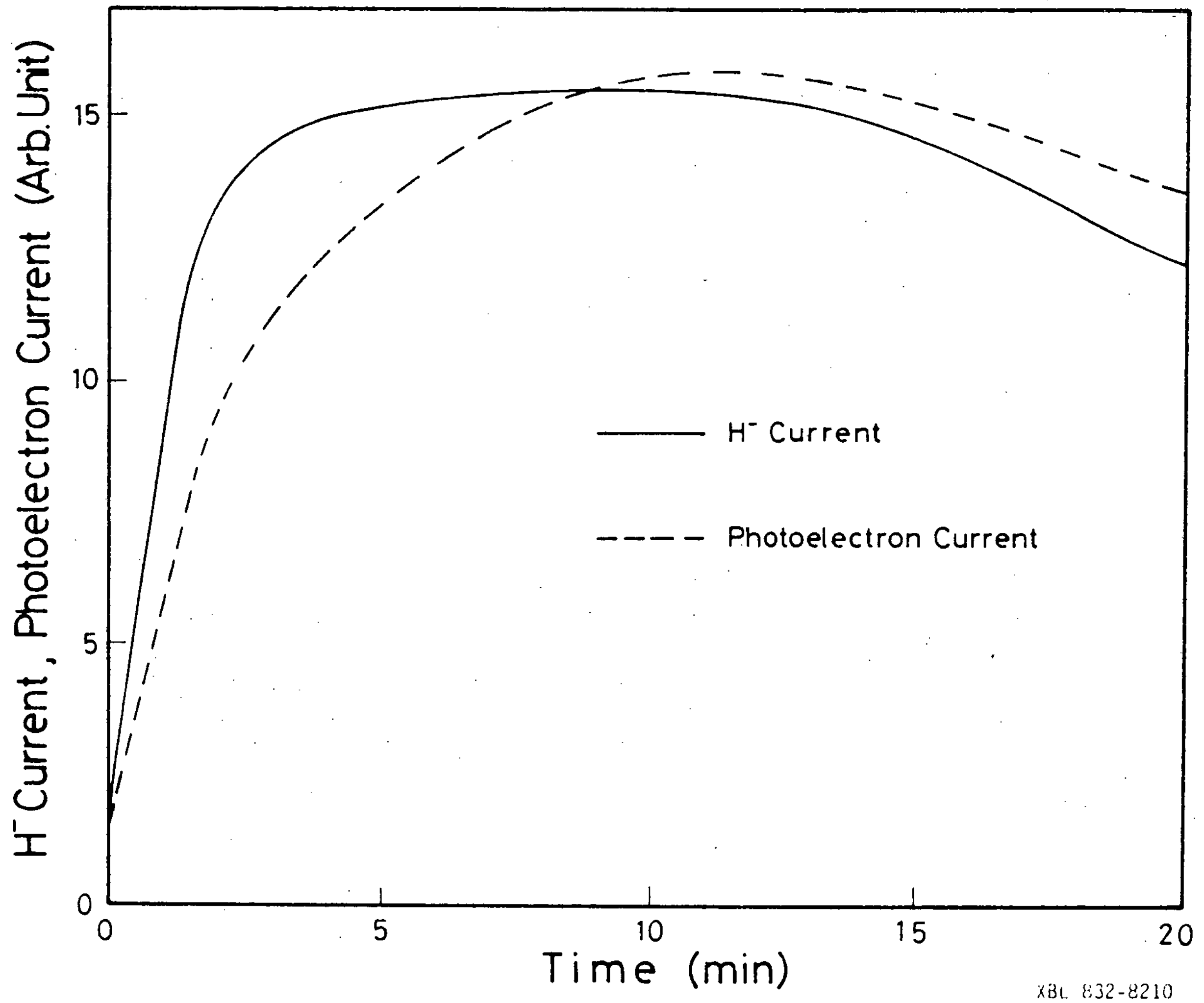

Fig. 26

CHAPTER 6

CONCLUSIONS

The work function of the metal surface immersed in the plasma was determined by measuring photoelectron emission currents. The main problem for the experimental technique was the plasma noise on the photoelectron current signal. To keep reasonable accuracy for the measurements, most of the experiments were done with plasmas of electron density less than 5×10^{9} cm^{-3}. This plasma density generated enough H^- current to study the basic behavior of the surface produced H^- beam.

The total H^- current which was detemined by integration of the output of the momentum analyzer showed a monotonic increase for a decreasing work function. The absolute value of H^- current at the fixed work function and fixed discharge power was not very reproducible, and this was possibly attributed to the change of the discharge characteristics, in particular, the behavior of Cs. The increase of the target bias always made the Cs coverage of the target thinner. This caused the apparent optimum target bias for a steady state operation of the ion source with a specific Cs concentration. By increasing the amount of Cs in the discharge, coverage could be adjusted to the one corresponding to the work function minimum, up to a target potential of 300 V. For similar values of work functions of the target, the total H^- current appeared to be monotonically increasing as the target bias was increased.

The energy spectrum of H^- current showed that the enhancement of the H^- production probability was especially pronounced at the lower H^- energies. It was observed the the component of H^- with energy close to the target bias was dominant near the work function minimum. The production probability of this group appeared to be governed by the work function, while the back scattering component seemed to be affected by the particle reflection coefficient of the surface. The production probability of this low energy group was higher for a higher bias potential, when compared to that at lower bias with similar work functions. This result indicates that one of the main sources of atomic hydrogen flux that creates the low energy H^- should be dependent on the target potential, and thus, the back scattering of the atomic hydrogen from the plasma was not the only major source of the H^- flux.

More careful studies are necessary to understand the physics of a surface-plasma ion source. To develop a model describing this type of ion source, the following points need further investigations:

(1) Surface density of atomic hydrogen on Cs covered metal surface at the known work function.

(2) Sputtering coefficients of Cs by hydrogen and Cs ions.

(3) Cross sections for surface collisions for H atoms on a surface.

In addition to the above points, similar experiments to ours should be done at a higher plasma density to confirm that the stated results are also valid for plasma parameters of actual ion sources.

REFERENCES

1. K. H. Berkner, R. V. Pyle and J. W. Stearns, Nucl. Fusion, 15, (1975), 249.

2. K. N. Leung and K. W. Ehlers, Rev. Sci. Instrum. 53, (6), (1982), 803.

3. K. W. Ehlers and K. N. Leung, Rev. Sci. Instrum. 51, (6), (1982), 721.

4. Yu. I. Belchenko, G. I. Dimov, V. G. Dudnikov, Investiya of USSR Academy of Science. Fiz. 37, (1973), 2573 .

5. R. K. Janev, Surf. Sci., 45, (1974), 609 .

6. M. Ye. Kishinevskiy, Institute of Nuclear Physics (Novosibirsk) Report IYAF 76-18 (1976).

7. J. R. Hiskes and A. Karo, "Proceedings of the First Symposium on the Production and Neutralization of Negative Hydrogen Ions and Beams," Brookhaven, NY., (1977), 42 .

8. B. Rasser, J. N. Van Wunnik and J. Los, Surf. Sci., 118, (1982), 697.

9. P. J. Schneider, LBL-10616, Ph.D. Thesis, Lawrence Berkeley Laboratory, University of California, Berkeley, CA.

10. M. L. Yu, "Proceedings of the First Symposium on the Production and Neutralization of Negative Hydrogen Ions and Beams." Brookhaven, N.Y., (1977), 48.

11. Yu. I. Belchenko, G. I. Dimov and V. G. Dudnikov, "Proceedings of the First Symposium on the Production and Neutralization of Negative Hydrogen Ions and Beams." Brookhaven, N.Y., (1977), 79.

12. O. S. Oen and M. T. Robinson, Journ. of Nucl. Materials, 76, 77, (1978), 370.

13. J. R. Hiskes and P. J. Schneider, Phys. Rev. B23, (1981), 949, "Symposium on the Production and Neutralization of Negative Hydrogen Ions and Beams." Brookhaven, N.Y., (1977), 15.

14. W. G. Graham, Phys, Let., 73A, (1979), 186.

15. K. Wiesenmann, "Proceedings of the First Symposium on the Production and Neutralization of Negative Hydrogen Ions and Beams." Brookhaven, N.Y., (1977), 97.

16. M. Prutton, "Surface Physics," Clarendon Press, Oxford, (1975), 94.

17. J. R. Hiskes, A. M. Karo and M. A. Gardner, J. Appl. Phys., 47, (1976), 3888.

18. R. K. Janev and S. B. Vojvodic, J. Phys, B., 13, (1980), 2481.

19. J. R. Hiskes, J. de Physique, Tome 40, Colloque C-7, Suppl. 7, Vol. II, C7-479, July, (1979).

20. R. Limpaecher and K. R. Mackenzie, Rev. Sci. Instrum., 44, (1973), 726.

21. L. W. Swanson and R. W. Strayer, J. Chem. Phys., 48, (1968), 2421.

22. R. G. Wilson, J. Appl. Phys., 37, (1966), 3151.

23. C. A. Papageorgopoulus and J. M. Chen, Surf. Sci., 39, (1973), 283.

24. J. L. Desplat and C. A. Papageorgopoulus, Surf. Sci., 92, (1980), 97.

25. K. N. Leung and K. W. Ehlers. "Proceedings of the Second Symposium on the Production and Neutralization of Negative Hydrogen Ions and Beams." Brookhaven, N.Y., (1980), P. 65.

26. T. E. Fischer, J. Vac. Sci. Tech., Vol. 9, No. 2, (1972), 860.

27. R. H. Fowler, Phys. Rev., 38, (1931), 45.

28. L. A. DuBridge and W. W. Roehr, Phys. Rev., 39, (1932), 99.

29. C. N. Berglund and W. E. Spicer, Phys. Rev., 136, (1936), A1030.

30. P. A. Anderson, Phys. Rev., 47, (1935), 958.

31. C. Herring and M. H. Nichols, Rev. Mod. Phys., 21, (1949), 185.

32. R. J. Zollweg, Surf. Sci., 2, (1964), 409.

33. B. J. Hopkins and B. J. Smith, J. Appl. Phys., 39, (1968), 213.

34. S. T. Martin, Phys. Rev., 56, (1939), 947.

35. F. F. Chen. "Plasma Diagnostic Technique." Chap. 4. R. H. Huddlestone, S. L. Leonard, editor. Academic Press, N.Y., (1965).

36. I. Langmuir and H. M. Mott-Smith, Gen. Elec. Rev., 27, (1924), 449.

37. W. G. Cross, Rev. Sci. Instrum., 22, 10, (1951), 717.

38. O. Klemperer, "Electron Optics," Cambridge, UP London, (1971).

39. R. W. Motley, "Q machines." Chapter 2. Academic Press, N.Y., (1975).

40. A. Kh. Ayukhamov and E. Turmashev, Sov. Phys. Tech. Phys., 22, 10, (1977), 1289.

41. Ye. D. Bender, M. Ye. Kishinevskiy and I. I. Morozov, "Proceedings of the First Symposium on Formation and Neutralization of Negative Hydrogen Ions and Beams." Brookhaven, N.Y., (1977), P. 60.

42. Ye. D. Bender, G. I. Dimov and M. Ye, Kishinevskiy, Report IYAF, 75-9, Nuclear Physics Institute, U.S.S.R. Novosibirsk, (1975).

43. Handbook of Chemistry and Physics, 57th ed., R. C. West, editor, (1976).

44. L. D. Schmidt and R. Gomer, J. Chem. Phys., 43, (1965), 95.

45. G. D. Hobbs and J. A. Wesson, Plasma Phys., 9, (1967), 85.

46. D. Bohm, "The Characteristics of Electrical Discharges in Magnetic Fields," Chap. 3, A. Guthrie and R. K. Wakerling, editors, McGraw-Hill, N.Y., (1949).

Appendix 1

Fowler's theory of photoelectron emission.

Photoelectron emission from a metal surface is a three stage process: first, an electron is excited by absorbing a photon; second, the electron is transported to the surface; and third, it escapes from the metal. When the energy of the incident photon is low, or close to the work function, the photon excites only those electrons near the surface. In this case, the electron transport inside of the metal does not affect the quantum efficiency, which is defined as the number of emitted electrons devided by the number of absorbed photons. If we neglect the change of the absorptivity of the metal for different photon energies, the quantum efficiency is proportional to the metal electrons whose momentum component normal to the surface will be large enough to overcome the work function after absorbing the photon energy. When the conduction band electrons follow the Fermi-Dirac distribution, the number density of these electrons is given by the following integral equation.

$$n = 2\left(\frac{m}{h}\right)^3 \int_{\frac{1}{2}mV_z^2 = U_o - h\nu}^{\infty} dV_z \int_0^{\infty} dV_r \int_0^{2\pi} d\theta \, \frac{V_r}{1 + \exp([\frac{m}{2}(V_r^2 + V_z^2) - E_f]/kT)} \qquad \text{(A-1)}$$

where, m; electron mass

E_f; electrochemical potential

V_r; electron velocity component parallel to the surface

V_z; electron velocity component normal to the surface

$h\nu$; photon energy

U_o; Potential step at the boundary.

The integral can be written, following R.H.Fowler[27],

$$n = \frac{2\sqrt{2}}{h^3} \frac{k^2T^2}{(U_o - h\nu)^{1/2}} \int_0^\infty dy \frac{\log\left[1 + \exp\left(-y + (h\nu - \phi_w)/KT\right)\right]}{\left(y + (U_o - h\nu)/kT\right)^{1/2}} \quad \text{(A-2)}$$

In the limit that $h\nu = \phi_w$, and $E_f >> kT$, the equation can be approximated by,

$$Y \propto \frac{1}{(U_o - h\nu)^{1/2}} \int_0^\infty dy \log\left[1 + \exp\left(-y + (h\nu - \phi_w)/kT\right)\right] \quad \text{(A-3)}$$

By expanding the logarithm and integrating term by term with the limit of $T > 0$, we have,

$$Y \propto \frac{(h\nu - \phi_w{}^2)}{(U_o - h\nu)^{1/2}}, \qquad h\nu > \phi_w \quad \text{(A-4)}$$
$$Y = 0 \qquad h\nu < \phi_w$$

Therefore, when the square root of the quantum efficiency is plotted as a function of the photon energy, the work function is the intersect of a straight line. To minimize the error from finite T, $(h\nu - \phi_w)$, and E_f, Fowler determined the work function by defining the function $\Phi(\mu)$ such that,

$$\log \frac{Y}{T^2} = B + \Phi(\mu)$$
$$\mu = \frac{h\nu - \phi w}{kT} \qquad \text{(A-5)}$$

where B is a constant. $\Phi(\mu)$ is a universal function for a μ which is readily computed from (A-3). Work function can be determined by making a fit of $\log(Y/T^2)$ to the curve of $\Phi(\mu)$, which is tabulated in many references.[28] The advantage of using equation (A-5) instead of (A-4) is that (A-5) is theoretically more accurate than (A-4) in wider range of photon energy. However, experiments showed that Fowler's theory was not necessarily a good approximation at higher values of μ. Treatment of (A-4) is still a common method to determine the work function as well as (A-5), when the surface temperature is not too high above the room temperature and the photon energy does not exceed the threshold by an amount close to the work function.

For some cases, we need to use a relatively wide band width for incident light. At the same time, the effect of temperature is not considered in eq (A-4). Validity of eq.(A-4) can be investigated by directly integrating eq.(A-2), for these non ideal conditions. When the finite band width of the incident monochromatic light is not taken into consideration, quantum efficiency below the threshold is overestimated due to higher energy component in the light. In Fig. 27, quantum efficiency for the incident light with 10 nm of band width is compared with the pure monochromatic light. Also, it shows

the deviation of eq.(A-4) from eq.(A-2), at the surface temperature of 300 K for Cs. In both cases, the errors are not large at the higher photon energies. A more important problem about using eq.(A-4) is that it will give a systematic error at higher photon energies, but for the work function determination with $(h\nu-\phi_w)<0.5$ eV, overestimation of the work function is less than 0.02 eV.

In case of an alkali-metal covered surface, the measured quantum efficiency becomes smaller than the theoretical value at the higher photon energy, due to the change of the absorption coefficient[29]. As illustrated in Fig. 28, this limits the region to determine the work function.

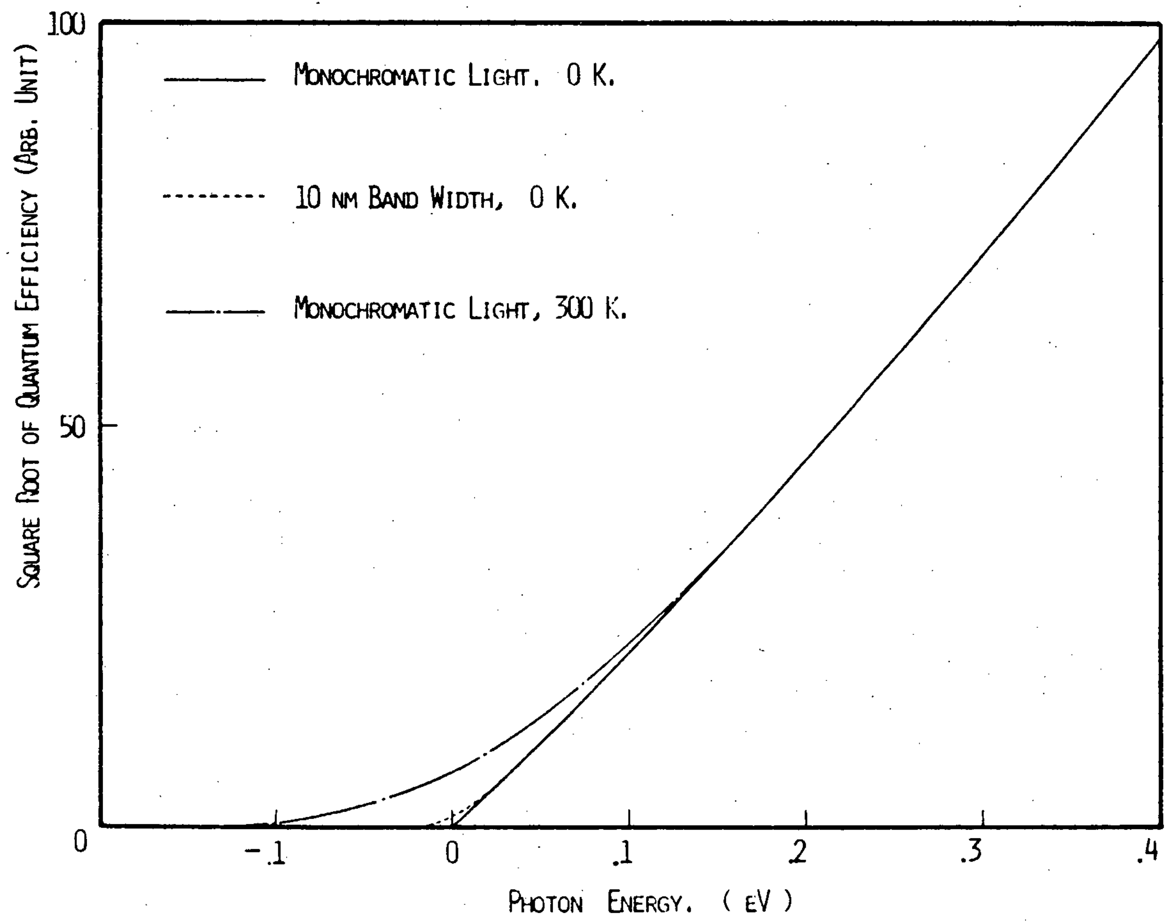

Fig. 27

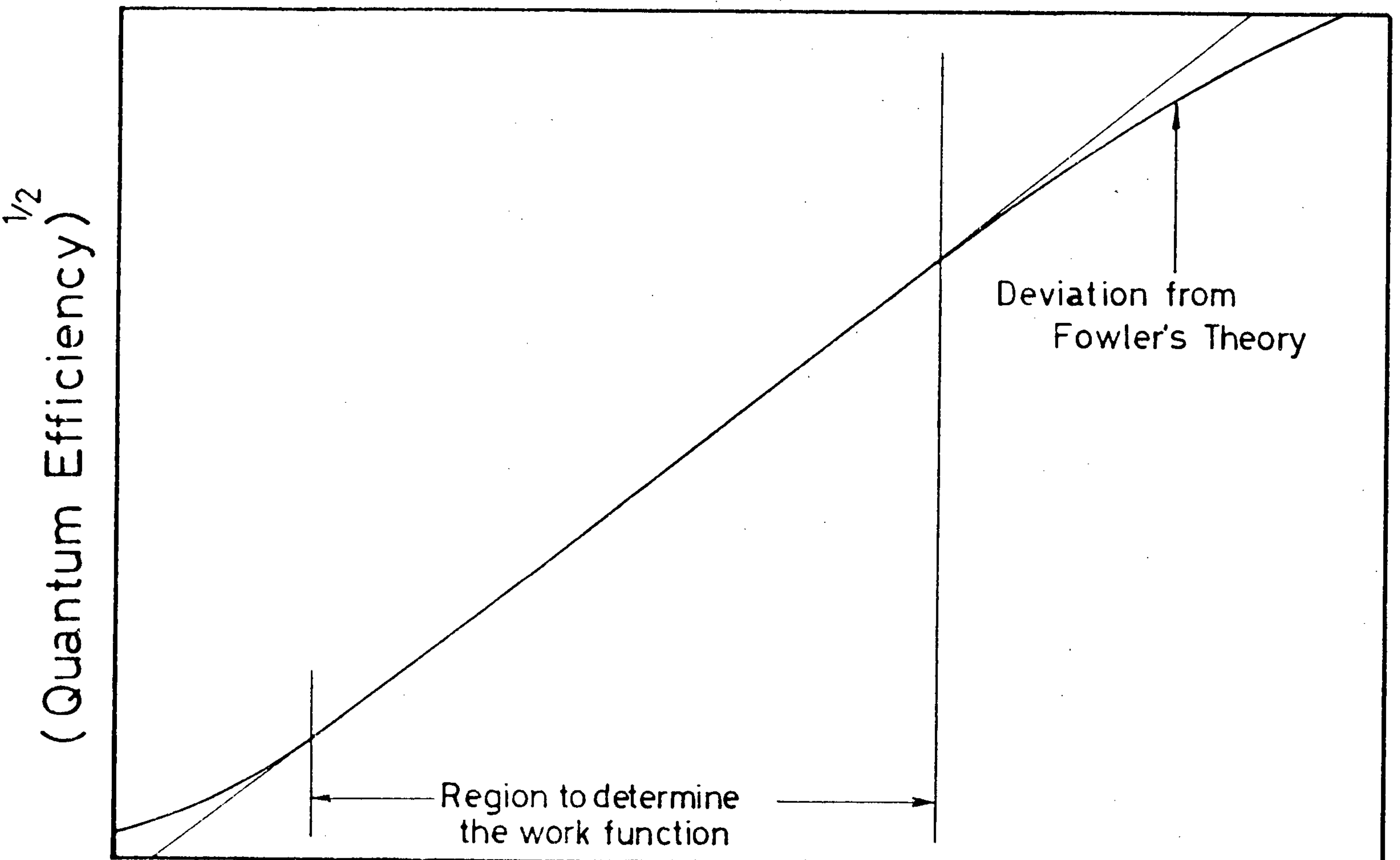

XBL 832-8231

Fig. 28

Appendix 2

Measurements of photoelectron emission from alkali-metal covered surfaces in a ultra high vacuum.

Determination of the work function by photoelectron emission measurement is a well established technique. Before applying the technique to the complex system of the surface in a plasma, several basic characteristics of photoelectron emission from alkali-metal covered surfaces were investigated to confirm the basic physics of photoelectron emission. To ensure enough time to measure the work function before the residual gases are adsorbed on a surface, an oil free ultra high vacuum system was used for the experiment. As shown schematically in Fig. 29, the sample, S.A.E.S. alkali-metal getter dispensers, the work function diode and the photoelectron collector electrode were installed in a vacuum chamber pumped by a cryo pump and an ion pump. After the proper surface treatment and outgassing of the alkali-metal dispensers, the chamber was pumped down to the 10^{-11} Torr range. Thickness of the alkali-metal on the substrate was changed by the evaporation of alkali-metal from the getters. The energy range of the incident photon was from 1.5 eV to 3.4 eV.

First, a thick Na layer on a Cu surface was prepared and the band width of the incident monochromatic light was changed by adjusting the slit width of the grating monochromator. The result shown in Fig. 30 shows that the photoelectron emission characteristic is not drastically affected by the change of the band width of

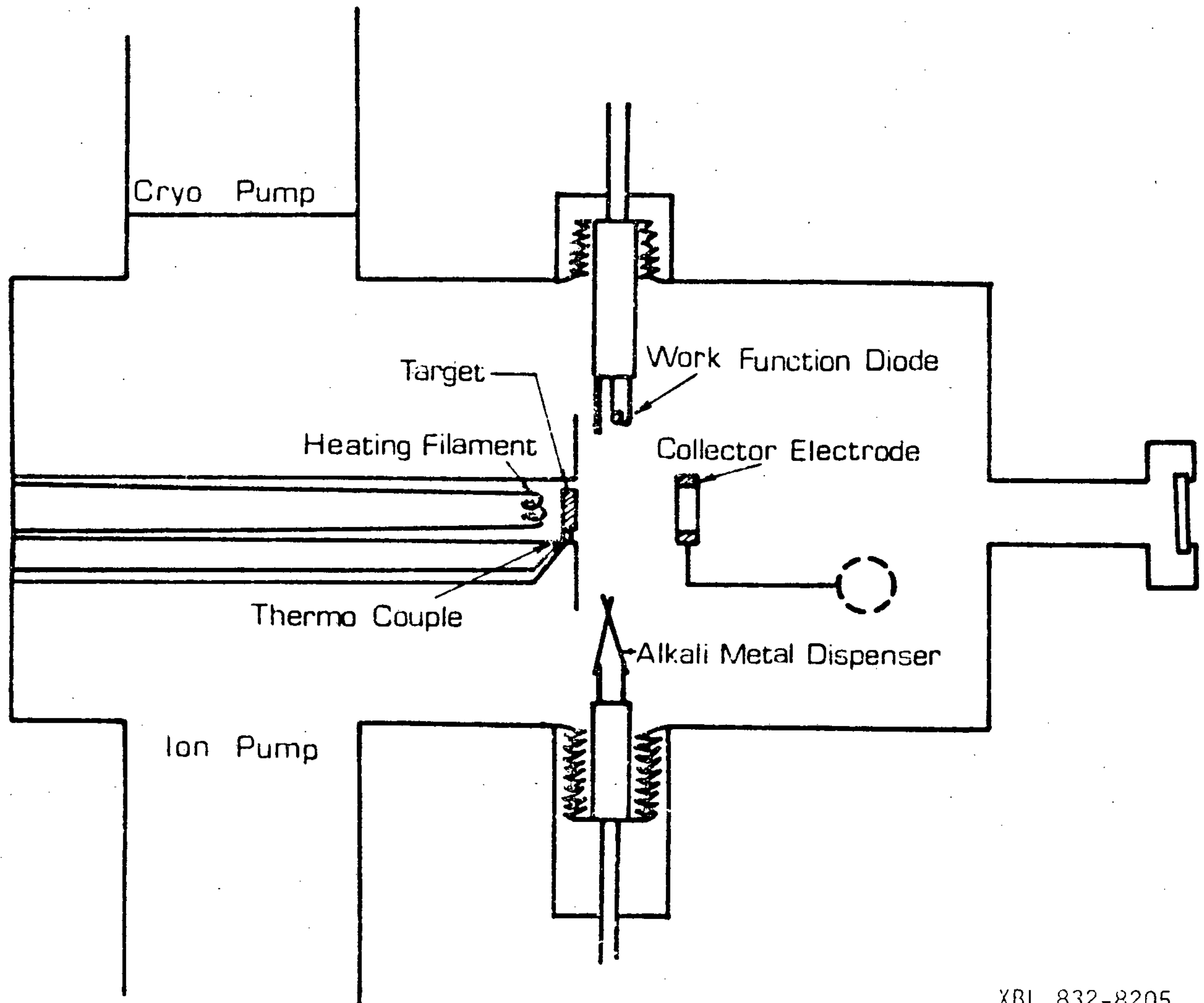

Fig. 29

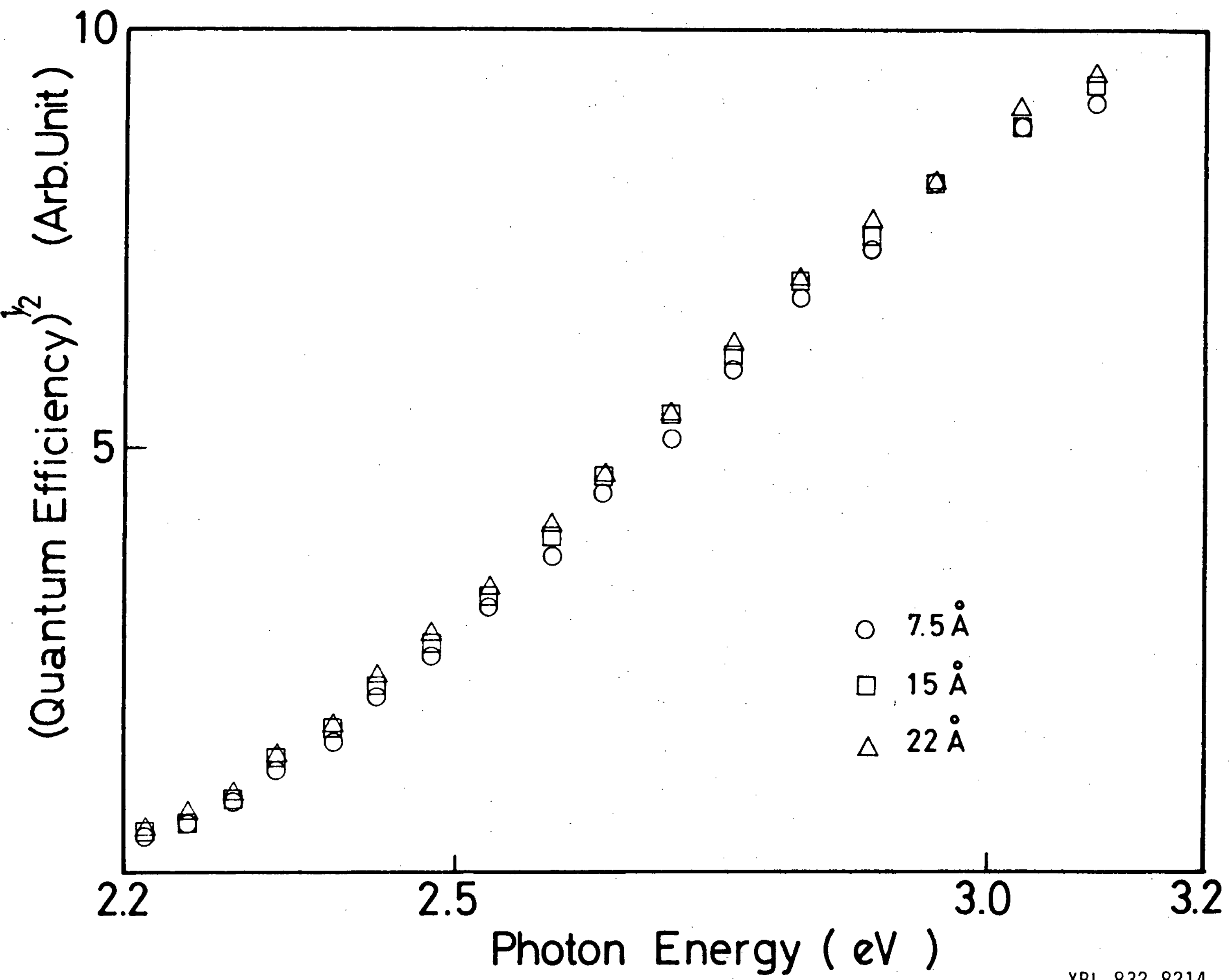

Fig. 30

the incident photon beam. Because of the limitations of the grating monochromator used, 2.2 nm was the largest band width that we could use, but it was believed that further increase of the band width will not affect the photoelectron emission characteristics.

The work function diode measures the surface work function by the field retardation of low energy electron beams emitted from a hot filament[30]. This method was used to monitor the work function in several experiments that measured the production of H^- from the surface. The purpose of the experiment was to see if there exists the systematic difference in work functions between the work function diode and the photoelectric measurements. The principal of the work function diode is to measure the thermionic electron current from the small emitter which is biased at V_b with respect to the sample surface. Then at the bias potential,

$$V_b = \frac{1}{e} (\phi_e - \phi_s)$$

where,

ϕ_e; work function of the electron emitter.

ϕ_s; work function of the sample,

the flow of electrons from the emitter to the sample is forbidden. Thus the work function difference between the sample and the emitter can be determined from the knee of the plot of the emitter bias voltage and the currnt that flows the target to the ground. The work function of a Mo surface with different Cs coverages was measured with the two techniques and the result is shown in Fig. 31.

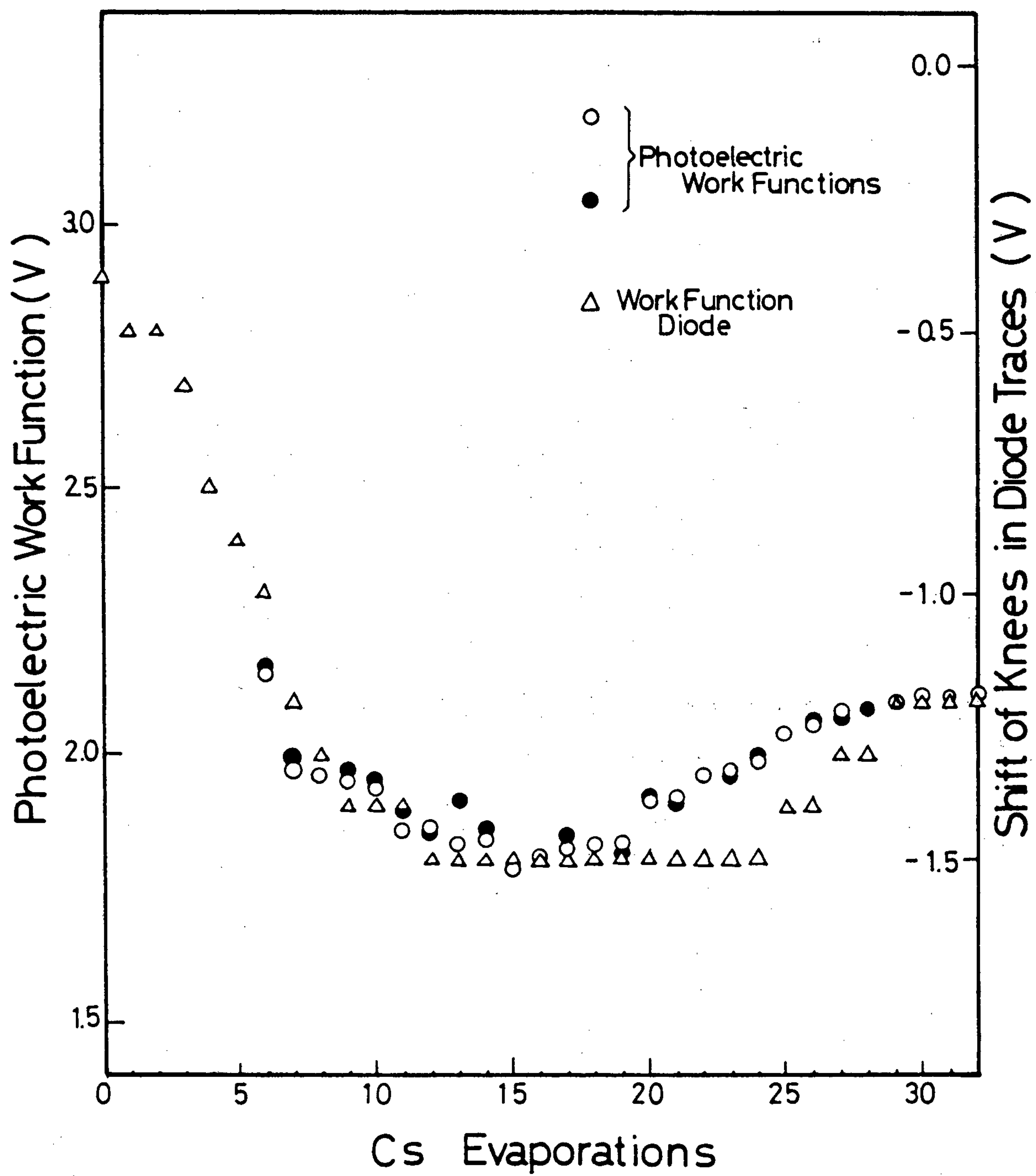

XBL 832-8229

Fig. 31

A typical trace of the filament electron emitter bias and the diode current is shown in Fig. 32. As it is seen in the trace, the electron current does not fall off sharply enough to give a good resolution. This broad energy spread stems from: 1, the potential drop across the emitter filament; 2, thermalization of electrons; 3, disturbance of the electron trajectory by the magnetic field due to filament heating current; 4, a non-uniform electric field due to surface patches[31]; and 5, geometrical misalignment of the system. Furthermore, change of the electron reflection coefficient due to the work function difference from one surface to the other is a source of substantial error[32]. It is believed that the inhomogenuity of the surface was the main source of the discrepancy in the measured values of the work functions[33]. To prevent Cs from migrating on the surface, this series of experiments had to be done while cooling the substrate with liquid nitrogen. It was reported that at this low temperature, surface inhomogenuity could be a serious problem[34]. The deviation of the photoelectric quantum yield from Fowler's theory which was often observed in the measurement suggests that this was the case. Bearing these aspects in mind, the poor agreement of the work functions measured by two different methods is not surprising.

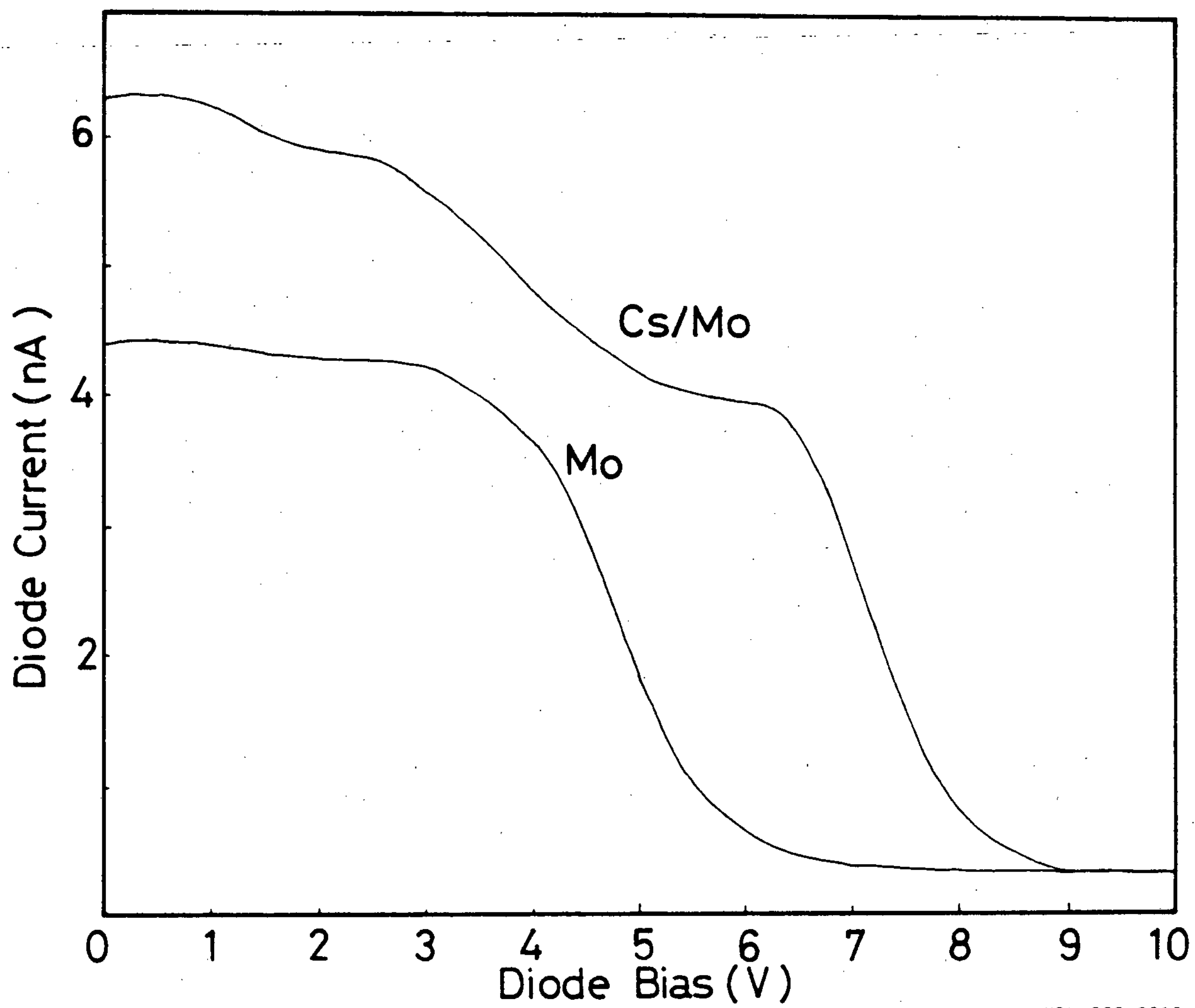

Fig. 32

Appendix 3.

Langmuir probes.

In the series of expeiments for the work function measurement of the surface in a plasma, 0.0076 cm diameter, 0.3 to 0.4 cm long tungsten wires sheilded by UO_2 glass were used as Langmuir probes. The reasons for using these probes were;

1. Smaller plasma disturbances.
2. Capability of orbital motion analysis of probe current.
3. Relatively small heating power to clean the probe.

The most important requirement in the probe measurement was not to disturb the plasma.

The Cs introduction into the discharge contaminated the surface of the probe, so the cleaning of the probe surface was necessary. The probes were biased positive until enough electron current was collected to them. By this heating treatment, Cs on the probe surface as well as other contaminants were baked out from the probe. When the Cs concentration in the discahrge was high, the amount of Cs that was adsorbed on the probe surface was not neglegible. When the surface area of the probe was large, the change of the discharge condition caused by the additional Cs baked out of the probe was recognized on the H^- current signal from the momentum analyzer. Probes with dimensions as small as written above never caused the apparant change of the discharge condition by cleaning treatment.

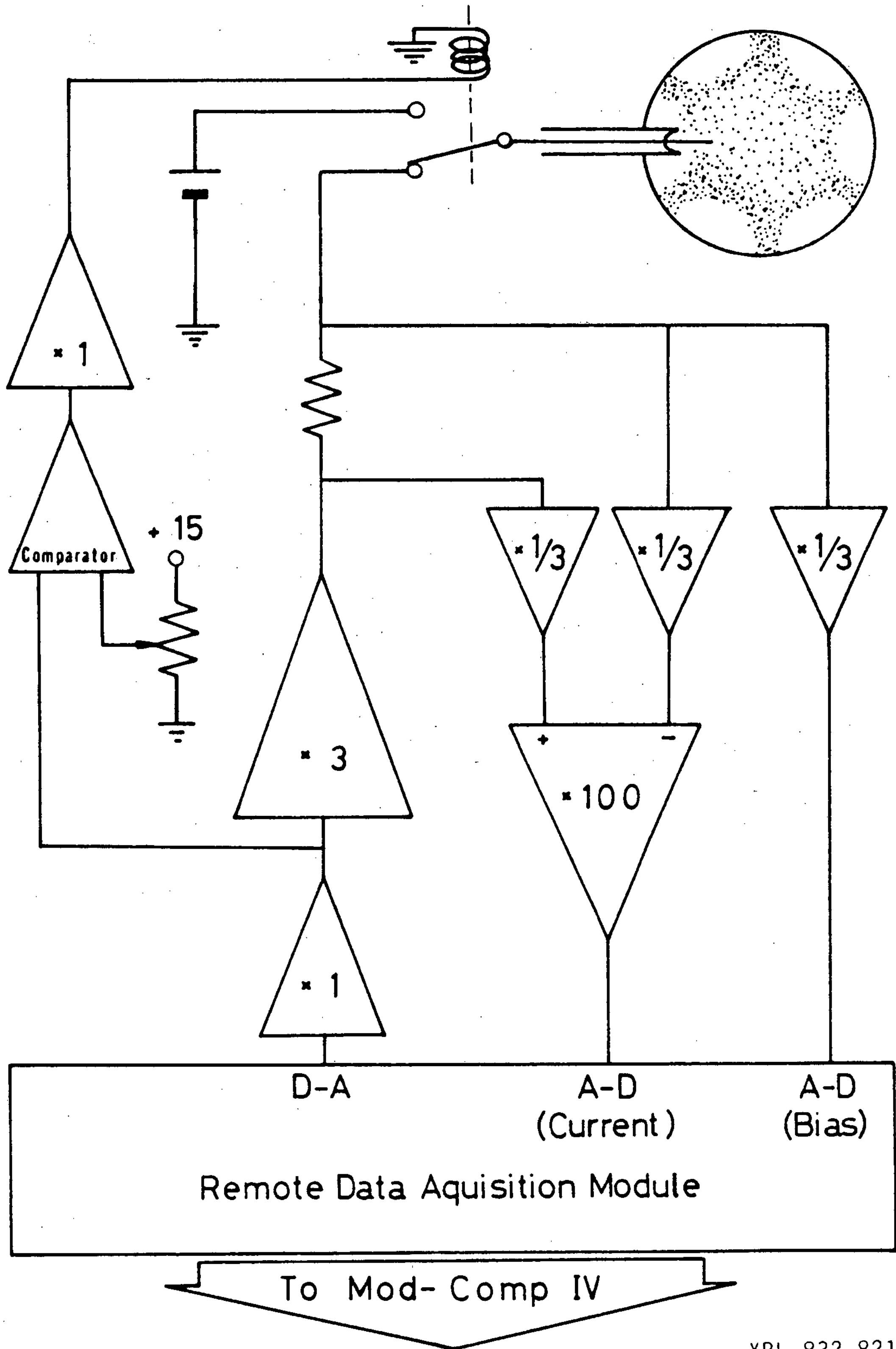

XBL 832-8211

Fig. 33

The circuit that was used for the plasma parameter measurements by a probe is shown in Fig. 33. Control of the probe bias was done by the Mod Comp IV mini-computer with a digital to analog interface connected to the power amplifier. Before a sweep of the bias, probe was heated by maintaining the bias at +26 V for several seconds. When discharge power was too small to heat the probe, an external bias circuit for probe heating was added to the circuit. After cleaning, the probe bias was swept from +26 to -26 V and the probe signals were digitalized and stored on the memory disk of the computer. The stored data were diplayed on a C.R.T screen during the experiment. A typical probe trace is shown on Fig 34. Analysis of the data was done after each series of measurements.

The plasma potential was determined as the probe bias where the second derivative with respect to the probe current for probe bias became 0. To truncate the high energy tail of the electron energy distribution, probe current was appoximated as a linear function of probe bias in the region where the probe bias was negative with respect to the plasma potential by an amount of several times the plasma temperature. Usually, this region was taken to be as -26 to -20 V of probe bias. After making a least square fitting of the stored data, the calculated linear curve was extraporated and subtracted from the probe current. When the logarithm of the remaining current was plotted against the probe bias, it showed a good fit to a linear curve near the plasma potential. An example of this plot is shown in Fig. 35. The electron temperature was determined from the slope of this plot[35].

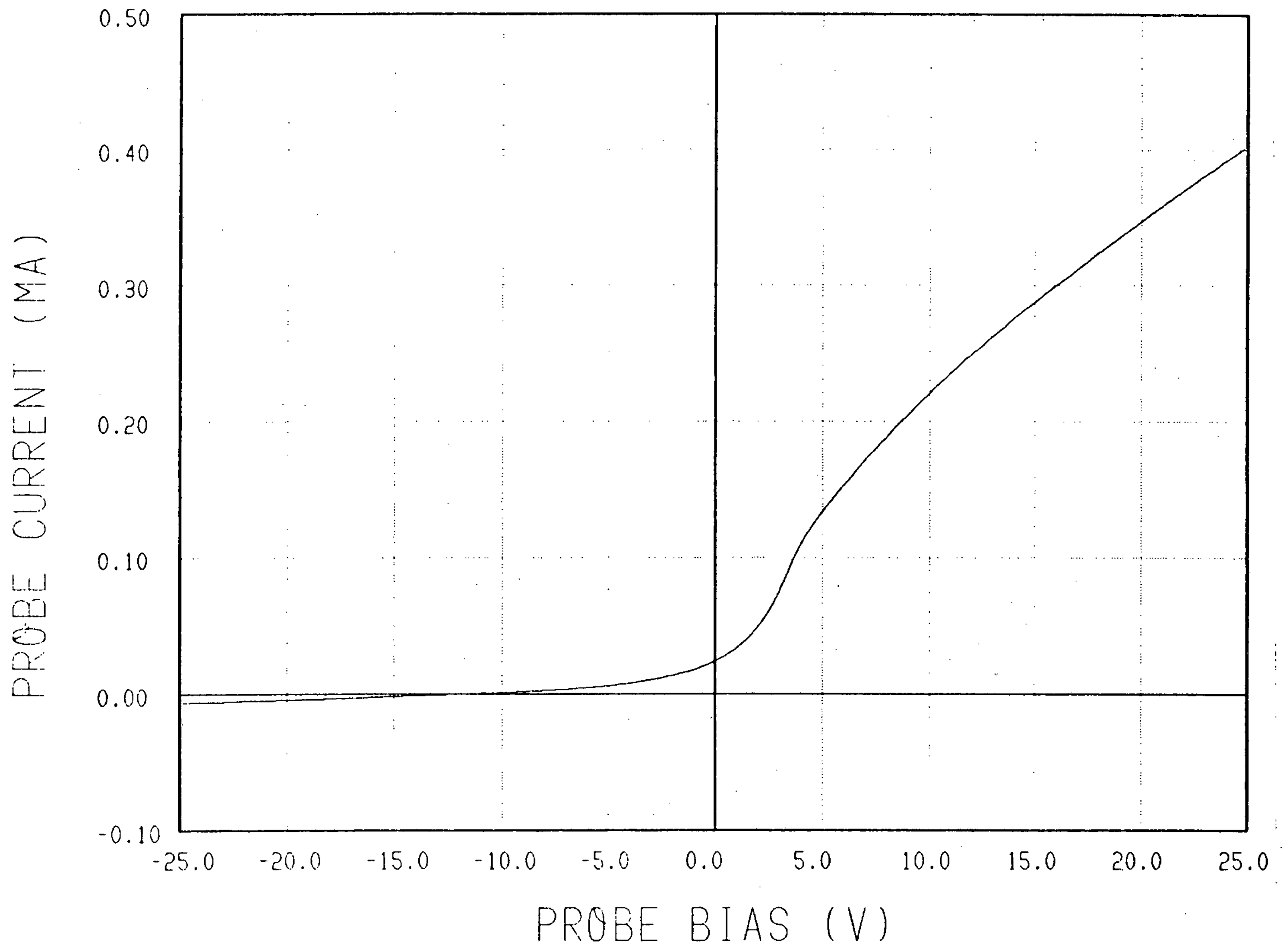

Fig. 34

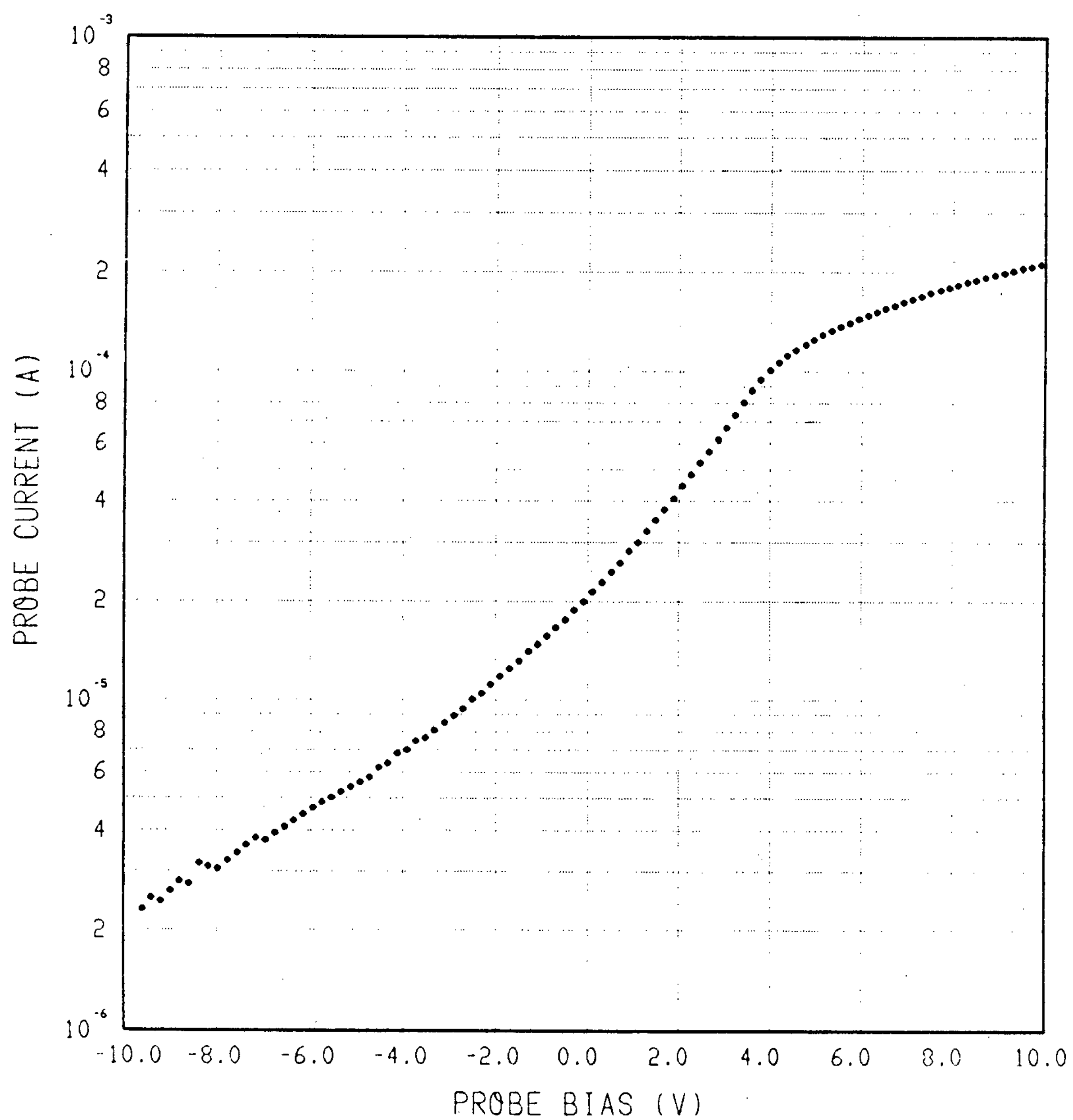

RUN 91 10/22/82 20:34:00

NE=2.2*10^9/CC TE=2.48 EV VP=3.41 V

XBL 832-8232

Fig. 35

Two ways were used to determine the electron density. One way is to use the ordinary formula of the electron saturation current, then the electron density can be written as,

$$n_e = \frac{4J_s}{eS} \sqrt{\frac{\pi M_e}{8 T_e}} \qquad \text{(A-6)}$$

where
m_e; electron mass
J_s; electron saturation current.
e ; unit charge of an electron.
T_e; electron temperature.
S ; probe surface area.

The electron saturation current was taken to be the current at the plasma potential after subtracting the current due to ions and high energy electrons. Measured electron density does not include the elctrons in the high energy tail of the distribution function.

Another way of determining the electron density is to employ the equation of the electron collection in the limit of the orbital motion around the cylindrical probe[36]. For a cylindrical probe with a radius smaller than the plasma Debye length, electron collection by the cylindrical probe can be approximately written for the probe bias $V_b > 3T_e$ as;

$$I_p = \frac{\sqrt{2}S\, n_e e}{\pi \sqrt{M_e}} (eV_b + T_e)^{1/2} \qquad \text{(A-7)}$$

When a higher temperature component is present, we may approximately write,

$$I_p = \frac{\sqrt{2}\, Se}{\pi \sqrt{M_e}} \left[n_{e1} (eV_b + T_{e1})^{1/2} + n_{e2} (eV_b + T_{e2})^{1/2} \right] \quad \text{(A-8)}$$

Hence,

$$\frac{dI_p^2}{dV_b} = \frac{2S^2e^2}{\pi^2 M_e} \left[(n_{e1}+n_{e2})^2 - n_{e1}\, n_{e2} \left(2 - \frac{2eV_b + T_{e1} + T_{e2}}{\left[e^2 V_b^{\,2} + (T_{e1} + T_{e2}) V_b + T_{e1} T_{e2}\right]^{1/2}}\right) \right] \quad \text{(A-9)}$$

Therefore, at sufficiently high bias potential, the derivative of the square of the probe current with respect to probe bias gives the approximate plasma density. A typical plot of the squared electron current and probe bias in the electron saturation region is shown on Fig.36. As is seen in the trace, the linear approximation is good.

The measured plasma potential should have included the work function difference of the probe surface, but this chenge of the work function does not affect the analysis of electron density, because no absolute value of the plasma potential is required to determine the electron saturation current. The experimental error of the plasma potential is determined by the accuracy of the measured value of the probe bias. The largest possible error was due to the digitalization of the data and it was less than 50 mV. Electron temperatures of the bulk plasma should be affected by the change of the region where we did the truncation of the higher energy electrons. When the region for which the approximate high

energy electron tail was determined was varied from -23 to -15 V with interval of 5 V, the calculated electron temperature decreased 10% at the most. So the absolute error of the electron temperature of the bulk plasma can be estimated as approximately 10%.

The electron density was usually taken to be the value determined by the orbital theory, because the electron density determination by the formula of electron saturation current counts on one point of the probe trace, while the orbital motion theory calculates the density from the entire electron saturation region. However, when the probe signal was noisy due to unstable source conditions, the electron satuation current did not give a good fit to the orbital theory. In these cases, the formula determined from the electron saturation current was used to measure the relative electron density. Estimated error of the electron density measurement by the orbital theory was less than 10%, provided the composition of the plasma is not very different. No attempt was made to estimate the error of absolute value of electron density.

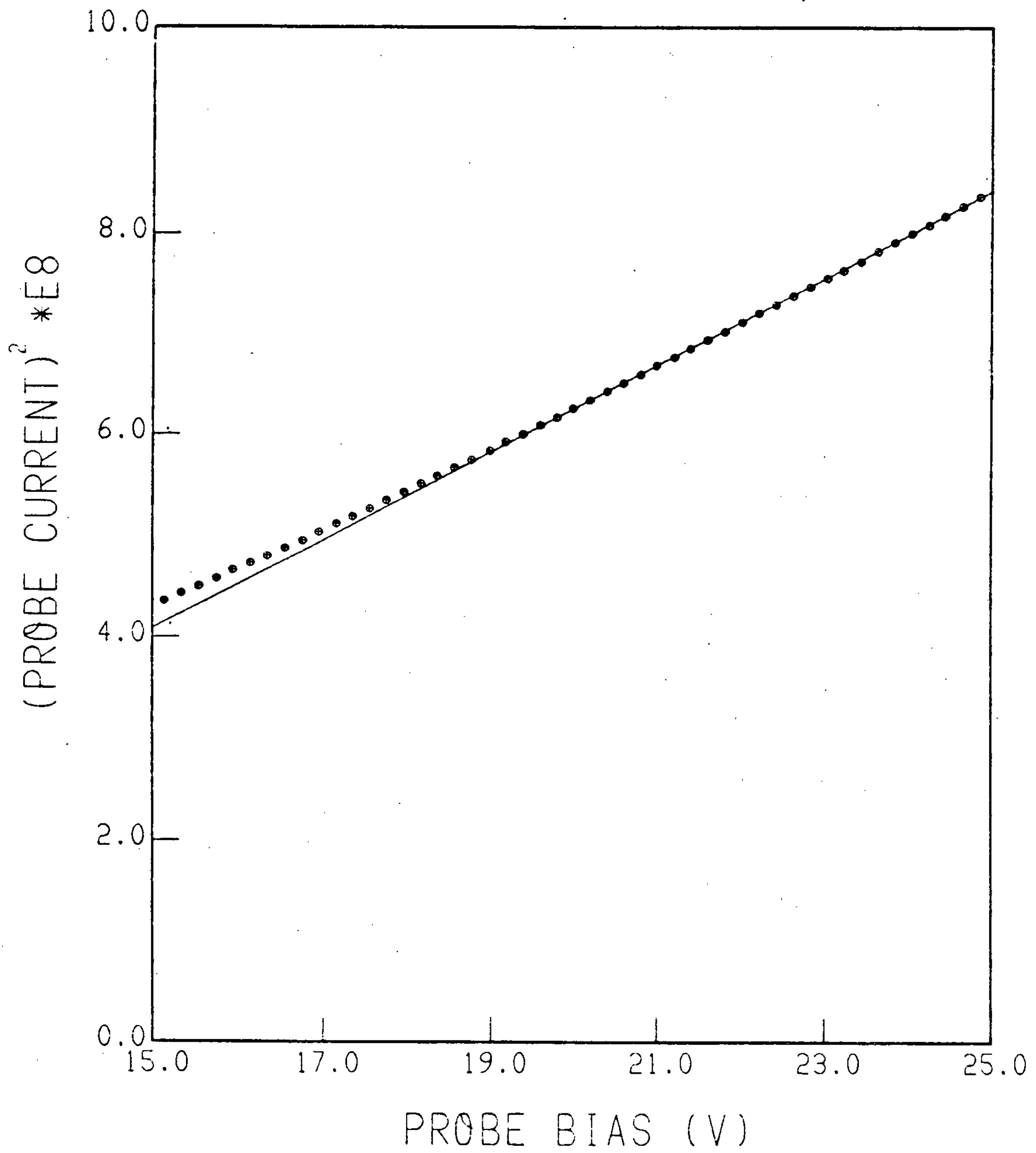

Fig. 36

Appendix 4.

The momentum analyzer.

A magnetic momentum analyzer can be used as an energy analyzer as well as a mass analyzer. To measure the differential momentum spectrum, pair of slits is adjusted to give the desired resolution determined by relation of magnetic lenses[37]. At the given momentum, a particle can pass through these two slits for a specific magnetic field. The resolution of the analyzer is defined for a mono-energetic beam as the difference between the two values of magnetic field at which the output current of the analyzer becomes half of the peak output current, devided by the magnetic field which corresponds to the peak current out of the analyzer. In the case that a monoenergetic beam illuminates the entrance slit homogeneously, and the exit slit has the width of the beam image, the trace of the output current versus analyzer magnetic field shows the triangular spectrum. For actual cases, the resolution is not strictly triangular, but usually has the spectrum form close to the triangle. Using the sensitivity, total current of the beam with energy spread can be calculated as,

$$i_{(v)} = \int_0^\infty j_{(v)} \, \eta_{(v)} \, dV \qquad \text{(A-10)}$$

where, $i_{(v)}$; detected amount of current at velocity v

$j_{(v)}$; velocity distribution of current at the entrance slit

$\eta_{(v)}$; sensitivity of the analyzer at velocity v.

Up to the second order, (i.e., accuracy to the r^3,)

$$I = \int_0^{\infty} j_{(v)} dV = \int_0^{\infty} \frac{i_{(v)}}{rV} \, dV \qquad \text{(A-11)}$$

This equation is valid even for cases of the anlyzer resolution, spectrum with non-triangular shape, provided r<<1. The energy spectrum can be computed from the simple relation,

$$j_{(E)} \, dE = j_{(v)} mv \, dv$$

$$j_{(E)} \propto \frac{i(E)}{E} \qquad \text{(A-12)}$$

The momentum analyzer that was used for the experiment had a beam collimation system as illustrated in Fig. 37. It was made compact for two major reasons. The first one was the residual magnetic field caused by the confinment magnets which was not larger than 5 G in the analyzer, but a longer travel distance for the beam would affect the analyzer dispersion relation. By setting the Larmor radius as small as 3.2 cm, the maximum error caused by the

error magnetic field should be less than 2% for 5 G of residual field and 6.0 cm of effective travel distance when H^- beam energy is above 10 ev. The second reason was the space charge effect of the beam. Energies of the surface produced H^- beams were very low. The space charge effect is more severe at low energies and it is impossible to fulfil the space charge limitation at all energies. We have set the design parameter as 100 eV for the lowest H^- beam energy. According to Klemperer[38], the current which can be detected by the analyzer with ribbon beam geometry is;

$$i = 4\ \varepsilon_0 \sqrt{\frac{2\ Ze}{M}}\ \frac{h(y_f - y_i)}{L^2}\ E^{3/2} \qquad \text{(A-13)}$$

where ε_0 ; permitivity of the vacuum

M ; ion mass

E ; beam energy

h ; slit height

y_i ; entrance slit width

y_f ; exit slit width

L ; travel distance of the beam

For the beam collimation section, we set $h = y_f = 1.2$mm and $y_i = 0.6$mm. Then we have 5×10^{-8} A for 100 eV H^- beam. For the beam analysis section, y_f is smaller than y_i. The value of y_f was determined from the geometrical focussing by magnetic field to obtain 2 % of analyzer resolution. Application of Klemperer's

formula gives more than 5 % for the analyzer resolution which seemed too large to collect important informations.

Violation of the condition given by eq. (A-13) does not affect the transmission of the beam current in the analysis section, but it simply gives the condition when all the beam that passes the entrance slit clears the exit slit. However, an exit slit size smaller than the space charge condition gives an increase of the analyzer resolution. Because other effects like misalignment of slits, and error magnetic field will change the resolution as well as the space charge condition, resolution was experimentally determined. It was found to be possible to keep 2% resolution for an H_3^+ beam with energy above 100 eV, and current below 3×10^{-8} A. Because the mass of an H_3^+ is three times that of H^-, this corresponds to 5×10^{-8} A of H^- beam as the limit.

Unfortunately, detected H^- beam current sometimes exceeded this value. The possible problem associated with the larger current compared to the space charge limit was tested with an H_3^+ beam at energies below 100 eV. By decreasing the extraction potential, resolution increased and the recorded spectrum deviated from the triangular shape; also, the integrated current decreased as the beam energy decreased. This decrease of integration current, however, was not very serious above a beam energy of 50 eV for an H_3^+ current below 3×10^{-8} A. Because the detected total H^- current did not exceed the space charge limitation condition by more than a factor of 2, and because H^- originally has an energy spread with

energy higher than the target potential, error of the integrated H^- current is estimated to be about 5% for the worst case.

Space charge effect on the differential energy spectrum is believed to cause no effect except the increase of the analyzer resolution. However, it is possible that low energy H^- current is underestimated due to larger divergence of the beam by the potential associated with space charge.

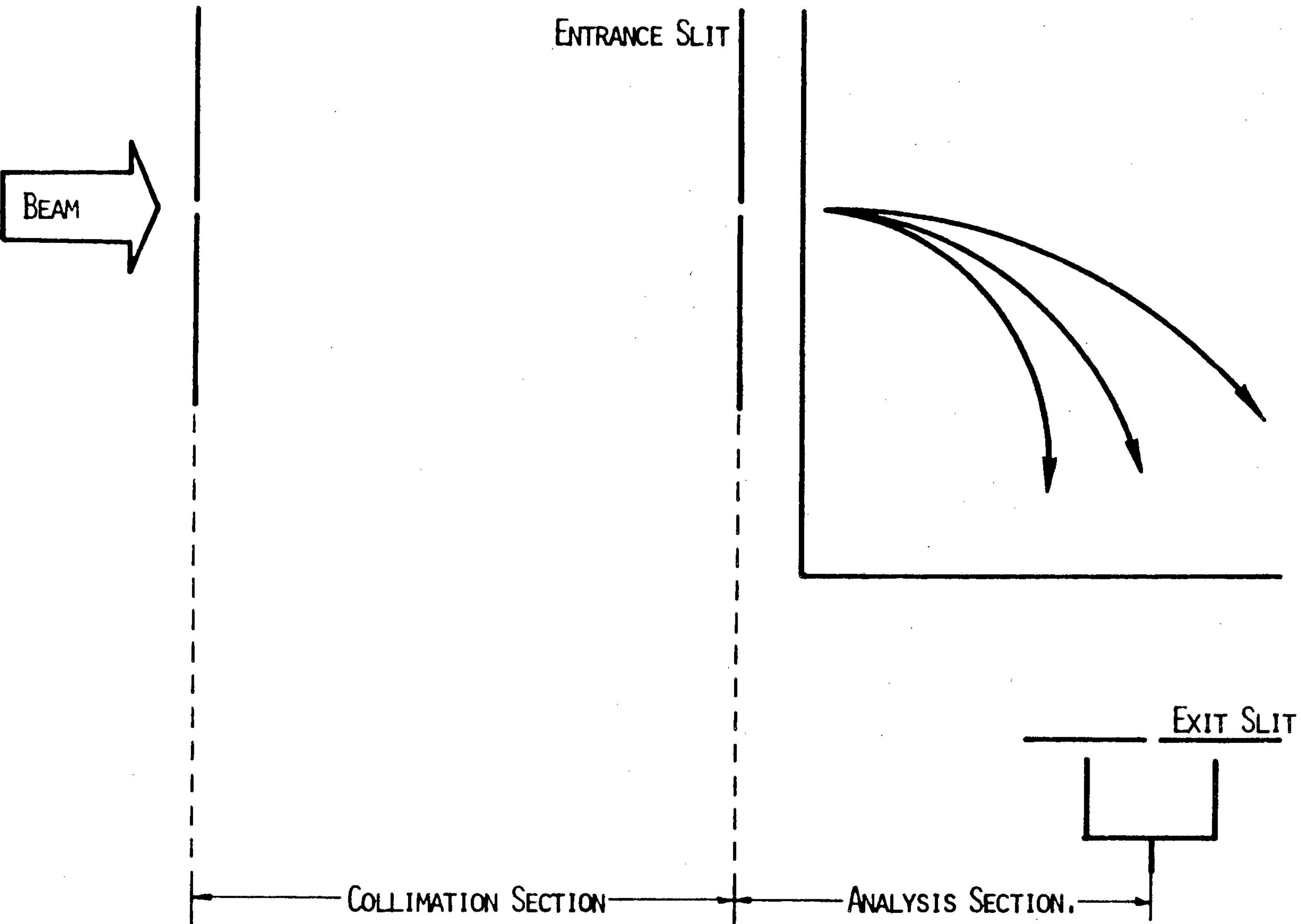

Fig. 37

Appendix 5

Pyroelectric radiometer.

The active area of the ordinary light detector is usually small. For the measurement of the total power of a light beam with an area larger than the detector size, focussing assemblies are used to condense the beam to a smaller size to clear the detector aperture. When the incident light contains a wide range of wave length, lenses are not ideal for this purpose. Also, concave mirrors are sometimes used for this reason, but they usually have the problem of short focal length and difficulty of making the off center focusing. It is for this reason that the large aperture pyroelectric radiometer was specially designed for the total incident beam power measurement of the experiment. Fig. 38 shows the basic structure of the detector. The main body of the detector was a 2.54 cm diameter gold plated disk of polarized lead zirconate titanate ceramic, coated with black gold. This coating is almost an ideal absorbant for all the photon energy range for the experiment. The performance of the detector was checked prior to the actual operation. In Fig. 39, spectral respence of the detector is shown. It is believed that the fluctuation of the responsitivity at several wave lengths is due to experimental errors, because the same value of responsitivity was recovered when the unfiltered light was projected onto the detector. Spatial dependence of the detector responsitivity was also checked and the result is shown in Fig. 40.

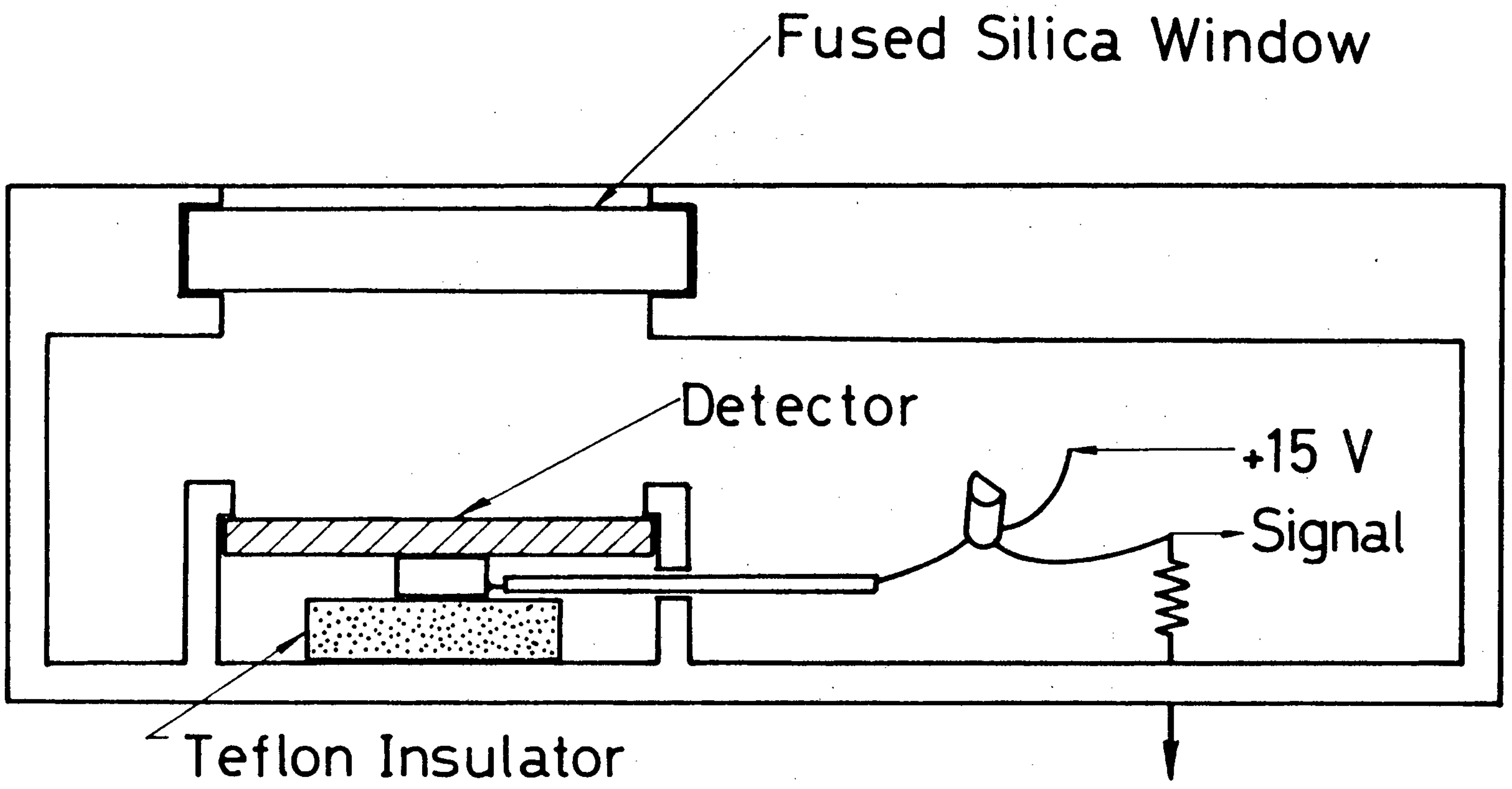

Fig. 38

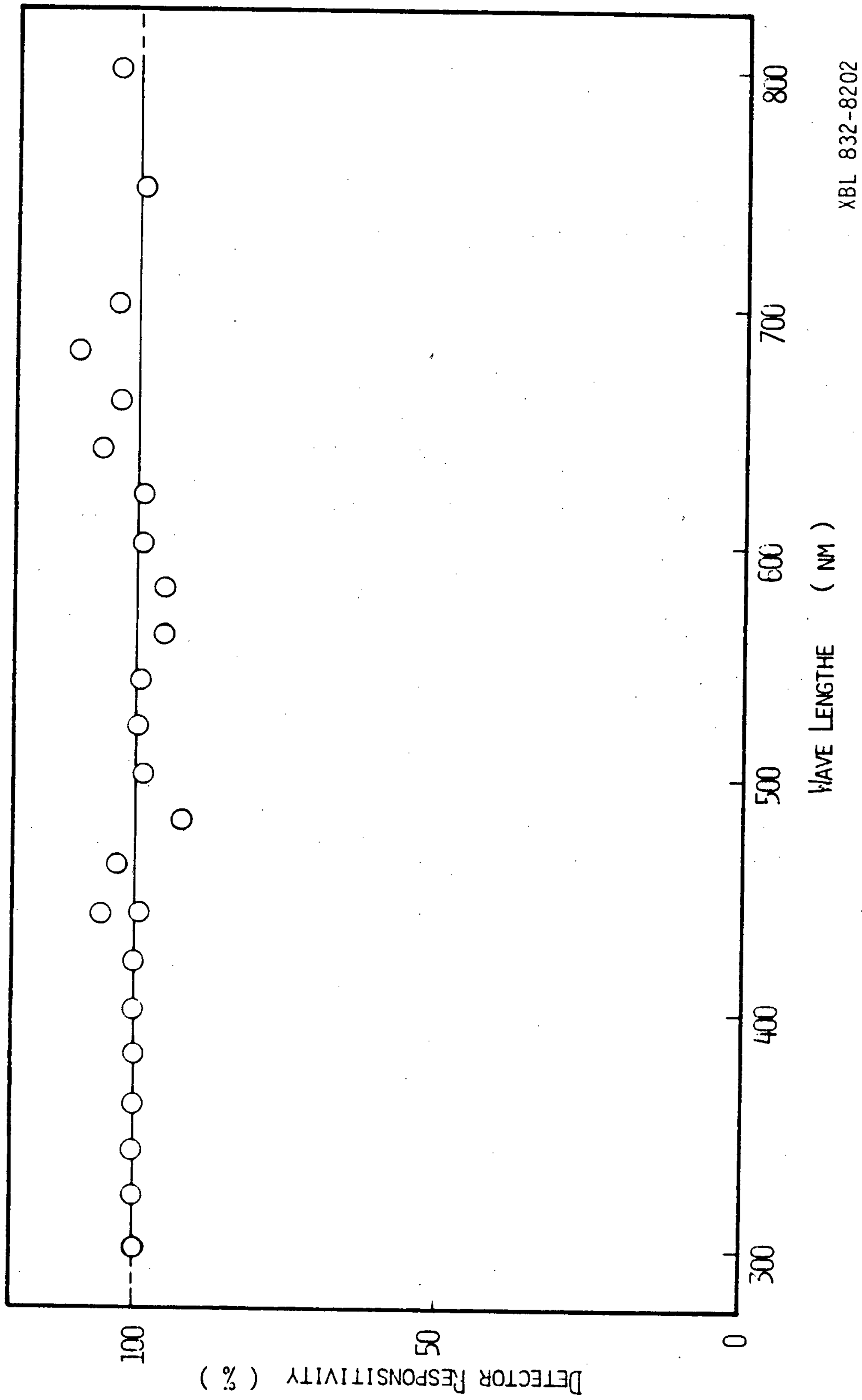

Fig. 39

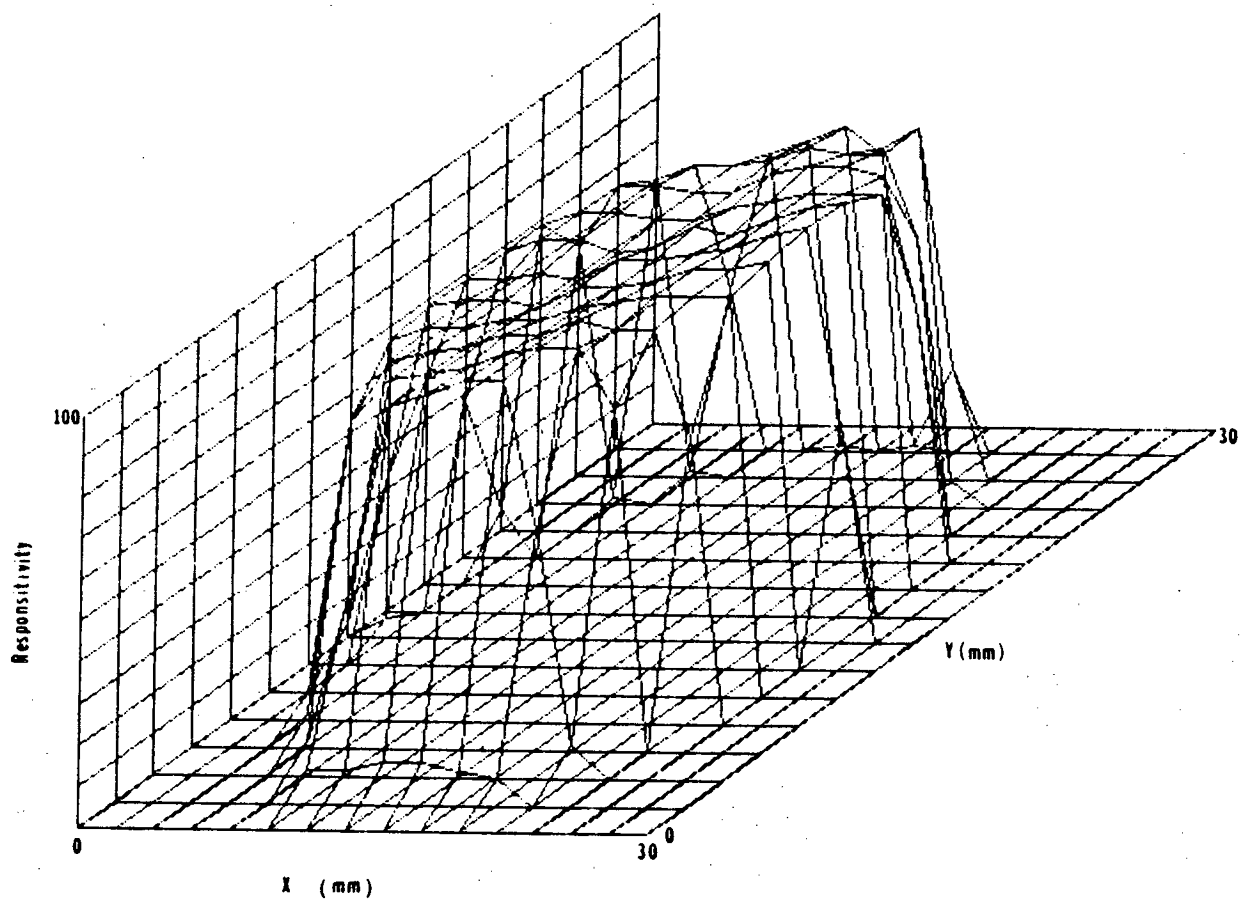

XBL 832-8277

Fig. 40

This characteristic was reproduced within 2% of accuracy for 3 times after the remodification of the collimation of the incident light to minimize the systematic error. Spatial dependence of the detector responsitivity is considered to be due to spatial dependence of the transmissivity of the sealing window rather than the absorptivity of detector coating itself.

Because of the large surface area and thickness of the crystal, the time constant of the detector was not small and the responsitivity was below 10^{-4} V/W for more than 1 kHz of chopping frequency. Since it was used for the performance check of the detector, light chopping frequency was fixed at 18.9 Hz, and the responsitivity at this frequency was 0.075 ± 0.004 V/W. Typical signal-to-noise ratio after the Lock-in amplifier was more than 100 to 1 for beam power down to 1 mW. The estimated noize equivalent power at 18.9 Hz was nearly 1 micro W.

Appendix 6

Calibration of the momentum analyzer.

The dispersion relation of the momentum analyzer was determined experimentallly. Several ions were used to calibrate the analyzer. These include H^+ and H_2^+ beams created at the target surface by electron bombardment, H^+, H_2^+, H_3^+ beams extracted from the plasma by applying a bias to the analyzer, and surface produced H^-. The measured dispersions for several different kinds of ion beams agreed well within the error of 5 % for energies above 100 eV.

The most common method which was used to calibrated the analyzer was surface produced H^- beam in the Cs plasma. Due to its low ionization potential, Cs can be ionized at the surface of the discharge filament. When the discharge filament is hot enough to emit electrons thermionically, electron ion pairs can leave the surface and create a Cs plasma[39]. For the case of our ion source, a Cs plasma with 10^7 to 10^8 cm^{-3} of electron density was observed. During this time, a very small amount of H^- was observed. This H^- was considered to be created by the sputtering of H adsorbed on the target surface by Cs^+ ions. Addition of neutral hydrogen increased this H^- current substantially, but small amount of H^- with higher energy, formed by the back scattering of hydrogen ions, was observed on the energy spectrum. One way to obtain a large amount of surface produced H^- current without the high energy tail was to load hydrogen onto the surface by a discharge[41]. A hydrogen discharge was created and the H^-

current in Cs discharge was measured soon after the arc potential and hydrogen gas were turned off. Detected H^- current decayed with a time constant of the order of seconds. It was assumed that part of the reason of this decay was due to hydrogen desorption from the surface[42]. But because Cs will be deposited onto the target, the work function should increase after the turn off of the hydrogen discharge, which was actually confirmed by the photoelectron current measurement. Therefore, it requires a more careful measurement to explain the contribution of the decrease of hydrogen adsoption to the observed decay of the H^- current.

A typical energy spectrum of the H^- current created by the Cs plasma appears on Fig.41. The peak of this spectrum was assumed to be close to the target potential. This is based on the assumption that momentum transfer from Cs^+ to H^- is not more than several eV. The Hall probe reading recorded at the peak of the beam was stored on the memory disk of the computer, and the offset of the Hall probe signal and analyzer dispersion was determined by a least squares fit program. Because a lot of Cs should be put into the chamber to run a Cs discharge, this calibration was usually done after the entire series of measurements.

One important parameter in regard to the calibration is the absolute accuaracy of the energy. To investigate this point, a field retardation type electrostatic energy analyzer with a carbon coated collector was mounted at the exit of the momentum analyzer as shown in Fig. 42. The circuit which is illustrated in Fig. 43 was

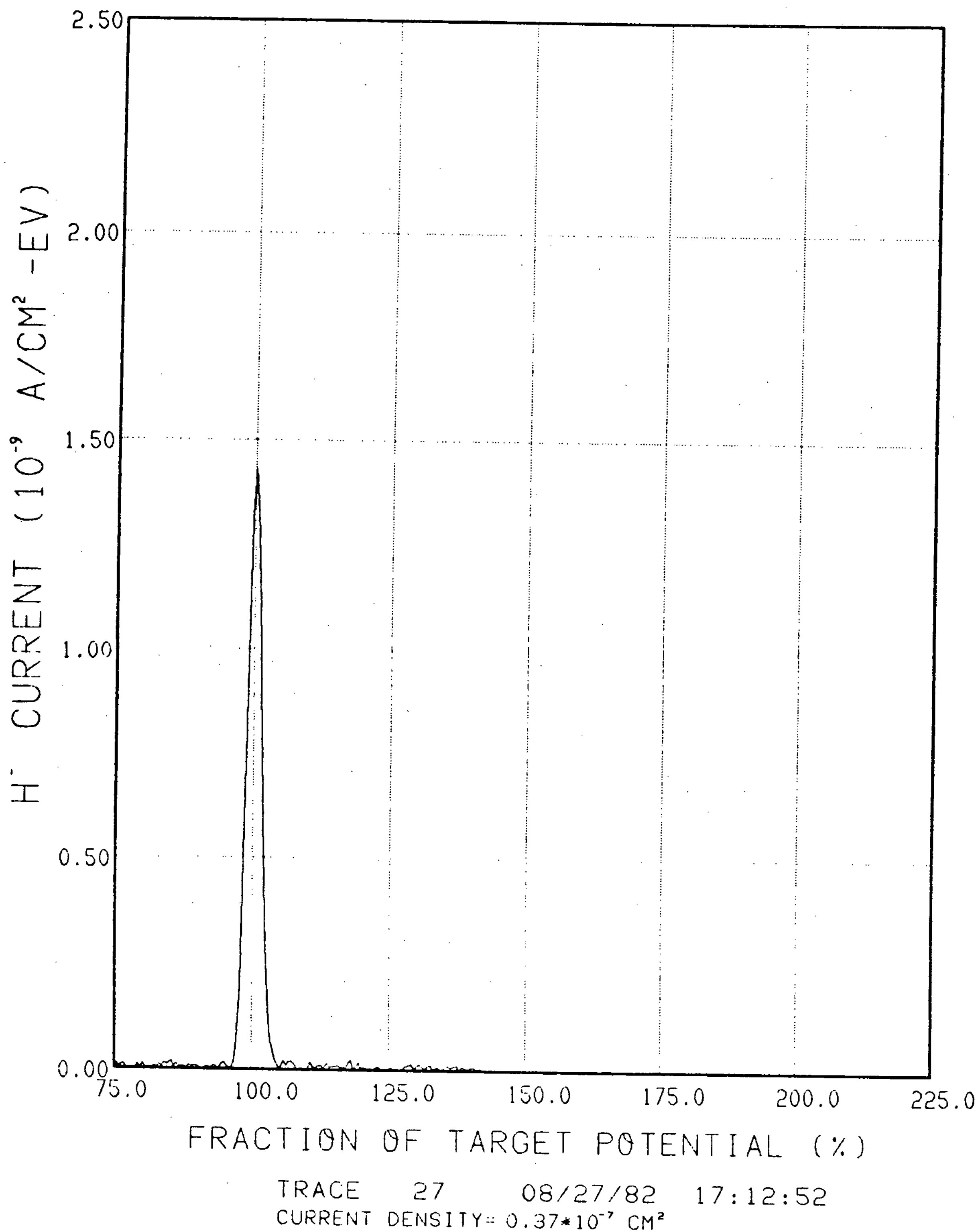

Fig. 41

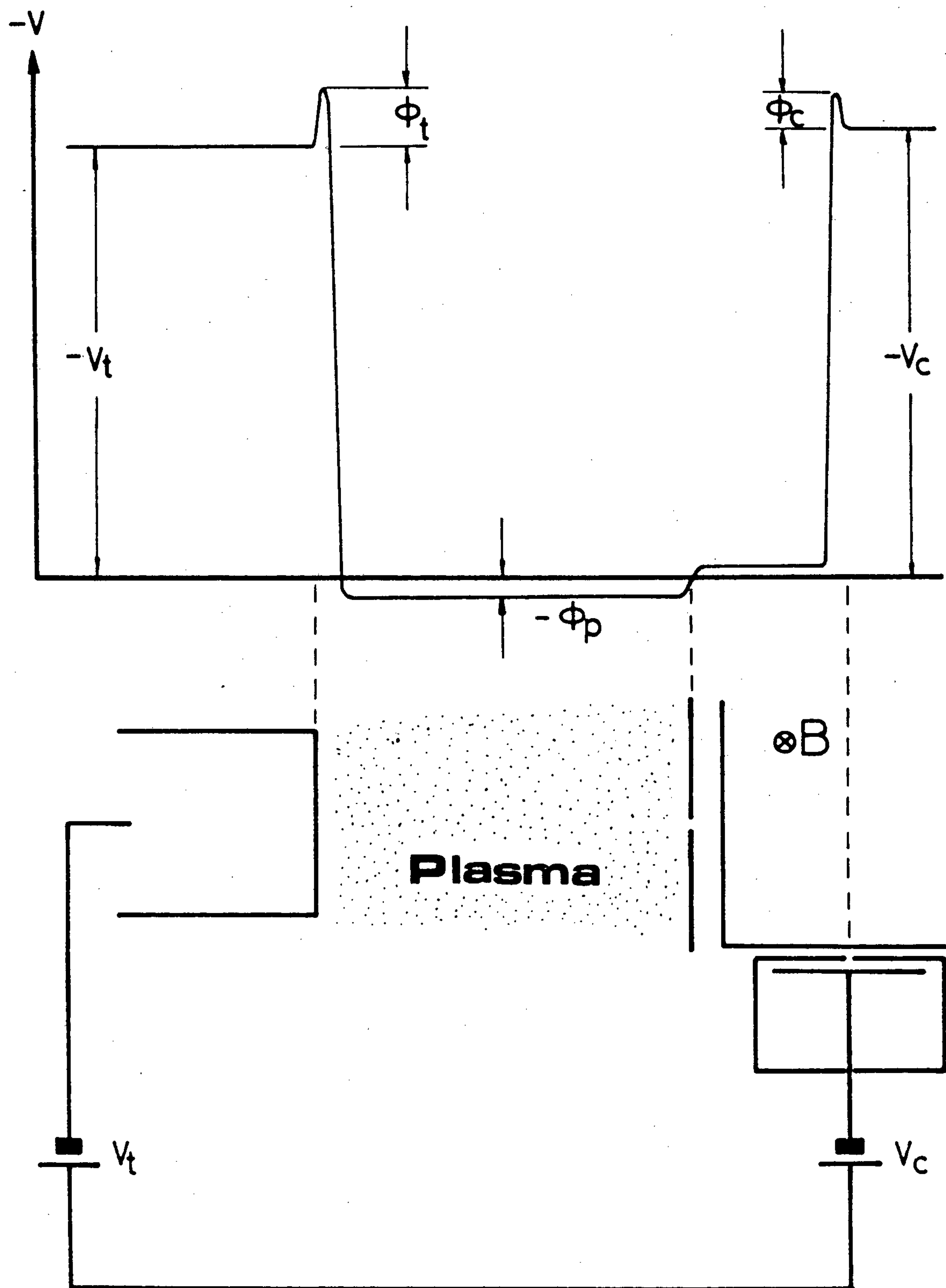

Fig. 42

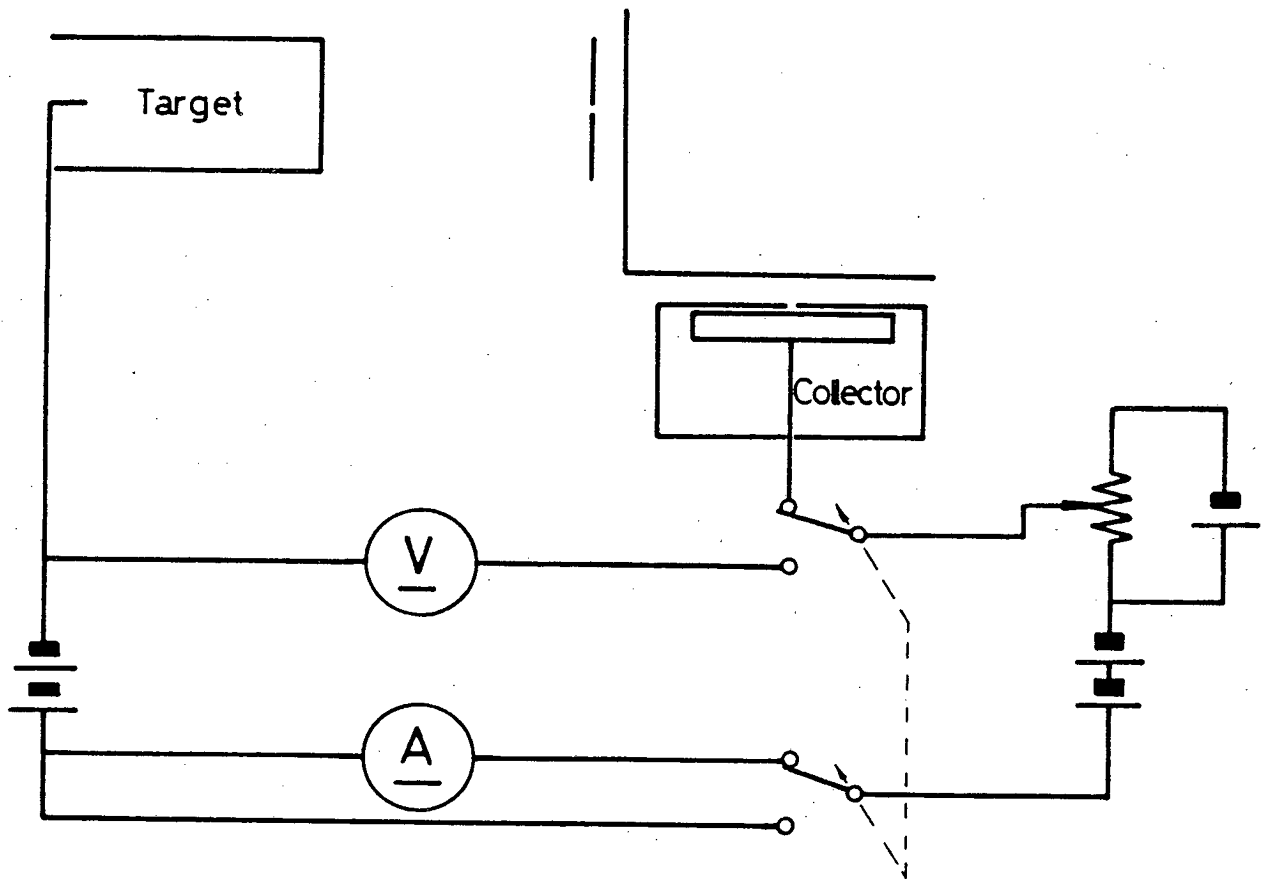

XBL 832-8194

Fig. 43

used for the measurement. At a given voltage difference between the target and the collector, the magnetic field was swept to record the spectrum of the H^- current. The measured voltage difference (V_t-V_c) at which the spectrum deviates from the one at enough acceleration voltage to the collector (V_t>>V_c, see Fig. 44,) gives the contact potential difference between the target and the collector provided that the beam contains the particles with energy equal to the target. (See Fig.42 for the potential diagram of the experiment. The H^- with no energy at the target can reach the collector, when V_t-ϕ_t is larger than V_c-ϕ_c.) The possible sources of error were misalignment of the detector and the stray magnetic field at the region of the retardation field. Both of these effects under- estimate the beam energy, and the error was estimated to be less than 2% for the misalignment, and 1 eV for the stray field. These estimations of errors are based on detector misalignment of less than 1 degree and the stray magnetic field of less than 40 G.

The experiment was first tried for the H^- beam produced in a Cs discharge. But due to the small amount of collected current, the experiment was done for a cesiated hydrogen discharge. This can be done because the peak of the H^- spectrum from a Cs discharge was always observed to be near the low energy threshold of the H^- spectrum from a cesiated hydrogen discharge. One result of this experiment is shown in Fig. 44. For this specific case, the contact potential difference was nearly 3 V. Meanwhile, target work

function was measured to be approximately 1.8 eV for this case. Assuming the work function of the carbon collector to be 4.9 eV,[43] this yields 3.1 eV of contact potential difference which is very close to the experimentally measured value. To measure the systematic error, target bias was changed, but very similar results were obtained. We believe that systematic underestimation of the beam energy due to misalignment was neglegible, or not much larger than .5 V, which was the uncertainty of the experiment comming from the obscure threshold of the H^- beam. Thus, the absolute accuracy of the calculated beam energy is believed to be determined by the spectrometer resolution of 2%.

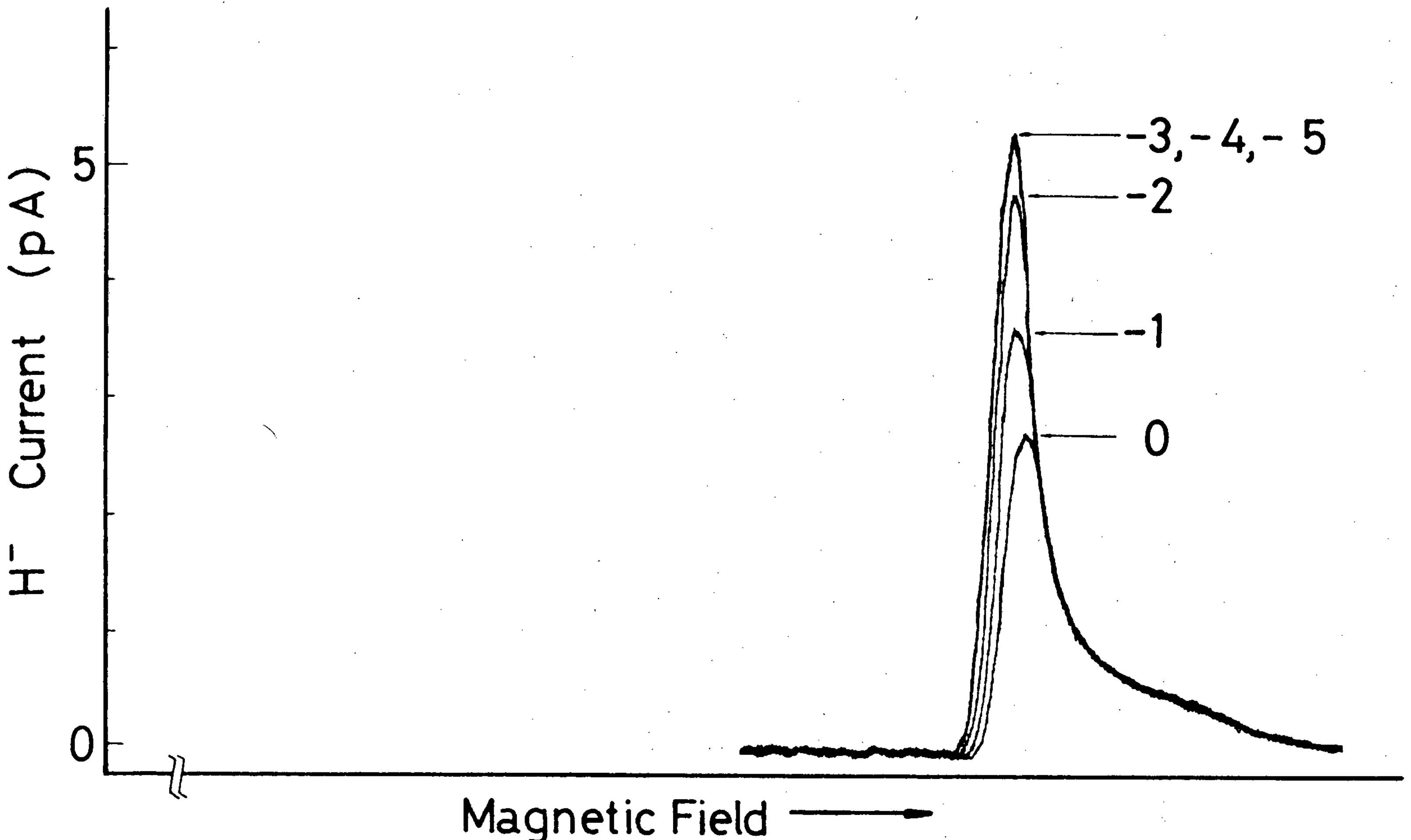

Fig. 44

Appendix 7

Change of the work function by a discharge

One of the basic questions of the surface condition of a metal immersed in a discharge is the change of the work function caused by the presence of a discharge. Positive hydrogen ions as well as atomic hydrogen may create additional hydrogen adsorption on the surface. To compare the values of work functions for two different conditions, with and without the hydrogen discharge, potassium coverage was changed on a Cu surface and the work functions were measured by photoelectron current detection.

The experiment was done in the following way. First, a thick K film was prepared on the Cu surface by K getter dispensers. Accumulation of the K film was monitored with the photoelectron current from the incidence of unfiltered light out of the Xe arc lamp. In Fig.45, the time history of the K coverage on the surface monitored by the photoelectron current is illustrated. The photoelectron current rose sharply as K was accumulated on the surface. After recording its maximum value, it then decreased as more K was deposited on the surface, until it reached a constant level. Assuming this constant level of the photoelectron current corresponded to the work function of a thick K coverage, K evaporation to the surface was terminated.

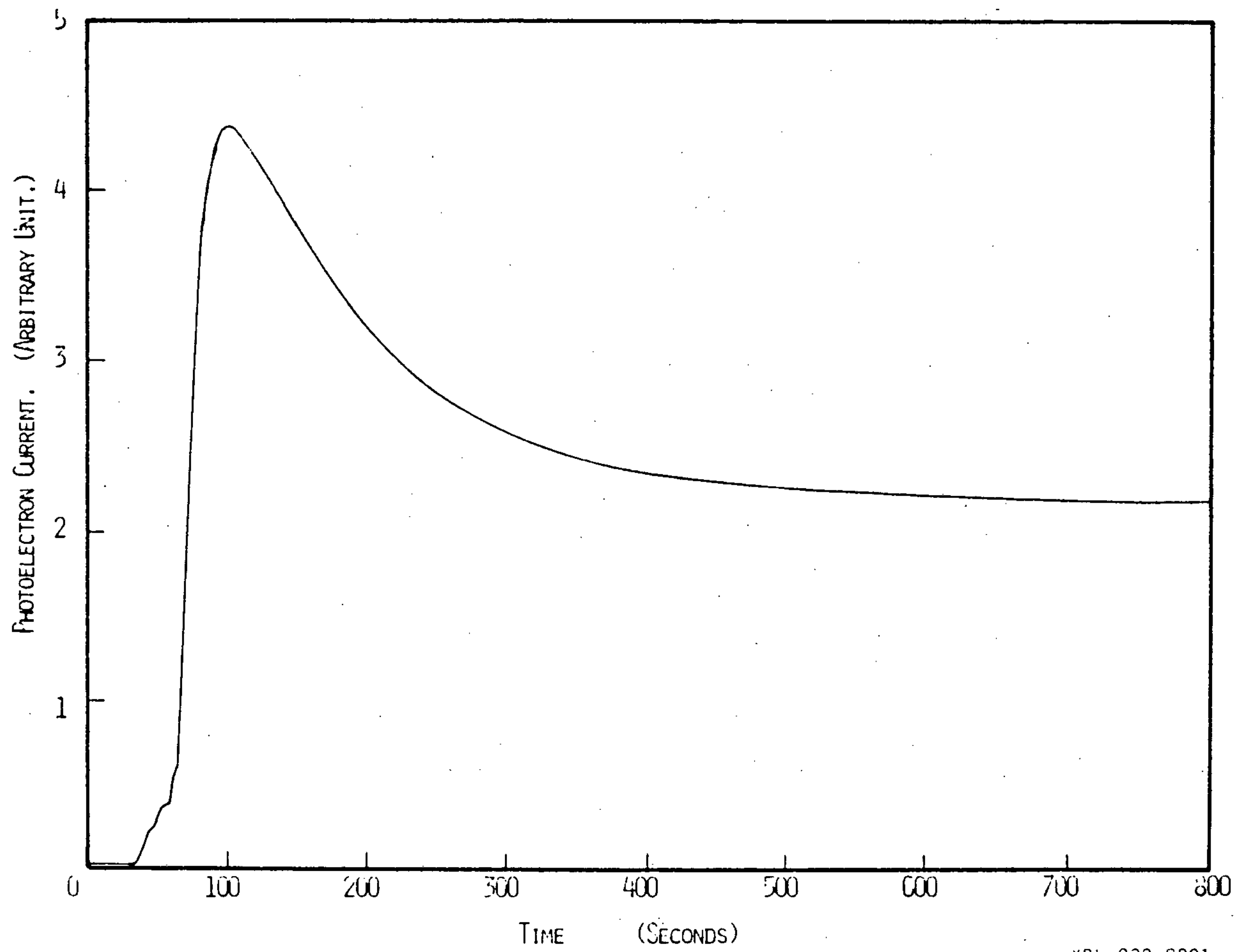

Fig. 45

The work function was measured without the plasma. Then a dilute plasma with an electron density of approximately 10^9 cm^{-3} was created. During the time the plasma was turned on, the drift of the photoelectron current was less than 5%. After the measurement of work function, target bias was elevated to 400V, and the density of the plasma was increased up to about $7x10^{10}$ cm^{-3}. With 30 to 45 seconds of this operation, a small amount of the K film was removed from the surface. The removal of the K film was recognized by the decrease of target ion saturation current. After turning off the discharge, the work function was measured for the case with no discharge and with dilute discharge. To eliminate the systematic error, the order of work function measurements was switched and the work function with no plasma was measured after that with the discharge, for several cases. The whole procedure was continued until the work function of the target became higher than the cut off of the light source.

The result (Fig.46) shows the distinct difference between the two different conditions. Measured values of work functions are higher for the case with the discharge compared with those without the discharge at both thick and thin K coverage. Near the work function minimum, the work functions with the discharge are lower than those without the discharge. If we compare with the result reported for the coadsorption of hydrogen on Cs covered W[23] and on K covered W[44], we can find the similarity among these results. It is possibe that this reduction of the work function minimum by hydrogen coadsorption is the cause of decrease of work function of Mo and Cu targets in the plasma.

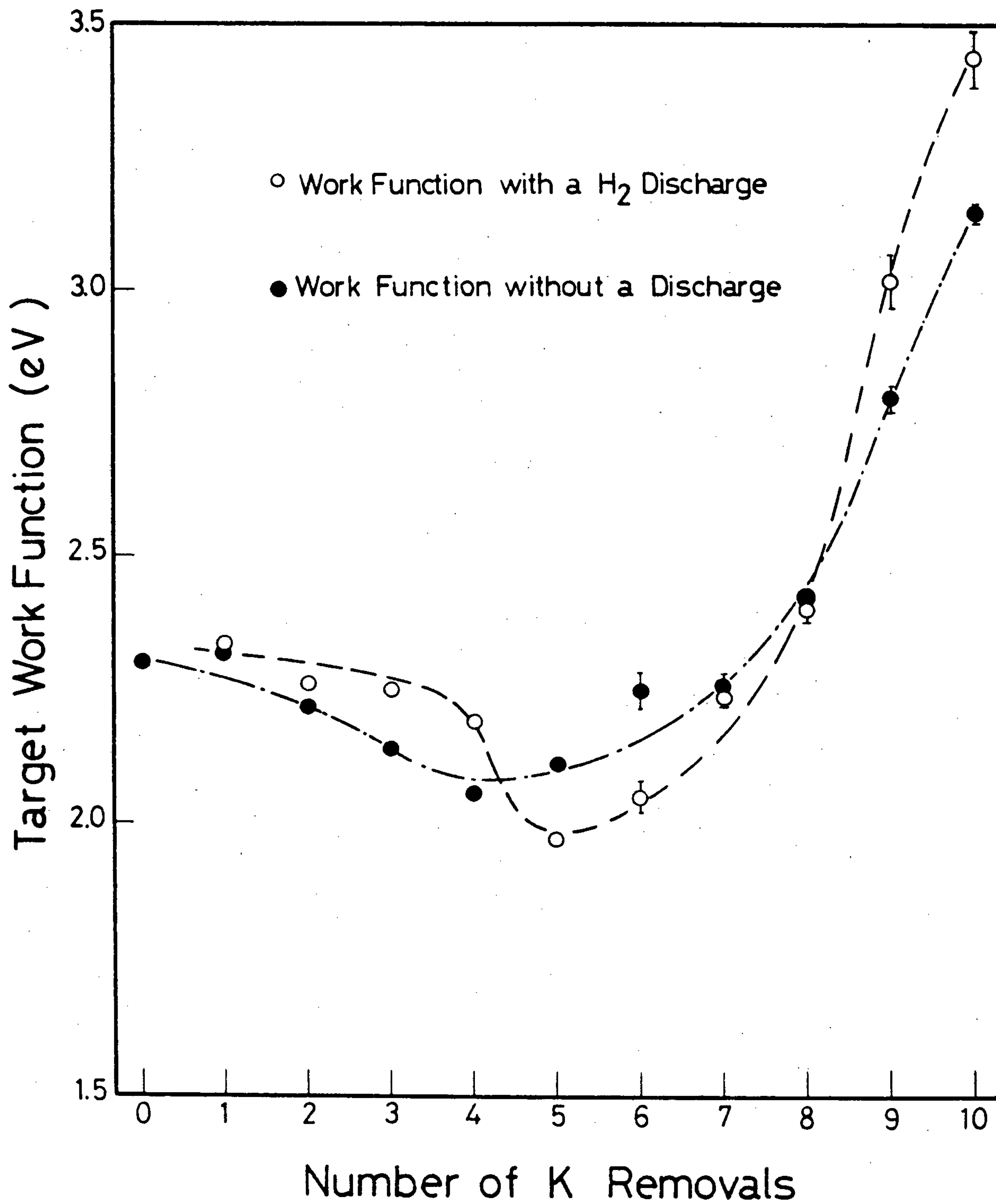

XBL 832-8228

Fig. 46

The same experiment was tried for Cs, but Cs was sputtered out of the surface too quickly when discharge was turned on. Besides, the photoelectron current drifted, possibly due to surface migration of Cs, even without the plasma. When the photoelectron current from the target were compared for a discharge and that for no discharge, we saw a similar effect as we have seen in the result of K on Cu. When the Cs coverage on the target was near the work function minimum, the photoelectron current from unfiltered light was usually increased by turning on the plasma. This suggests that the work function was decreased by the discharge. For a Cs coverage either much thinner or thicker than the work function minimum, the discharge reduced the photoelectron current from the target, which corresponds to the increase of work function by a discharge. Because the present method of work function measurement took a certain amount of time, actual comparison of work functions with and without the discharge was very difficult due to rapidly changing surface conditions. But this point should be further investigated to postulate the mechanism of reduction of work function of Cs covered metal surface in the hydrogen discharge.

Appendix 8

The plasma-sheath equation for an H^- producing surface

The sheath created between the plasma and an H^- producing surface consists of a variety of charged particles. Among them, H^- should affect the space charge condition more than secondary emitted electrons, due to its larger mass. A solution to the sheath problem by Hobbs and Wesson[45] took behavior of secondary electrons into account. The treatment given here for H^- is a modification of their approach. We define the density and the fluid velocity of H^- in the usual way as

$$n^- = \int f_{(v)} dv$$
$$v^- = \frac{\int V f_{(v)} dv}{\int f_{(v)} dv} \qquad \text{(A-14)}$$

where, $f_{(v)}$ is the velocity distribution function of H^- ions. We neglect the positive ion temperature, and assume that the velocity distribution of plasma electrons is the Maxwell distribution with temperature T_e. We also determine the total positive ion density in the same manner as n^- and v^-. If we neglect the effect of secondary electron emission, Poisson's equation reads for the space potential as,

$$\frac{d^2\phi}{dX^2} = -\frac{e}{\varepsilon_o}(n^+ - n^- - n_e) \quad \text{(A-15)}$$

where, ε_o is the permittivity of vacuum and e is the unit charge of an electron. Defining the positive ion density and the negative ion density far from the wall as n_o and n^-, respectively, the electron density at an arbitrary point can be written,

$$n_e=(n_o-n^-)\exp(e\phi/T_e) \quad \text{(A-16)}$$

The equation of continuity gives the H^- density,

$$n^- v^- = \frac{j^-}{e}$$

From conservation of energy,

$$n^- = \frac{j^-}{e}\left(\frac{M^-}{2E}\right)^{1/2}$$

where, j^-; H^- current density at infinity.

E^-; H^- beam energy at infinity

M^-; mass of H^-

Similarly, positive ion density can be written as,

$$n^+ = n_o\left(\frac{E^+}{E^+ - e\phi}\right)^{1/2}$$

where, E^+ is the positive ion energy at infinity. The equation can be simplified by defining the following quantities.

$$n_D = \sqrt{\frac{\varepsilon_o T_e}{n_o e^2}}$$

$$\omega = \frac{e\phi}{T_e}$$

$$\omega^+ = \frac{E^+}{T_e}$$

$$\omega_W = \frac{V_W}{T_e}$$

$$\omega^- = \frac{E^-}{T_e}$$

$$\gamma^- = \frac{n^-}{n_o}$$

$$\rho = \frac{x}{n_D}$$

where V_w is the bias potential of the H^- production surface. Poisson's equation (A-15) now reads,

$$\frac{d^2\omega}{d\rho^2} = - \left(\frac{\omega^+}{\omega^+ - \omega}\right)^{1/2} + (1-\gamma^-) \exp(\omega) + \gamma^- \left(\frac{\omega^-}{\omega^- - \omega}\right)^{1/2} \quad \text{(A-17)}$$

We multiply $\frac{d\omega}{d\rho}$ and integrate from ρ to ∞ . Then,

$$- 1/2 \left(\frac{d\omega}{dp}\right)^2 = 2\omega^+ - 2 /\omega^+(\omega^+-\omega)^{1/2}$$
$$+(1-\gamma) 1-\exp(\omega) + 2\gamma\omega^- - 2\gamma \omega^-(\omega^-+\omega)^{1/2} \quad \text{(A-18)}$$

For this equation to hold, the right hand side of the equation should be negative. Near the wall, ω^- ω_w , and we assume that E^+ is determined by the surrounding wall other than the H^- production surface and so $\omega^+ = 1.$[46] The severest condition for the equation is the case that all H^- are produced monoenergetically at the wall potential. To examine this situation, we put ω^- ω_w, then for $\omega_w >> \omega^+$,

$$\gamma^- \leq \frac{\left[2 \omega^+(\omega^+ + \omega_w)\right]^{1/2} - 2\omega^+ - 1}{2\omega_w - 1} \quad \text{(A-19)}$$

If we rewrite the above relation in terms of the negative ion conversion efficiency,

$$\eta^- = \frac{j^-}{eN^+V^+} = \sqrt{\frac{M^+ \omega^-}{M^- \omega^+}}$$

then,

$$\eta^- \leqq \sqrt{\frac{M^+}{M^-}\frac{\omega^-}{\omega^+}} \quad \frac{2\sqrt{\omega^+(\omega^+ + \omega_W)} - \omega^+ - 1}{2\omega_W - 1} \tag{A-20}$$

The plot of the above equation for $M^+ = M^-$ and $T_e = 1$ eV is shown in Fig. 47. It is obvious from the plot that the limitation of the produced H^- current due to this space charge effect is not very severe except at very low energy. However, for lower energies, a more accurate treatment of the equation is necessary.

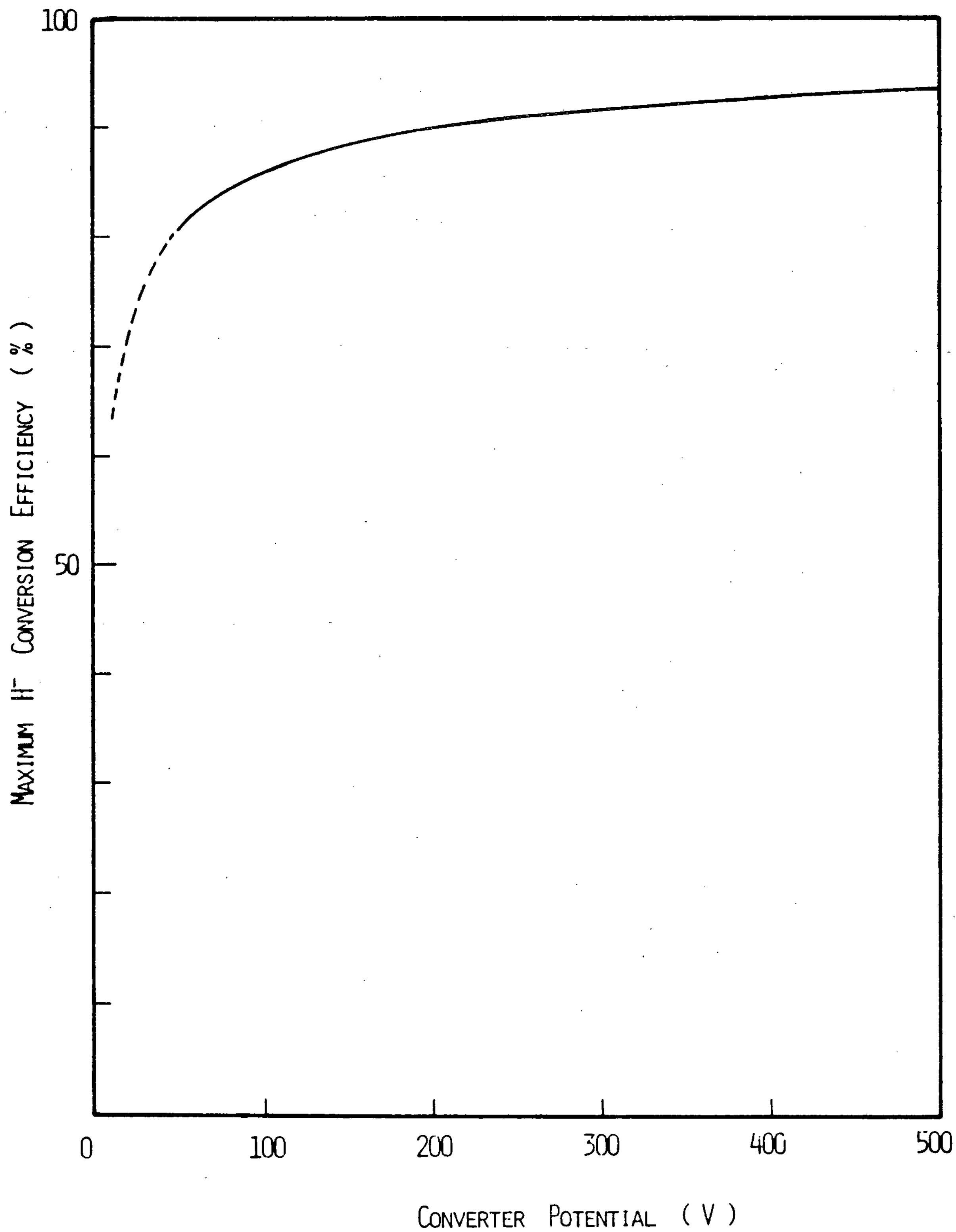

Fig. 47

Appendix 9

Work function measurement in the plasma after glow

Photoelectron current measurement using the Lock-in amplifier is inherently sensitive to the plasma noise. If the plasma noise is proportional to the plasma density, turning off of the plasma during the time of photoelectron current measurement will improve the signal to noise ratio. There is another advantage for this method. Incident light should be turned on only for the period during which the plasma is turned off. For a plasma duty cycle of close to unity, the duty cycle of light source approaches to 0. This yields diminished target heating and a smaller heat load to the optical components, particularly, the monochromator. Thus the peak power of the light can be set higher and this will result in the larger incident light power, leading to an even better signal to noise ratio.

Fig. 48, shows the time history of the measurement. The plasma is turned off for a small period of time (n_e), and the monochromatic light is quickly directed to the target (I_0). The total current of the target is the sum of the plasma current and the photoelectron current (I_t). If a gate circuit is used to exclude the plasma current during the on period (I_f), the target current can be integrated to determine the photoelectron current.

Using the Xe arc lamp, which served as the light source of the present experiment, this technique was examined for its performance. The circuit diagram is drawn in Fig. 49. The duty cycle was 3 % with a measurement period of 15 msec. Signal gating period

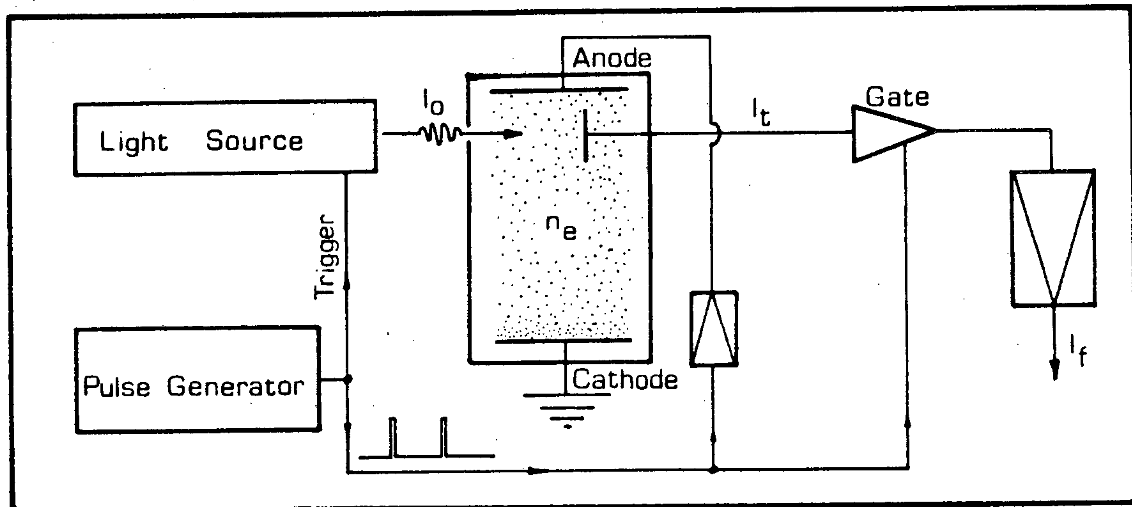

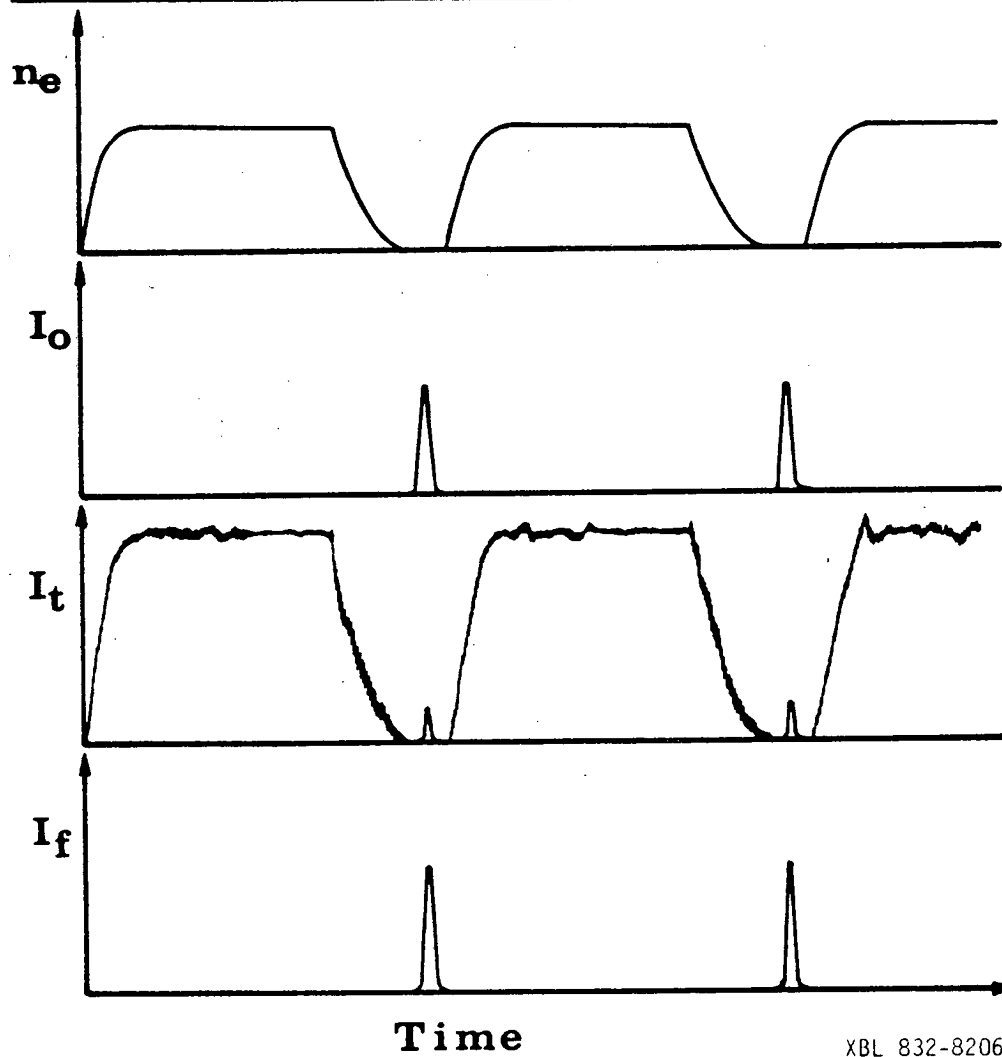

Fig. 48

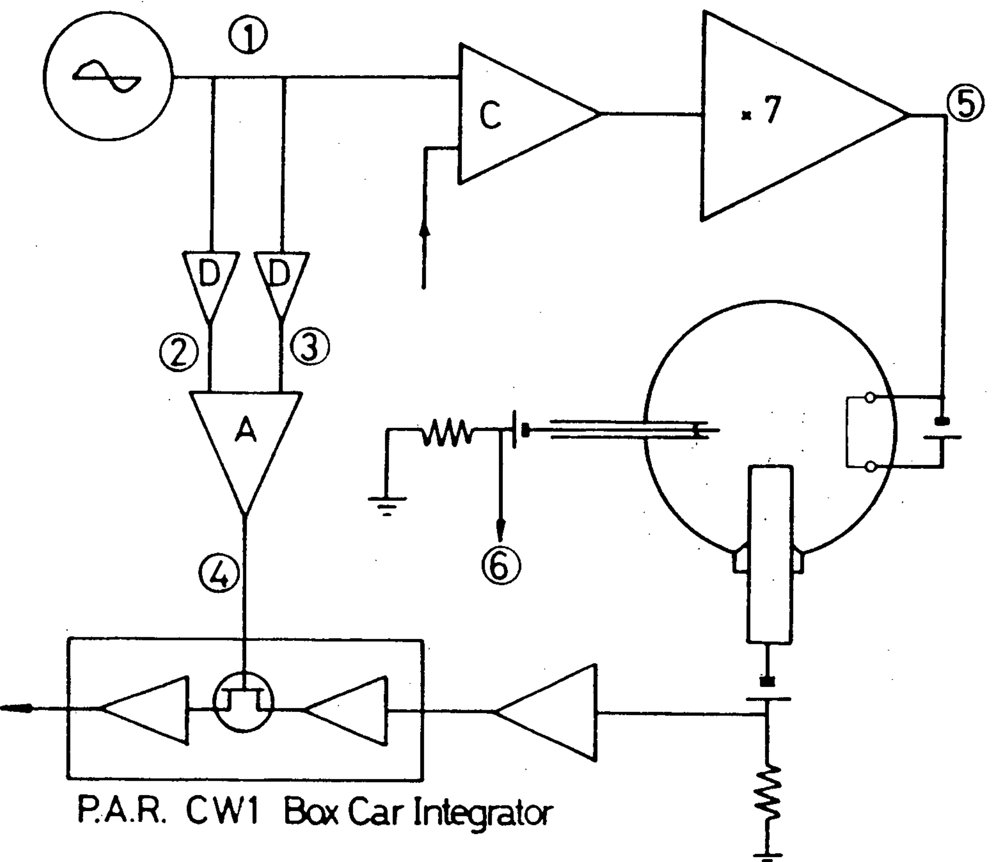

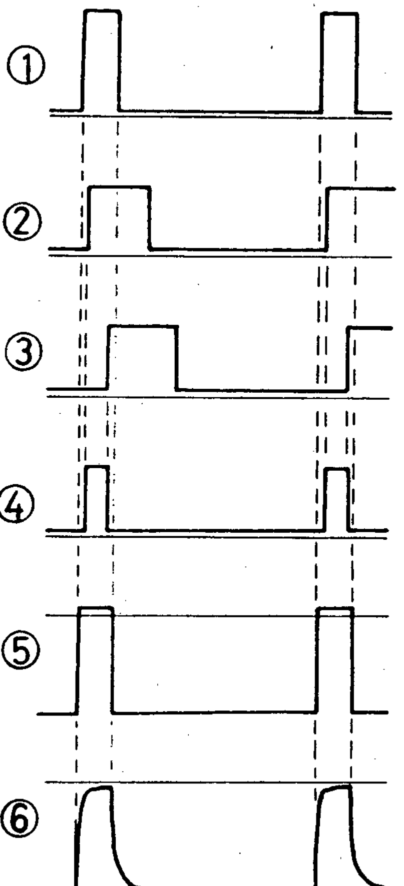

Fig. 49

was 300 micro-sec and the integration time constant was set to 300 msec. The after glow current was not neglegible and the noise associated with this current was present. It also caused a large D.C. offset to the measured photoelectron current signal. Still, signal to noise ratio was slightly better than the method of using a lock-in amplifier with the same incident light power. By using a suitable pulsive light source, this technique can be a promissing way to measure the work function of the H^- producing surface in high density plasmas.

To investigate the surface condition, we measured the H^- current from the target with a short turn off period. When total current of H^- through a high speed current amplifier was monitored, behavior of the H^- current was proportional to the ion saturation current detected at the probe. When the differential momentum spectrum of the H^- current was observed, near the threshold of the low energy side of the spectrum, a deviation in the shape of the H^- current from the ion saturation current was recognized on the osciloscope. At this point, we are not sure wheather this is caused by a change in work function of the surface of not. (One possible explanation is the beam charge up at the collimator of the mass analyzer, but the effect is not confirmed.) Before employing the method of work function measurement that accompanies plasma modulation to any kind of experiment, a thorough study of effects of discharges on surface condition should be made.

This report was done with support from the Department of Energy. Any conclusions or opinions expressed in this report represent solely those of the author(s) and not necessarily those of The Regents of the University of California, the Lawrence Berkeley Laboratory or the Department of Energy.

Reference to a company or product name does not imply approval or recommendation of the product by the University of California or the U.S. Department of Energy to the exclusion of others that may be suitable.

TECHNICAL INFORMATION DEPARTMENT
LAWRENCE BERKELEY LABORATORY
UNIVERSITY OF CALIFORNIA
BERKELEY, CALIFORNIA 94720